Fundamentals and Applications of Pressure and External Field Driven Oil-Water Microflows

A thesis submitted

in partial fulfillment of the requirements

for the degree of

Doctor of Philosophy

by

Seim Timung

Department of Chemical Engineering

Indian Institute of Technology Guwahati

April, 2018

C E R T I F I C A T E

It is certified that the work contained in this thesis entitled **"Fundamentals and Applications of Pressure and External Field Driven Oil-Water Microflows"**, by Mr. Seim Timung, has been carried out under our supervision and has not been submitted elsewhere for a degree.

Thesis supervisors

Dr. Dipankar Bandyopadhyay
Associate Professor
Department of Chemical Engineering
Indian Institute of Technology Guwahati

Dr. Tapas Kumar Mandal
Associate Professor
Department of Chemical Engineering
Indian Institute of Technology Guwahati

April, 2018

ACKNOWLEDGEMENT

Working for the accomplishment of this thesis has been the most incredible journey of my life, which would not have been possible without these people.

First and foremost, I would like to thank my thesis supervisor **Dr. Dipankar Bandyopadhyay** for giving me an opportunity to work in a very interesting area of research. I am very grateful to him for his continuous guidance, important advices and stimulating discussions. In spite of his busy schedule, he always happily spent time to analyze the problems and gave needed suggestions for the betterment of my work. Some of his remarkable qualities such as, patience and devotion towards his work, his continuous zeal to achieve perfection, and a very attractive communication skill, will always inspire me. The experience of working with him will definitely have far-reaching influence in my life. I consider it an honor to work under him.

I would like to express my deepest gratitude to **Dr. Tapas Kr. Mandal** for his insightful comments and suggestions during the course of my research work. His continuous encouragement and support gave me a lot of inspiration to carry out this research work.

It gives me immense pleasure to acknowledge the support and help of **Dr. Abhiram Hens** and **Dr. Ravi Kumar Arun**, Microsystem Technology Lab, CMERI, Durgapur, India.

I wish to thank my doctoral committee members, **Prof. S. Kanagaraj**, Department of Mechanical Engineering, **Dr. Mahuya De** and **Dr. Vimal Katiyar**, Department of Chemical Engineering, for their valuable suggestions and efforts during my thesis work.

My sincere thanks to **Dr. A. Ananth Praveen Kumar** and **Dr. Kartick Mondal,** alumni from our research group, **Dr. Nayanmani Das,** Institute Post-Doctoral Fellow, and **Mr. Mridupawan Sonowal**, National Institute of Technology, Meghalaya, for their co-operative assistance in learning the basic concepts and providing me with continuous encouragement throughout my PhD tenure. Also, I am particularly grateful to **Mr. Abhinav Sharma, Mr. Amit Kumar Singh, Mr. Joydip Chaudhuri, Mr. Manash**

Pratim Borthakur, Mr. Mitradip Bhattacharjee, and **Mr. Vijeet Tiwari,** for their supports in experiments and computations.

I am also thankful to other members of our research group, **Ms. Abhijna Das, Mr. Abir Ghosh, Mr. Ankur Pandey, Ms. Anuja Tripathi, Mr. Bhaskarjyoti Sharma, Mrs. Binita Nath, Mr. Bolleddu Ravi, Mr. Debdatta Ghosh, Mr. Debendra Nath Sarkar, Mr. Divesh Ranjan, Mr. Jayant Borana, Mr. Nilanjan Mandal, Mr. Pritam Roy, Md. Rashid Ali Faridi, Mr. Saptak Rarotra, Ms. Satarupa Dutta, Mr. Shaik Shahid, Ms. Snigdha Chakraborty, Ms. Shreya Mukherjee, Mr. Shirsendu Mitra, Mr. Siddharth Thakur, Dr. Sunny Kumar, Mr. Surjendu Maity, Mrs. Tamanna Bhuyan, Mr. Venkatanarayana Prasad S, Mr. Vineet Kumar,** and last but not the least **Mr. Viswanath Pasumarthi.** I cannot forget to thank my friends **Mr. Abhik Bhattacharjee, Mr. Ashim Malakar**, **Mr. Biki Teron, Mr. Kiran Saikia, Mr. Manash Jyoti Borah, Mr. Pradip Das, Mr. Rahul Saha, Dr. Rupak Kishore, Mr. Sanjay Dutta, Mr. Siddhanta Roy,** and **Mr. Subrat Kotoky,** for the lovely support in making my stay at IIT Guwahati very memorable.

My special thanks goes to all the faculty and staff members of **Department of Chemical Engineering**, and **Central Instruments Facility**, and **Center for Nanotechnology**, **IIT Guwahati,** for their supports and co-operations during all this time.

I also wish to convey my sincere gratitude to obtain financial support through the **MeitY grant no. 5(9)/2012-NANO** and facilities through the **DST-SERB, grant no. SR/S3/CE/0079/2010**.

Above all, I wish to thank my **parents, and family members** for their love and support throughout everything, as always.

I dedicate this thesis to *My Family.*

SEIM TIMUNG

SYNOPSIS

Fundamentals and Applications of Pressure and External Field Driven Oil-Water Microflows

1. Introduction

Interfacial morphologies of two-layer flows in microfluidic devices have been studied comprehensively in recent times because of their diverse applications in the areas of bio-analysis, multiphase unit operations, emulsification, MEMS devices, microreactors, and energy harvesting, among many others. Microfluidic devices are considered superior to their macroscopic analogues primarily because of the availability of higher surface to volume ratio in the flow morphologies, smaller throughput leading to easier control on the operating parameters, and the reduced operating cost in the processes owing to the lesser usage in the quantity of materials where costly chemicals are in use. The microscale two-phase flows are also fundamentally an exciting area of research because of the manifestation of diverse interfacial flow morphologies in the form of slug, plug, core-annular, stratified, wavy, bubbly, and drop-dispersions, among others. These flow patterns can be obtained in a confined microfluidic system with the variation in various operating parameters which include flow rate or density or viscosity of the fluids, interfacial tension between the fluids, and wettability near the boundaries. The design and optimal operation of the contemporary miniature technologies for various applications may naturally require an in depth fundamental understanding of the hydrodynamics of two-phase flows, e.g. gas-liquid or liquid-liquid systems. A detailed knowledge of the various flow morphologies inside the microscale setups under a varied range of operating parameters have been envisioned to develop various next-generation engineering prototypes.

Among all the multiphase flow configurations, the gas-liquid flow through a ‘Y’ or ‘T’ shaped microchannel with circular or rectangular cross-section have been the most widely studied. In contrast, the understanding of the similar liquid-liquid configurations has started gaining attention only in the recent years because of their complex but remarkable physics. It is now well understood that the typical viscosity and density stratifications together with the weaker capillarity at the interface make the dynamics of the liquid-liquid flows rather unique. In particular, the lower interfacial tension can facilitate smaller drop formation, which can be of significance for the microreactor design, formation of microemulsions, and enhanced heat and mass transfer applications. However, most of the previous studies related to the liquid-liquid flows inside the microchannels involved the effect of flow ratio of phases to obtain the different flow morphologies and mention the important role of the interfacial tension in droplet generation. A systematic study on the variations in the flow morphologies with interfacial tension at different flow ratios of the liquid phases and the subsequent pressure drop characteristics is rather an unexplored area of research, especially for the liquid-liquid flows inside moicrochannels.

Importantly, in most of the microscale setup, the production of well-ordered discrete droplets inside the microfluidic devices need to be transported, mixed or separated, reacted, emulsified, stored, and analysed in a controlled manner, targeting a specific application. In this direction, the efforts have been made to deploy the pressure driven two-phase microfluidic flows to generate the digitized flow patterns by tuning the flow rates, interfacial tension, and viscosity of the fluids, apart from changing the wettability criteria or geometry of the channels. However, the major limitations associated with these methodologies are, (a) droplets can be created only for a specific window of parametric space, (b) often the systems require complex geometrical arrangement, (c) requirements of

specially modified microchannel surfaces, or (d) addition of surfactants to aid the drop formation. In this direction, an efficient alternative can be the use of external field in breaking down the flow structures into the miniaturized ones having higher surface to volume ratio. Thus, in the recent years, extensive research activity has been observed to miniaturize the flow patterns with the help of external field inside microfluidic channel.

The knowledge and understanding gathered from the fundamental studies of microfluidic technology have always been integrated with other fields of science and technology, for developing miniature devices targeted for a specific application. Some of the applications can be as droplet based reactor, extraction in stratified flow, cell sorting, emulsification, production of nanomaterials, microfluidic based viscometer and tensiometer, and many more. Among other, the applications microfluidics have very often being employed for energy harvesting because it provides the scope for micro-very-large-scale integration (μ-VLSI) of large number of single units in order to maximize the generated output. The microfluidic based Kelvin water dropper, bio-systems, nanosystems, and fuel cells have been developed to convert various other forms of energy into the electrical ones inside the microfluidic setups. These studies have shown the possibility of mimicking a scientific phenomenon in macroscale to microscale inside a microchannel. Although there is always a constant need to improve the throughput and efficiency of such micro-devices. This necessity opens up a huge opportunity for exploring new alternative routes towards developing such energy harvesting devices and further improving the efficiency of the existing ones.

The objectives of the present work are as follows:

- Develop a flow pattern indicator for both gas-liquid and liquid-liquid systems inside a microchannel using artificial neural network (ANN).

- Study the effect of fluid properties and flow conditions on transition of liquid-liquid flow morphologies in microchannel.
- Study the effect of externally applied electric field on liquid-liquid flow morphologies in a microchannel.
- Study of liquid-liquid flow morphologies with and without electric field using numerical simulations.
- Develop a microfluidic device for harvesting of energy from light.

In this thesis, we aim to study the dynamics of pressure driven and field induced multiphase flow morphologies inside microfluidic channel with the help of experiments and simulations. In order to accomplish the above mentioned objectives, a systematic study has been performed and the whole work has been divided into five sections which are discussed below.

2. Prediction of flow pattern using neural network

In this chapter, we attempt to develop a flow pattern indicator capable of predicting all the flow patterns for gas-liquid and liquid-liquid systems in a microfluidic channel using probabilistic neural network (PNN) and comparing the results with its corresponding experimental data as well as with various existing analytical models in literature. Out of many neural networks present in literature, probabilistic neural network (PNN) has been chosen for the present study due to its speed in operation and accuracy in pattern recognition. The inbuilt code in MATLAB R2008a has been used to develop the PNN model. During training, superficial velocity of gas and liquid phase, channel diameter, angle of inclination and fluid properties such as density, viscosity and surface tension have been considered as the governing parameters of the flow pattern. Data has been collected from the literature for air-water and nitrogen-water flow through different circular

microchannel with internal diameters (d_h = 0.53, 0.25, 0.100 and 0.050 mm for nitrogen-water and 0.53, 0.22 mm for air-water). For the convenience of the study, the flow patterns available in the literature have been classified into six categories namely; bubbly, slug, annular, churn, liquid ring and liquid lump flow. Single PNN is unable to predict the flow pattern for the whole range (d_h = 0.53 mm – 0.050 mm) of microchannel diameter. In this scenario, two separate PNN models have been developed to predict the flow patterns of gas-liquid flow through different channel diameters, one for diameter ranging from 0.53 mm to 0.22 mm and another for 0.100 mm to 0.05 mm. The predicted map and their transition boundaries have been compared with the existing experimental data and found to be in good agreement. The accuracy in prediction of transition boundary obtained from available analytical models used for conventional channel is found to be less for all diameters of microchannel, as compared to the results reported in the present work. The percentage accuracy of PNN (~ 94% for d_h = 0.53 mm and ~ 73% for d_h = 0.100 mm) has also been found to be higher than the model based on Weber number (~ 86% for d_h = 0.53 mm and ~ 36% for d_h = 0.05 mm). After, the prediction of gas-liquid flow, we also conducted the prediction of flow patterns for liquid-liquid flow systems in similar fashion. While the overall prediction for liquid-liquid flow patterns also showed accuracy of ~91.37 %, which can be further improved by incorporating more number of data during training of PNN.

3. Capillary force mediated flow-patterns of oil-water microflows

In this chapter, we report the capillary and frictional force mediated transitions of morphologies of a liquid-liquid flow inside a microchannel with the help of experiments and computational fluid dynamic simulations. A number of steady and time-periodic flow patterns is reported with the variations in the interfacial tension, exchange of inlets, flow

ratio, and, viscosity ratio of the phases. Transitions from slug to plug to droplet to stratified flow patterns were obtained by tuning the interfacial tension. Progressive reduction in the interfacial tension transformed the bigger slugs into smaller plugs, plugs into droplets, and droplets into the stratified flow pattern. Interestingly, the simulations uncovered a non-monotonic and nonlinear reduction in pressure drop with the decrease in the interfacial tension. The change in the pressure drop was correlated to the variation in the slug or plug or droplet frequency of water at the outlet. The variations in the pressure drop were also associated with some distinctive transitions from dripping to jetting mechanism of water droplet ejection near the inlet. Apart from the interfacial tension, the viscosity stratification across the phases was also found to play an important role in converting the slug flow patterns into smaller plugs or droplets. The study also reports the parametric space in which the droplet flow patterns could be obtained inside a microchannel tuning the flow and viscosity ratios of the phases alongside the interfacial tension. The reported transitions of flow patterns and the pressure drop characteristics can be of significance in improving the efficiency of the futuristic microfluidic devices.

4. Electric field mediated spraying of miniaturized droplets

In the present chapter, we report a facile and non-invasive way to disintegrate a microdroplet into a string of further miniaturized ones under the influence of an external electrohydrodynamic (EHD) field inside a microchannel. The deformation and breakup of the droplet was engendered by the Maxwell's stress originating from the accumulation of induced and free charges at the oil-water interface. While at smaller field intensities (0 – 0.83 MV/m) the droplet deformed into a plug, at relatively higher field intensities (1.16 MV/m) a pair of droplets having opposite surface charge was formed. The charged droplets showed an interesting periodic bridging and breakup during their translation

motion across the channel. For even higher field intensities (1.19 – 3.56 MV/m), the entire droplet underwent dielectrophoresis towards one of the electrodes before experiencing a strong attractive force from the other electrode to deform into a shape of a Taylor cone. With progress in time, mimicking the electrospraying phenomenon, the cone-tip periodically ejected a string of miniaturized water droplets to form a microemulsion inside the channel. The frequency and size of the droplet ejection could be tuned by varying the applied field intensity. A water droplet of ~214 μm diameter could continuously eject droplets of size ~10 μm or even smaller to form a microemulsion inside the channel.

5. Discrete electric field mediated droplet splitting in microchannels

In this chapter, numerical simulations supplemented by experiments together uncovered that strategic integration of discrete electric fields in a non-invasive manner could substantially miniaturize the droplets into smaller parts in a pressure driven oil-water flow inside microchannels. The Maxwell's stress generated from the electric field at the oil-water interface could deform, stretch, neck, pin, and disintegrate a droplet into many miniaturized daughter droplets, which eventually ushered a one-step method to form water-in-oil microemulsion employing microchannels. The interplay between electrostatic, inertial, capillary, and viscous forces led to various pathways of droplet breaking, namely, fission, cascade, or Rayleigh modes. While a localized electric filed in the fission mode could split a droplet into a number of daughter droplets of smaller size, the cascade or the Rayleigh mode led to the formation of an array of miniaturized droplets when multiple electrodes generating different field intensities were ingeniously assembled around the microchannel. The droplets size and frequency could be tuned by varying the field intensity, channel diameter, electrode locations, interfacial tension, and flow ratio. The proposed methodology shows a simple strategy to transform a microdroplet into an array

of miniaturized ones inside a straight microchannel for enhanced mass, energy, and momentum transfer, and higher throughput.

6. Microfluidic energy harvester

Microfluidics have very often been employed for energy harvesting because it provides the scope for μ-VLSI of single units in order to maximize the output. In the fifth chapter, we show an alternative strategy to convert optical and mechanical energies into the electrical energy inside a microfluidic channel. A droplet of aqueous solution of sodium chloride (NaCl) generated electricity in presence of light when it was placed between two cylindrical electrodes of Cu and Cu_2O. The generated voltage varied with different kind of light sources and it was found that under solar illumination the generated voltage was maximum. Moreover, gold (Au) nanoparticles in the droplet enhanced the voltage generation due to their surface Plasmon resonance. The maximum generated voltage was found to be ~120 mV under solar illumination for a single droplet. The effect of different parameters like salt concentration, light source distance, droplet volume, nanoparticle loading etc. were also studied. In order to further enhance the voltage generation convex lens was also used to focus solar light on the droplet. The generated voltage could be increased using multiple droplets and a maximum of ~320 mV was achieved using five such droplets. Moreover, the maximum power density achieved in this case is ~13 $\mu w/cm^2$ under solar illumination. The similar phenomenon was also implemented in microchannel which increased the performance of the system. It was found that at a critical flow rate the generated voltage and current density was enhanced which led to a ~13-fold increment in power density. In this case, the effect of electrochemical photovoltaics, surface plasmon resonance, and streaming potential was combined to improve the efficiency of the device. Interestingly, the combined effect of the mentioned three effects could increase the

efficiency of the system to ~2%. Thus, the proposed microchannel based energy harvester is potential candidate for the large area solar energy harvester.

7. Conclusions and future scope of study

In summary, the thesis focusses on the theoretical and experimental understanding for production and control of flow morphologies inside microchannel. This work explores the effect of flow velocity ratio, viscosity and interfacial tension on the transition of oil-water flow morphologies inside the microfluidic devices. The spraying and breakup of miniaturized droplets in microchannel were also uncovered through experiments and numerical simulations. It was observed that the diameter and frequency of ejected microdroplets could be controlled with the variations in the intensity of the applied electric field. The proposed mechanisms of droplet formation can be exploited to develop the microfluidic emulsifiers in the near future. A microfluidic based solar energy harvester has been developed, which upon VLSI of a large number of units can produce high density powers for a number of futuristic applications. The outcome of this research can not only enhance the understanding of pressure and field driven microfluidics but also contribute to the applications related to energy harvesting, emulsification, microreactors, and multiphase unit operations, among others.

For future scope, the reported works can be extended in many different ways. Some of them are as follows:

- Oil-water flow in microchannel with expansion and contraction chamber.
- Electric and magnetic field induced two-phase flow in microchannel.
- Droplet based microreactors for production of nanomaterials.

Book authored:

1. Identification of flow pattern in microchannel using ANN, **S. Timung**, T. K. Mandal, Lap Lambert Academic Publishing, Germany, 2013. (**ISBN: 978-3-659-39774-5**)

Patent:

1. M. Bhattacharjee, **S. Timung**, T. K. Mandal and D. Bandyopadhyay, Microfluidic Electrical Energy Harvester, **2016, Indian Patent, 201631036408 A.**

Journal publications:

1. **S. Timung** and T. K. Mandal, Prediction of flow pattern of gas–liquid flow through circular microchannel using probabilistic neural network, Applied Soft Computing, 2013, **13** (4), 1674–1685.

2. Sharma, J. Chaudhuri, V. Kumar, **S. Timung**, T. K. Mandal and D. Bandyopadhyay, Digitization of two-phase flow patterns in a microchannel induced by an external AC field, RSC Adv., 2015, **5**, 29545–29551.

3. **S. Timung**, V. Tiwari, A. K. Singh, T. K. Mandal, D. Bandyopadhyay, Capillary force mediated flow patterns and non-monotonic pressure drop characteristics of oil-water microflows, Can. J. Chem. Eng., 2015, **93**, 1736–1743.

4. **S. Timung**, J. Chaudhuri, M. P. Borthakur, T. K. Mandal, G. Biswas, and D. Bandyopadhyay, Electric field mediated spraying of miniaturized droplets inside microchannel, Electrophoresis, 2016, **38**, 1450–1457.

5. J. Chaudhuri, **S. Timung**, C. B. Dandamudi, T. K. Mandal, and D. Bandyopadhyay, Discrete electric field mediated droplet splitting in microchannels: fission, cascade, and Rayleigh modes, Electrophoresis, 2017, **38**, 278–286.

6. M. Bhattacharjee, **S. Timung**, H. Nemade, T. K. Mandal and D. Bandyopadhyay, Nano-enabled Microfluidic Solar Energy Harvester with Surface Plasmon Resonance of Au Nanoparticles and Streaming Potential. (**Manuscript under preparation**)

7. S. Kumar, **S. Timung**, A. Ghosh, A. K. Dasmahapatra, and D. Bandyopadhyay, Dewetting of Microdroplets on Soft Surfaces for Immediate Digitization of Femtoliter Droplets. (**Manuscript under preparation**)

Conference Publications

1. **S. Timung**, V. Kumar, A. K. Singh, T. K. Mandal and D. Bandyopadhyay, Citrate-Stabilized Silver Nanoparticles Synthesis in Continuous-Flow Microreactor, International Conference on Advanced Nanomaterials and Nanotechnology, IIT Guwahati, Guwahati, India, 2013.

2. **S. Timung**, V. Tiwari, A. K. Singh, T. K. Mandal and D. Bandyopadhyay, Interfacial tension induced flow transitions in the two-phase flow inside microchannels, 22th National and 11th International ISHMT-ASME Heat and Mass Transfer Conference, IIT Kharagpur, Kharagpur, India, 2013.

3. **S. Timung**, A. Sharma, T. K. Mandal and D. Bandyopadhyay, Field induced flow behaviors of oil-water flow inside microfluidic channels, International Conference on MEMS and Sensors, IIT Madras, Chennai, India, 2014. **(Best paper award)**

4. J. Chaudhuri, **S. Timung**, T. K. Mandal and D. Bandyopadhyay, computational study of transition of oil-water flow morphology due to sudden contraction in microfluidic channel, COMSOL Conference, Bangalore, India, 2014.

5. S. Kumar, M. Bhattacharjee, **S. Timung**, A. K. Singh, T. K. Mandal, A. K. Dasmahapatra and D. Bandyopadhyay, Marangoni effect induced droplet motion for energy harvesting, emerging materials: characterization & application, CSIR-CGCRI, Kolkata, India, 2014.

CONTENTS

LIST OF TABLES

LIST OF FIGURES

NOMENCLATURE

a	arbitrary physical property
A	accuracy in prediction (%)
B	length of the minor axis
c_k	cost of misclassification
C_s, C_w, C_{Au}	concentration of salt, surfactant and gold nanoparticles, respectively (M or mol/L)
d	diameter of microchannel (μm)
d_d	droplet diameter (μm)
d_e	diameter of electrodes (μm)
d_h	hydraulic diameter of microchannel (μm)
d_{md}	diameter of microdroplet (μm)
d_s	distance from light source (cm)
D	deformation of droplet
D_f	droplet frequency (/s)
E	energy (eV)
F	free energy function
f_k	probability density function of k^{th} class
F_R	flow rate (ml/min)
$\mathbf{g}$	vector for acceleration due to gravity (m/s^2)
G	chemical potential
h_k	probability that a sample belongs to k^{th} class.
I	length of inlets (cm)
J_D	current density (mA/m^2)
K	classes or groups to which any random variables belongs.
K_L	specific electrical conductivity (S/m)
k	Boltzmann constant
Ir	Iridium
L	length of the major axis
l	length of microchannel (cm)
L_i	cumulative length of the interfacial contact between oil and water
$\dot{m}$	rate of mass transfer (kg/s)

n	ideality factor
N_{DD}	number of droplets
N_E	number of electrodes
p	pressure (Pa)
P_D	power density (W/m^2)
Pt	Platinum
q	charge density (C/m^3)
Q_r	ratio of input velocity of water to velocity of oil.
R	regression constant
r	radius of microchannel (μm)
r_d	radius of droplet (μm)
t	time (s)
t_h	duration of heating (s)
U	velocity of phases (m/s)
$\mathbf{u}$	velocity vector (m/s)
V	voltage generated (V)
w	width of electrodes
X	set of random variables

Greek letters

α	volume fraction
δ	thickness of the fluid interface (μm)
ε_o	permittivity of free space (N m^2/C^2)
ε_r	permittivity ratio
ε_w	relative permittivity of water
κ	curvature of the interface
λ	mixing free energy
η_{abs}	fraction of optical absorption
μ	viscosity of fluid (Pa s)
γ	interfacial tension (N/m)
ρ	density (Kg/m^3)
ψ	electric field (MV/m)

ϕ	level set parameter
ϕ_D	volume of droplet (μL)
θ	contact angle
χ	mobility of interface
ζ	zeta potential (V)

Dimensionless groups

Bo	Bond number
Bo_e	electric Bond number
Ca	capillary number
Re	Reynolds number
v	kinematic viscosity
We	Weber number

Subscripts

f	frequency
h, v	horizontal and vertical inlet
i, j	i^{th} and j^{th} fluid phase
r	ratio
w, o, c	water, oil, and continuous phase
G, *L*	gas and liquid phase

Acronyms

AC (DC)	alternating (direct) current
ANN	artificial neural network
ASTM	American Society for Testing and Materials
AuNPs	gold nanoparticles
CFD	computational fluid dynamics
CLSVOF	coupled level set volume of fluid
DEH	droplet energy harvester
DEP	dielectrophoretic
DI	de-ionized

DSI	direct solar illuminations
ECPV	electrochemical photovoltaics
EDX	energy dispersive x-ray
EHD	electrohydrodynamic
FESEM	field emission scanning electron microscope
FF	fill-factor
FFBP	feed forward back propagation
fps	frames per second
FSI	focused solar illuminations
GLS	Galerkin least-square
LBM	lattice-Boltzmann method
LDM	leaky dielectric model
LED	light emitting diode
MEH	microfluidic energy harvester
PDF	probability density function
PDMS	polydimethylsiloxane
PNN	probabilistic neural network
RBN	radial basis network
SDS	sodium dodecyl sulphate
SAED	selected area electron diffraction
SEM	scanning electron microscope
SERS	surface enhanced Raman scattering
SP	streaming potential (mV)
SPR	surface Plasmon resonance
SVM	support vector machine
TEM	transmission electron microscope
UV-Vis	ultraviolet visible
VLSI	very large scale integration
VOF	volume of fluid
XRD	x-ray diffraction

Chapter 1

Introduction

1.1 OVERVIEW

In the present thesis, we explore various pressure driven and external field driven two-phase flow phenomena inside a microchannel. Over the past few years, two-phase flow inside a microchannel have been broadly studied due to its wide variety of applications such as reactions,[1] cell sorting,[2] synthesis of micro/nanomaterials,[3,4] emulsification,[5,6] energy harvesting,[7,8] lab-on-a-chip, micro-electro-mechanical devices (MEMS),[9] and many more. They also offer several advantages as compared to their macroscopic counterparts, such as, (i) availability of higher surface to volume ratio for enhanced momentum, heat and mass transfer, (ii) ability to handle smaller volume of fluids, (iii) well controlled exothermic reactions, and (iv) suitability to hazardous chemicals.[10]

The hydrodynamics of two-phase flow in microchannel exhibits many exciting flow morphologies such as bubbly or droplet, plug, slug, slug-annular, annular and stratified flow.[11-14] These flow structures are employed for various targeted applications which can be developed by tuning the flow rate of phases,[11,13] viscosity,[15,16] interfacial tension,[5] channel geometry[17,18] and wall wetability.[6,14,19] For example, the creation of well-ordered discrete miniaturized droplets could be utilized for producing a monodispersed emulsion in food, pharmaceutical, and cosmetic industries.[20-24] These tunable flow structures can also offer control over the degree of mixing, which can alter the properties of the reacted products.[25-28] Apart from that, these flowing structures inside microchannels can be triggered by applying external field – electric and magnetic, which are capable of achieving several targeted tasks such as sorting,[29,30] fission,[31,32] fusion[33] and actuation[34] for various lab-on-a-chip[35,36] and point-of-care-diagnostic devices.[37,38] At the same time, many other researchers have shown various methodologies for energy harvesting employing fluid flow in microchannels.[7,8,39] The advantages of such devices or prototypes

are the possibility of very-large-scale-integration (VLSI) of individual units for large scale power generation.

1.2 OBJECTIVES AND LAYOUT OF THE THESIS

Microfluidic devices offer the possibility of scaling down the size of several existing scientific and industrially important equipment having an enhanced efficiency, such as, microreactors for reaction engineering,[40] microrheometers for rheological measurements,[41] and microemulsifiers for emulsification,[42] among many others. Due to this reason, it has attracted the attention of many professionals from both industries and academics, and have emerged as a promising area of research. Here, in the present thesis, we aim to explore:

- Various exciting features of two-phase flow systems inside microchannel and find various pathways for creating miniaturized flow structures by pressure and external field driven flows.
- Alternative ways for energy harvesting in a continuous flow microchannel which can have a major contribution in solving the present day energy crisis.

In order to make a systematic study, the whole work is divided into seven chapters, which are discussed here. In **Chapter 1**, we present a general overview of two-phase flow in microchannel. A brief literature review on pressure and external field driven two-phase flow in microchannels is described. It also covers a brief literature review on various phenomena and methodologies towards solar energy harvesting. Finally, the literature cited in this chapter has helped us in identifying various futuristic alternatives or directions of research related to two-phase flows in microchannel based on which the objectives and layout of the present work have been organised. In **Chapter 2**, we have developed a probabilistic neural network (PNN) model for prediction of flow patterns and their

transition boundaries for gas-liquid and liquid-liquid flow systems in microchannels. The percentage accuracy of PNN was found to be higher than the same obtained from various analytical models available in literature. In **Chapter 3**, with the help of experimental and computational study we uncover the effects of flow velocity ratio, interfacial tension and viscosity of phases on the flow patterns and pressure drop characteristics of an oil-water flow inside 'T' shaped microchannels. Transitions from slug, to plug, to droplet, to core-annular, to stratified flow patterns were obtained by tuning the oil-water interfacial tension. The study helps in identifying various pathways towards the size reduction of slug length or droplet diameter, which enable the availability of a higher surface-to-volume ratio inside microfluidic devices. In **Chapter 4**, with the help of experiments and simulations we show the deformation, breaking and spraying of droplets into smaller ones due to an applied electric field. The size of ejected droplets was found to decrease with the increase in applied electric field. In **Chapter 5**, through numerical simulations we show that a droplet flowing in a microchannel could undergo breaking multiple times with strategic placement of electrodes along the downstream of microchannel. The proposed methodology shows a simple approach to transform a microdroplet into an array of miniaturized ones inside a straight microchannel for enhanced mass, energy, and momentum transfer, and higher throughput. In **Chapter 6**, we have developed a microfluidic based prototype for energy harvesting from light. Here, we show that the generated power density could be enhanced by varying flow rates of the electrolyte and incorporating gold nanoparticles at various concentrations. Finally, in **Chapter 7,** we conclude the thesis with important outcomes from this work and the scopes of future research. A detailed literature review covering various features and applications of two-phase flow in microchannel have been presented below.

1.3 PREDICTION OF FLOW PATTERNS IN MICROCHANNEL

Green technology with adequate safety pertaining to the processes of the chemical industries are perhaps some of the major concerns to the modern civilization. In the present era, the advent of microprocesses such as the microreactors or microfluidic devices are envisioned to fulfil these requirements. In the past few decades, we have already observed the extensive use of microfabrication techniques in the electronic industries for miniaturization of devices alongside very large scale integration (VLSI) of the devices. Very often during operation these microstructure devices gets heated which hampers the optimum performance of the devices. In order to maintain a constant performance there is a need to constantly remove the excess heat from these devices. Frequently, under these circumstances the applications related to two-phase flow emerge. Some other applications related to the two-phase flows in a microchannel include chemical reactions, like fluorination, chlorination and bromination of organic compounds, hydrogen production by ethanol steam reforming, fluidization, compact heat exchanger and cooling system for various micro-electronics devices, air-condition and refrigeration, unit operations like evaporation, condensation and many more.[40,43-46] The design of such microstructure device would naturally require the complete knowledge of hydrodynamics of two-phase flow in such channel confinements.

Thus far, a number of experimental studies on two-phase flow through a microchannel have been reported in literature. However, most of them has been for gas-liquid flow and the same for the liquid-liquid flow systems are rather less. All of the past researchers have concentrated on the study of hydrodynamics of such flows, which includes the analyses on the flow patterns, holdup and pressure drop characteristics. The study of two-phase flow phenomena in a microchannel is perhaps incomplete without the knowledge of flow

morphologies under various conditions owing to their influence on the various hydrodynamic parameters such as holdup, pressure-drop, and mixing characteristics are significantly influenced by the flow pattern encountered.[47] In view of the above, a detailed literature survey has been performed to improve the understanding of the two-phase flows inside microfluidic channels,.

One of the earliest work on gas-liquid flow in microchannel was reported by Triplett et al.[11] where they studied the hydrodynamics of air-water flow through microchannel of two different geometry namely; circular and semi-triangular. For circular channel they have selected two diameter, - (i) 1.45 mm and (ii) 1.09 mm and hydraulic diameters for semi-triangular channels are 1.49 mm and 1.09 mm. They could identify some basic flow patterns such as bubbly, slug, slug-annular, annular and churn flow. The absence of stratified flow in their experiments suggested the dominance of surface tension over gravity in microchannels. Another important work by Kawahara et al.[48] reported the flow patterns of nitrogen-water flow through microchannel with diameter 100 μm and observed a series of different flow patterns occurring for the same flow condition. Essentially, this is the first work where such unsteady flow patterns were reported, which differs from usually observed flow patterns. The nomenclature of such flow patterns had to be made based on the probability of appearance of the flow configuration and named as slug-ring, ring-slug, semi-annular and multiple flow. Similar observations were observed by Chung and Kawaji[12] where they studied the effect of channel diameter on the flow pattern for nitrogen-water system. Experiments were conducted using mixture of nitrogen and water in circular channels with diameter of 530, 250, 100, and 50 μm. The flow pattern for d_h = 530 and 250 μm have found to be similar to those observed by Triplett et al.[11] While the unsteady flow patterns were observed for d_h = 100 and 50 μm which were similar to

Kawahara et al.[48] Similar sets of steady and unsteady flow patterns were also observed by Saisorn and Wongwise[49]. These observations clearly depict the difference in flow patterns observed in a microchannel with diameter, $d_h \geq 200$ μm and $d_h < 200$ μm. As the channel diameter decreases the effect of surface and viscous forces becomes dominant over gravity and inertial forces, which can be among the major reasons for such difference in flow patterns.

From literature, it has been observed that the hydrodynamics of multiphase flow inside a microchannel with diameter, $d_h < 200$ μm is still an open area of research because none of the physical models could clearly predict the experimental observations. Further, the classical models for the two-phase flow regimes applicable to conventional channels very often fail to predict the flow pattern occurring in microchannels[50-52] While the flow patterns observed in experimental results[11,12,48,53] shows some deviation from the classical models clearly and it indicates that the mechanism of formation and its dominant forces inside a microchannel are quite different from that of conventional channels. This highlights the necessity of a separate model, which can be employed for the prediction of flow patterns in microchannel. In this regard, Akbar et al.[54] presented a flow regime map based on Weber number of both the fluids as co-ordinates which divides the whole map into four main regions – e.g. surface tension-dominated, annular, froth or dispersed, and transition. The observations have been found to be in good agreement for air-water flow in circular microchannel with diameter, $d_h \geq 200$ μm. Also, with development of CFD software such as FLUENT, various numerical technique for two-phase flow models have been reported.[55] However, as different flow patterns are governed by different forces and mechanisms, each flow transition calls for separate models.[56] Apart from analytical and numerical models, one of the alternative for prediction of two-phase flow patterns could

be by employing neural networks. Although neural networks have been employed to predict flow patterns in conventional channels[56-60], their applicability for flow patterns in microchannel is yet to be done.

1.4 LIQUID-LIQUID FLOW IN MICROCHANNEL

Interfacial morphologies of two-layer flows in microfluidic devices have been studied extensively in recent times because of their diverse applications in the areas of bio-analysis,[36] multiphase extraction,[61] emulsification,[62] MEMS devices,[63] and microreactors,[64] among many others. Microfluidic devices are considered superior to their macroscopic analogues primarily because of the availability of higher surface-to-volume ratio, smaller throughput leading to easier control of the operating parameters, and reduction in operating cost in the processes where costly chemicals are in use.[10] Microscale two-phase flows also manifest exciting interfacial flow patterns in the form of slug, plug, core-annular, stratified, wavy, bubbly, and drop-dispersions, which have fascinated many researchers. Previous studies uncovered a host of exceptional behaviours of two-phase microflows, for example: generation of microscale droplets or bubble dispersions, or chaotic interfacial patterns,[65] folding and swirling of interfacial threads,[66,67] formation of vesicles,[68] mixing,[15] and particle synthesis.[18] A number of review articles have summarized the various scientific and technological aspects of the two-layer flows inside microchannels.[10,69]

Among all the multiphase configurations, gas-liquid flow through a ‘Y’ or ‘T’ shaped microchannel with a circular or rectangular cross-section has been the most widely studied.[12,48,70] In contrast, the understanding of similar liquid-liquid configurations has started gaining attention only in recent years, because of

their complex but remarkable physics. A review by Joseph et al.[71] ably distinguished the salient features of liquid-liquid flows as compared to similar gas-liquid flows while discussing the open issues in oil-water flows. It is now well understood that the typical viscosity and the density stratifications, together with weaker capillarity at the interface, make the dynamics of liquid-liquid flows rather unique. In particular, the lower interfacial tension can facilitate smaller drop formation, which can be of significance for microreactor design, formation of microemulsions, and enhanced heat and mass transfer applications.

Apart from focus on the technological aspects, the fundamental mechanisms of drop, plug, or slug release of the two-phase flows inside microfluidic devices have attracted significant attention in recent years.[72] The 'dripping,' 'jetting,' and 'squeezing' mechanisms of the droplet, plug, or slug formation due to the interplay between the inertia, capillary, and shear forces have also been investigated.[72] For example, Menech et al.[73] studied the steady and transient characteristics of squeezing, dripping, and jetting transitions with the variations in the capillary number. In the dripping mechanism, the droplets or plugs are ejected near the inlet, whereas the jetting involves extension of a fluid thread downstream of the channel before droplets are pinched off from the main thread. The flow morphologies originating from the dominance of capillary, viscous, or weak inertial forces and the subsequent pressure drop characteristics have also been studied in detail.[14,74,75] For example, Zhao et al.[74] showed the transitions in flow patterns at the T-junction of a microchannel with the Weber number by varying the superficial velocities of the oil-water phases. Tice et al.[15] showed the variations in plug flow patterns with phase viscosity changes in a liquid-liquid configuration inside a microchannel. Subsequently, Kashid et al.[75] and Salim et al.[14] showed the transitions in flow-patterns

alongside interesting pressure drop characteristics with the variation in the phase flow rates inside glass and quartz microchannels for an oil-water system. These two studies alongside the study from Jovanović et al.[76] have developed a modified Lockhart–Martinelli correlation to predict the pressure drop characteristics for the liquid-liquid flows, in which the flow patterns, wettability of channels, interfacial area, and shape and size of the channels, are considered to be important factors. Indeed, a few other studies have uncovered that the wettability of the liquids on the channel walls,[77] interfacial tension between the liquid layers,[15,78-81] and the geometry of the microchannel[13,75,82] play crucial roles in the development of flow patterns of liquid-liquid microfluidic flows. A recent work by Foroughi and Kawaji[83] highlighted some unique transitions in the flow patterns with the changeover in the balance of the inertial, viscous, and interfacial forces inside a flow-focussed microchannel with the variation in the oil-to-water flow ratio.

However, most previous studies related to the liquid-liquid flows inside the microchannels vary the phase flow rates to obtain different flow morphologies and mention the important role of interfacial tension in droplet generation. A systematic study on the variations in flow morphologies with interfacial tension and subsequent pressure drop characteristics is a relatively unexplored area of research, especially for liquid-liquid flows inside microchannels.

1.5 ELECTRIC FIELD MEDIATED SPRAYING OF MINIATURIZED DROPLETS

Droplet or digital microfluidics is poised to play a pivotal role in improving the efficiency of a wide range of applications which include flow-cytometry,[63] microreactors,[64] emulsification,[6] and energy harvesting.[7] Fundamentally, the usefulness of droplet

microfluidics relies on the production of well-ordered discrete flow patterns inside the microfluidic devices, which are to be transported, mixed or separated, reacted, emulsified, stored, and analyzed in a controlled manner, targeting a specific application. In this direction, the efforts have been made to deploy pressure driven two-phase microfluidic flows to generate the digitized flow patterns by tuning the flow rates,[13,84,85] interfacial tension,[6,84] and viscosity of the fluids,[16,84] apart from changing the wettability criteria[6,19] or geometry[17,86] of the channels. However, the major limitations associated with these methodologies are, (a) droplets can be created only for a specific window of parametric space, (b) often the systems require complex geometrical arrangement, (c) requirements of specially modified microchannel surfaces, or (d) addition of surfactants to aid the drop formation. In this regard, an efficient alternative can be the use of external field in breaking down the flow structures into the miniaturized ones having higher surface to volume ratio. Thus, in the recent years, extensive research activity has been observed to miniaturize the flow patterns with the help of external field inside the microchannels to improve the performance of the microfluidic devices for enhanced momentum, heat, and mass transfer.[31,87-90]

Previous studies suggested that a discrete water droplet suspended in a continuous oil medium could deform into interesting shapes under the influence of an external electrohydrodynamic (EHD) field. [87,91] Accumulation of bound and free charges at the oil-water interface due to the mismatch of dielectric permittivity and the electrical conductivity of the fluids was found to be the major reasons behind these deformations.[92] In some of their pioneering experiments, Allan and Mason[89] showed that the conducting droplets of macroscopic dimensions could be deformed into prolate shape while perfectly dielectric droplets deformed into oblate shape. Later, Taylor[93] proposed a leaky dielectric

model (LDM) to explain these experimental results and inferred that the deformation could depend upon a number of process parameters such as the oil-water interfacial tension, applied field intensity alongside the ratios of the electrical conductivity, dielectric permittivity, and viscosity of the fluid mediums. Furthering these observations, other studies revealed that external EHD field could even break a macroscopic water droplet into smaller ones when the field intensity is increased beyond a critical limit.[88,90,93,94] However, the physics associated with the EHD multiphase flows in the microscale can be very different from their macroscopic counterparts due to the complex interplay originating from the electrical, viscous, inertial, and surface tension forces.

In this direction, a number of recent studies indicated that the use of external field can also be an efficient alternative to digitize the flow patterns.[95-97] For example, an alternating current (AC) field could be integrated with the microchannels to form emulsions with miniaturized droplets.[98] Numerical simulations also uncovered the strategies to transform a stratified oil-water flow in a microchannel into droplet flow by applying direct current (DC) or AC fields.[99,100] Interesting physical phenomena such as attraction and pinning of water slugs towards electrodes, phase separation due to droplet coalescence, simultaneous droplet splitting, coalescence and sorting have also been studied in detail.[17,31,33,101,102] In the past few decades, the theoretical modeling of oil-water flows coupled with the EHD field have also overcome the complexities associated with tracking of the intricate interfacial methodologies in presence of an external field. Poisson's equation for the electric field combined with the Stokes' equation for the flows were solved numerically for the microscopic flows to analyze the EHD field induced breakup of droplets.[99,100,103] The coupling between the hydrodynamics and the electric field has been performed by integrating the Maxwell's stresses in the governing equations and in the boundary

conditions. The finite difference, finite element, or finite volume methods coupled with the volume-of-fluid (VOF), volume of fluid coupled with level-set (CLSVOF),[104-107] Lattice-Boltzmann (LBM),[108] or phase field methods[109-112] were employed to solve the entire system of transport equations with appropriate boundary conditions to uncover the spatiotemporal dynamics of the two-phase systems.

1.6 ELECTRIC FIELD MEDIATED DROPLET SPLITTING IN MICROCHANNEL

Miniaturization of flow patterns inside the microfluidic environment is expected to improve the performance of multifarious applications which include microreactors,[1,113] micromixers,[114] cell analysis,[63,115] MEMS devices,[36,116] bio-analytical tools,[117,118] theranostic,[3,4,119] and energy harvesting[7] devices. For example, a pressure driven two-phase oil-water microflow shows interesting transition from stratified to core-annular, slug, plug, or droplet flow morphologies with significantly higher surface area per unit mass when the velocities or viscosity of the phases, interfacial tension, or the wettability of the fluids are systematically varied.[120-123] These microscale flow patterns, attuned to the interplay between the dominant capillary and frictional forces over the weak inertial and gravitational forces,[28,124-128] are harnessed for synthesis of micro/nano materials,[3,18,113] multicomponent mixing[113] and preparation of multiphase dispersions[62,68] with improved efficiency. However, the slow diffusive nature of transport in the highly confined microscale devices limits their efficiency as compared to their macroscopic counterparts where all the diffusive, convective, and turbulent modes are available to adjust the transport properties for a better efficiency. In this situation, the technological feasibility of many of the microscale processes is strongly dependent on, (a) efficient momentum, energy, and mass transport through digitization and subsequent miniaturization of flow

patterns, and (b) increase in the throughput of the processes to match their macroscopic counterparts after very large scale integration of numerous microscale units.[35,69,129,130] Thus, extensive research activity has been observed in recent years to digitize the flow patterns alongside improving the throughput of the microscale prototypes.[11,35,48,55,69,82,129-133]

Previous works on the gas-liquid[11,48,55,131] and liquid-liquid[82,132,134] microflows suggest that regular pressure driven flows are unable to meet many of the aforementioned expectations so far. Alternatively, recent studies indicate that the use of external fields to maneuver the balance of the other forces inside the microfluidic devices can be another paradigm to be explored for a better efficiency and performance.[32,103-105,108,133,135-138] For example, external electric field have been employed to engender droplet coalescence,[33,139,140] splitting and sorting[31,139-141] where the accumulation of induced or free charges at the interface plays a crucial role in developing the miniaturized flow morphologies. There are evidences that the electrohydrodynamic (EHD) stress can be strong enough to deform a soft-interface to produce miniaturized flow structures with significantly higher surface to volume ratio.[96,97,142] The major advantage in this methodology is its non-invasive nature of operation, which points to the fact that they can be integrated easily to any of the microfluidic applications without influencing the other process parameters. For example, a few recent studies report that integrating the alternating (AC)[98,100] or direct (DC)[99] current electric fields with the microfluidic devices either in local[98-100] or non-local[33] manner can digitize the two-phase flow patterns, which in turn can improve throughput of the microfluidic processes.

1.7 MICROFLUIDIC SOLAR ENERGY HARVESTER

Rapid progress in the technologies related to the micro- or nano-scale fabrication and characterization have enabled the development of micro-power harvesters suitable for smart phones, calculators, health-care devices, watches, ipods, laptops, computers, micro/nano fluidic devices, and wireless sensors.[143-149] These economic, scalable, proficient, and eco-friendly technologies are envisioned to harvest high-density power from various natural resources to sustain the energy demands of the contemporary techno-savvy society.[143-145] Arguably, this journey started about a century back with the inventions of photovoltaic effect,[150,151] solar cells,[152] and photoelectric effect,[153,154] which allowed the conversion of naturally abundant solar energy into the electrical power at usable efficiencies.[155-159] Subsequently, the inventions of multi-junction solar cells,[160] silicon based first[161] and second[161,162] generation solar cells, helped in improving the efficiency to cater the needs of multifarious portable technologies. Later, the third generation solar devices[163-165] such as the organic[166-168] or perovskite cells[169] emerged to address the issues associated with the silicon based solar cells such as eco-friendliness, stability, and efficiency. Since then the focus has been to bring in the specialities of micro or nanoscale wires, particles, or tubes of functional materials[170-173] to develop the next generation photo-electrochemical, dye-sensitized, photovoltaic, and micro-nano fluidics based cells.[174-180] Herein we report the development of a pair of micro-power harvesters in which one is composed of a microdroplet while the other one is made of a microfluidic channel. The proposed energy harvesters are capable of converting solar and mechanical energy into the electrical one at usable efficiencies when integrated with Schottky barrier metal-semiconductor electrodes.

The Schottky-junction solar cells composed of metal-semiconductors such as the Cu-Cu_2O are well known for their lower cost, high minority carrier diffusion length, and higher absorption coefficient in the visible region at a theoretical efficiency of ~ 20%.[181-185] Further, since the p-type Cu_2O has a bandgap of ~2 eV, the Cu-Cu_2O solar energy harvesters show higher efficiencies in the yellow to near UV region than the Si based solar cells.[181-183,186,187] Thus, in the past, variety of solar cells have been constructed using metal/p-Cu_2O, n-ZnO/p-Cu_2O, or n-CdO/p-Cu_2O.[184,185,188,189] However, the maximum efficiency of the reported devices is found to be ~2%.[184,190] A few recent works have reported that the heterojunction cells can be one of the ways to address this issue.[188,189,191,192]

In parallel to the developments of the different kinds of solar cells, the present era has also experienced the emergence of different kinds of micro-power harvesters where the mechanical energy is converted to the electrical one.[193-196] These energy harvesters exploits various fluid mechanical phenomena, for example, droplet actuation,[195-197] reverse electro-wetting,[198] or piezoelectric effect[39] to harvest high density electrical power. The typical power densities of the micro-power harvesters are envisioned to match the naturally abundant radio frequency (~1 $\mu W/cm^2$), solar irradiation (~100 mW/cm^2), ambient illumination (~100 $\mu W/cm^2$), thermoelectric devices (~60 $\mu W/cm^2$), vibration generators (~10 – 800 $\mu W/cm^3$), or ambient air flow (~1 mW/cm^2).[199]

In summary, the thesis initiates with the understanding of the two-phase flows in microfluidic channel. Following this, we explore the various strategies to create miniaturized droplets by applying electric field. The outcome of this study can be of significance in the development of droplet microfluidic devices for the applications such

as mixing, emulsification, microreactors, μ-VLSI, and miniaturization, among others. At the end, we also show the integration of a proof-of-concept microfluidic prototype for solar energy harvesting.

1.8 REFERENCES

1. K. F. Jensen, Chemical Engineering Science **56**, 293 (2001).
2. J. Autebert, B. Coudert, F.-C. Bidard, J.-Y. Pierga, S. Descroix, L. Malaquin, and J.-L. Viovy, Methods **57**, 297 (2012).
3. L. Capretto, D. Carugo, S. Mazzitelli, C. Nastruzzi, and X. Zhang, Advanced Drug Delivery Reviews **65**, 1496 (2013).
4. K. S. Krishna, Y. Li, S. Li, and C. S. S. R. Kumar, Advanced Drug Delivery Reviews **65**, 1470 (2013).
5. L. Shui, A. van den Berg, and J. C. T. Eijkel, Lab on a Chip **9**, 795 (2009).
6. J. H. Xu, S. W. Li, J. Tan, Y. J. Wang, and G. S. Luo, Langmuir **22**, 7943 (2006).
7. A. G. Marin, W. van Hoeve, P. Garcia-Sanchez, L. Shui, Y. Xie, M. A. Fontelos, J. C. T. Eijkel, A. van den Berg, and D. Lohse, Lab on a Chip **13**, 4503 (2013).
8. E. Yıldırım and H. Külah, Microfluidics and Nanofluidics **13**, 107 (2012).
9. K. A. Cook-Chennault, N. Thambi, and A. M. Sastry, Smart Materials and Structures **17**, 043001 (2008).
10. V. Kumar, M. Paraschivoiu, and K. D. P. Nigam, Chemical Engineering Science **66**, 1329 (2011).
11. K. A. Triplett, S. M. Ghiaasiaan, S. I. Abdel-Khalik, and D. L. Sadowski, International Journal of Multiphase Flow **25**, 377 (1999).

12. P. M. Y. Chung and M. Kawaji, International Journal of Multiphase Flow **30**, 735 (2004).

13. H. Foroughi and M. Kawaji, International Journal of Multiphase Flow **37**, 1147 (2011).

14. A. Salim, M. Fourar, J. Pironon, and J. Sausse, The Canadian Journal of Chemical Engineering **86**, 978 (2008).

15. J. D. Tice, A. D. Lyon, and R. F. Ismagilov, Analytica Chimica Acta **507**, 73 (2004).

16. T. Cubaud, Physical Review E **80**, 026307 (2009).

17. A. Carlson, M. Do-Quang, and G. Amberg, International Journal of Multiphase Flow **36**, 397 (2010).

18. M. Yamada, S. Doi, H. Maenaka, M. Yasuda, and M. Seki, Journal of Colloid and Interface Science **321**, 401 (2008).

19. C. Choi, D. I. Yu, and M. Kim, Experimental Thermal and Fluid Science **35**, 1086 (2011).

20. O. Skurtys and J. M. Aguilera, Food Biophysics **3**, 1 (2008).

21. H. Christian, Journal of Physics D: Applied Physics **46**, 114008 (2013).

22. G. T. Vladisavljević, N. Khalid, M. A. Neves, T. Kuroiwa, M. Nakajima, K. Uemura, S. Ichikawa, and I. Kobayashi, Advanced Drug Delivery Reviews **65**, 1626 (2013).

23. Q. Xu, M. Hashimoto, T. T. Dang, T. Hoare, D. S. Kohane, G. M. Whitesides, R. Langer, and D. G. Anderson, Small **5**, 1575 (2009).

24. J. Wan, A. Bick, M. Sullivan, and H. A. Stone, Advanced Materials **20**, 3314 (2008).

25. V. Sebastian Cabeza, S. Kuhn, A. A. Kulkarni, and K. F. Jensen, Langmuir **28**, 7007 (2012).

26. C.-X. Zhao, L. He, S. Z. Qiao, and A. P. J. Middelberg, Chemical Engineering Science **66**, 1463 (2011).

27. S. Li, J. Xu, Y. Wang, and G. Luo, Langmuir **24**, 4194 (2008).

28. A. Gunther and K. F. Jensen, Lab on a Chip **6**, 1487 (2006).

29. I. Doh and Y.-H. Cho, Sensors and Actuators A: Physical **121**, 59 (2005).

30. K. H. Kang, Y. Kang, X. Xuan, and D. Li, Electrophoresis **27**, 694 (2006).

31. D. R. Link, E. Grasland-Mongrain, A. Duri, F. Sarrazin, Z. Cheng, G. Cristobal, M. Marquez, and D. A. Weitz, Angewandte Chemie International Edition **45**, 2556 (2006).

32. J. D. Sherwood, Journal of Fluid Mechanics **188**, 133 (1988).

33. A. R. Thiam, N. Bremond, and J. Bibette, Physical Review Letters **102**, 188304 (2009).

34. M. Pollack, A. Shenderov, and R. Fair, Lab on a Chip **2**, 96 (2002).

35. H. A. Stone, A. D. Stroock, and A. Ajdar, Annual Review of Fluid Mechanics **36**, 381 (2004).

36. M. A. Burns *et al.*, Science **282**, 484 (1998).

37. C. D. Chin, V. Linder, and S. K. Sia, Lab on a Chip **12**, 2118 (2012).

38. F. A. Gomez, Bioanalysis **5**, 1 (2013).

39. S. P. Beeby, R. Torah, M. Tudor, P. Glynne-Jones, T. O'donnell, C. Saha, and S. Roy, Journal of Micromechanics and microengineering **17**, 1257 (2007).

40. P. Lob, H. Lowe, and V. Hessel, Journal of Fluorine Chemistry **125**, 1677 (2004).

41. M. Zou, S. Cai, Z. Zhao, L. Chen, Y. Zhao, X. Fan, and S. Chen, Review of Scientific Instruments **86**, 104302 (2015).

42. R. K. Shah *et al.*, Materials Today **11**, 18 (2008).

43. W. Cai, F. Wang, A. van Veen, C. Descorme, Y. Schuurman, W. Shen, and C. Mirodatos, International Journal of Hydrogen Energy **35**, 1152 (2010).

44. B. Potic, S. R. A. Kersten, M. Ye, M. A. van der Hoef, J. A. M. Kuipers, and W. P. M. van Swaaij, Chemical Engineering Science **60**, 5982 (2005).

45. S. Saisorn and S. Wongwises, Experimental Thermal and Fluid Science **32**, 748 (2008).

46. C.-Y. Yang and C.-C. Shieh, International Journal of Multiphase Flow **27**, 1163 (2001).

47. S. Saisorn and S. Wongwises, International Communications in Heat and Mass Transfer **35**, 833 (2008).

48. A. Kawahara, P. M. Y. Chung, and M. Kawaji, International Journal of Multiphase Flow **28**, 1411 (2002).

49. S. Saisorn and S. Wongwises, Experimental Thermal and Fluid Science **34**, 454 (2010).

50. J. M. Mandhane, G. A. Gregory, and K. Aziz, International Journal of Multiphase Flow **1**, 537 (1974).

51. D. Barnea, International Journal of Multiphase Flow **13**, 1 (1987).

52. Y. Taitel and A. E. Dukler, AIChE Journal **22**, 47 (1976).

53. E. Rahim, R. Revellin, J. Thome, and A. Bar-Cohen, International Journal of Multiphase Flow **37**, 12 (2011).

54. M. K. Akbar, D. A. Plummer, and S. M. Ghiaasiaan, International Journal of Multiphase Flow **29**, 855 (2003).

55. R. M. Santos and M. Kawaji, International Journal of Multiphase Flow **36**, 314 (2010).

56. H. Sharma, G. Das, and A. N. Samanta, AIChE Journal **52**, 3018 (2006).

57. J. E. Julia, B. Ozar, J.-J. Jeong, T. Hibiki, and M. Ishii, International Journal of Heat and Fluid Flow **32**, 164 (2011).

58. Y. Mi, M. Ishii, and L. H. Tsoukalas, Nuclear Engineering and Design **204**, 87 (2001).

59. T. Tambouratzis and I. Pazsit, Annals of Nuclear Energy **37**, 672 (2010).

60. W. Zhang, F. Y. Shih, N. Jin, and Y. Liu, International Journal of Multiphase Flow **36**, 793 (2010).

61. M. Tokeshi, T. Minagawa, K. Uchiyama, A. Hibara, K. Sato, H. Hisamoto, and T. Kitamori, Analytical Chemistry **74**, 1565 (2002).

62. S. L. Anna, N. Bontoux, and H. A. Stone, Applied Physics Letters **82**, 364 (2003).

63. J. Skommer, J. Akagi, K. Takeda, Y. Fujimura, K. Khoshmanesh, and D. Wlodkowic, Biosensors and Bioelectronics **42**, 586 (2013).

64. K. F. Jensen, Chemical Engineering Science **56**, 293 (2001).

65. R. Dreyfus, P. Tabeling, and H. Willaime, Physical Review Letters **90**, 144505 (2003).

66. T. Cubaud and T. G. Mason, Physical Review Letters **96**, 114501 (2006).

67. T. Cubaud and T. G. Mason, Physical Review Letters **98**, 264501 (2007).

68. T. Thorsen, R. W. Roberts, F. H. Arnold, and S. R. Quake, Physical Review Letters **86**, 4163 (2001).

69. L. Shui, J. C. T. Eijkel, and A. van den Berg, Advances in Colloid and Interface Science **133**, 35 (2007).

70. K. A. Triplett, S. M. Ghiaasiaan, S. I. Abdel-Khalik, and D. L. Sadowski, International Journal of Multiphase Flow **25**, 377 (1999).

71. D. D. Joseph, R. Bai, K. P. Chen, and Y. Y. Renardy, Annual Review of Fluid Mechanics **29**, 65 (1997).

72. C. Cramer, P. Fischer, and E. J. Windhab, Chemical Engineering Science **59**, 3045 (2004).

73. M. De Menech, P. Garstecki, F. Jousse, and H. A. Stone, Journal of Fluid Mechanics **595**, 141 (2008).

74. Y. Zhao, G. Chen, and Q. Yuan, AIChE Journal **52**, 4052 (2006).

75. M. N. Kashid and D. W. Agar, Chemical Engineering Journal **131**, 1 (2007).

76. J. Jovanovic, W. Zhou, E. V. Rebrov, T. A. Nijhuis, V. Hessel, and J. C. Schouten, Chemical Engineering Science **66**, 42 (2011).

77. R. Raj, N. Mathur, and V. V. Buwa, Industrial & Engineering Chemistry Research **49**, 10606 (2010).

78. J. Chen, S. Wang, and S. Cheng, Chemical Engineering Science **84**, 706 (2012).

79. T. Cubaud, B. M. Jose, S. Darvishi, and R. Sun, International Journal of Multiphase Flow **39**, 29 (2012).

80. J. H. Xu, P. F. Dong, H. Zhao, C. P. Tostado, and G. S. Luo, Langmuir **28**, 9250 (2012).

81. J. H. Xu, S. W. Li, J. Tan, Y. J. Wang, and G. S. Luo, AIChE Journal **52**, 3005 (2006).

82. A.-L. Dessimoz, L. Cavin, A. Renken, and L. Kiwi-Minsker, Chemical Engineering Science **63**, 4035 (2008).

83. H. Foroughi and M. Kawaji, International Journal of Multiphase Flow **37**, 1147 (2011).

84. S. Timung, V. Tiwari, A. K. Singh, T. K. Mandal, and D. Bandyopadhyay, The Canadian Journal of Chemical Engineering **93**, 1736 (2015).

85. T. Ward, M. Faivre, M. Abkarian, and H. A. Stone, Electrophoresis **26**, 3716 (2005).

86. D. R. Link, S. L. Anna, D. A. Weitz, and H. A. Stone, Physical Review Letters **92**, 054503 (2004).

87. H. Sato, N. Kaji, T. Mochizuki, and Y. H. Mori, Physics of Fluids (1994-present) **18**, 127101 (2006).

88. C. G. Garton and Z. Krasucki, Proceedings of the Royal Society of London A: Mathematical, Physical and Engineering Sciences **280**, 211 (1964).

89. R. S. Allan and S. G. Mason, Proceedings of the Royal Society of London A: Mathematical, Physical and Engineering Sciences **267**, 45 (1962).

90. S. Torza, R. G. Cox, and S. G. Mason, Philosophical Transactions of the Royal Society of London A: Mathematical, Physical and Engineering Sciences **269**, 295 (1971).

91. Y. Lin, Electrophoresis **34**, 736 (2013).

92. M. N. Reddy and A. Esmaeeli, International Journal of Multiphase Flow **35**, 1051 (2009).

93. G. Taylor, Proceedings of the Royal Society of London A: Mathematical, Physical and Engineering Sciences **291**, 159 (1966).

94. G. Taylor, Proceedings of the Royal Society of London A: Mathematical, Physical and Engineering Sciences **280**, 383 (1964).

95. S. Lecuyer, W. D. Ristenpart, O. Vincent, and H. A. Stone, Applied Physics Letters **92**, 104105 (2008).

96. B. Ray, P. D. S. Reddy, D. Bandyopadhyay, S. W. Joo, A. Sharma, S. Qian, and G. Biswas, Electrophoresis **32**, 3257 (2011).

97. D. Bandyopadhyay, P. D. Reddy, A. Sharma, S. Joo, and S. Qian, Theoretical and Computational Fluid Dynamics **26**, 23 (2012).

98. S. H. Tan, B. Semin, and J.-C. Baret, Lab on a Chip **14**, 1099 (2014).

99. A. Sharma, V. Tiwari, V. Kumar, T. K. Mandal, and D. Bandyopadhyay, Electrophoresis **35**, 2930 (2014).

100. A. Sharma, J. Chaudhuri, V. Kumar, S. Timung, T. K. Mandal, and D. Bandyopadhyay, RSC Advances **5**, 29545 (2015).

101. J. D. Wehking, L. Chew, and R. Kumar, Applied Physics Letters **103**, 054101 (2013).

102. X. Chen, Y. Song, D. Li, and G. Hu, Physical Review Applied **4**, 024005 (2015).

103. O. Vizika and D. A. Saville, Journal of Fluid Mechanics **239**, 1 (1992).

104. J. Q. Feng and T. C. Scott, Journal of Fluid Mechanics **311**, 289 (1996).

105. J. M. Lopez-Herrera, S. Popinet, and M. A. Herrada, Journal of Computational Physics **230**, 1939 (2011).

106. A. Fernández, G. Tryggvason, J. Che, and S. L. Ceccio, Physics of Fluids (1994-present) **17**, 093302 (2005).

107. J. Chaudhuri, S. Timung, C. B. Dandamudi, T. Kumar Mandal, and D. Bandyopadhyay, Electrophoresis, **38** 278 (2017).

108. J. Zhang and D. Y. Kwok, Journal of Computational Physics **206**, 150 (2005).

109. D. Jacqmin, Journal of Computational Physics **155**, 96 (1999).

110. V. E. Badalassi, H. D. Ceniceros, and S. Banerjee, Journal of Computational Physics **190**, 371 (2003).

111. Y. Lin, P. Skjetne, and A. Carlson, International Journal of Multiphase Flow **45**, 1 (2012).

112. I. Steinbach, L. Zhang, and M. Plapp, Acta Materialia **60**, 2689 (2012).

113. X. Niu, M. Zhang, J. Wu, W. Wen, and P. Sheng, Soft Matter **5**, 576 (2009).

114. J. D. Tice, H. Song, A. D. Lyon, and R. F. Ismagilov, Langmuir **19**, 9127 (2003).

115. H. N. Joensson and H. Andersson Svahn, Angewandte Chemie International Edition **51**, 12176 (2012).

116. H. Tsuchiya, M. Okochi, N. Nagao, M. Shikida, and H. Honda, Sensors and Actuators B: Chemical **130**, 583 (2008).

117. M. Nakano, N. Nakai, H. Kurita, J. Komatsu, K. Takashima, S. Katsura, and A. Mizuno, Journal of Bioscience and Bioengineering **99**, 293 (2005).

118. V. Taly, D. Pekin, A. E. Abed, and P. Laurent-Puig, Trends in Molecular Medicine **18**, 405 (2012).

119. D. Wlodkowic and J. M. Cooper, Analytical and Bioanalytical Chemistry **398**, 193 (2010).

120. P. Garstecki, M. J. Fuerstman, H. A. Stone, and G. M. Whitesides, Lab on a Chip **6**, 437 (2006).

121. A. Gupta and R. Kumar, Microfluidics and Nanofluidics **8**, 799 (2010).

122. X.-B. Li, F.-C. Li, J.-C. Yang, H. Kinoshita, M. Oishi, and M. Oshima, Chemical Engineering Science **69**, 340 (2012).

123. R. Ledesma-Aguilar, R. Nistal, A. Hernández-Machado, and I. Pagonabarraga, Nat Mater **10**, 367 (2011).

124. H. Gau, S. Herminghaus, P. Lenz, and R. Lipowsky, Science **283**, 46 (1999).

125. B. Zhao, J. S. Moore, and D. J. Beebe, Science **291**, 1023 (2001).

126. J. Judy, D. Maynes, and B. W. Webb, International Journal of Heat and Mass Transfer **45**, 3477 (2002).

127. J. Ou, B. Perot, and J. P. Rothstein, Physics of Fluids **16**, 4635 (2004).

128. D. Di Carlo, Lab on a Chip **9**, 3038 (2009).

129. C. N. Baroud, F. Gallaire, and R. Dangla, Lab on a Chip **10**, 2032 (2010).

130. C.-X. Zhao and A. P. J. Middelberg, Chemical Engineering Science **66**, 1394 (2011).

131. T. S. Fouilland, D. F. Fletcher, and B. S. Haynes, Chemical Engineering Science **65**, 5344 (2010).

132. D. R. Webster and E. K. Longmire, Experiments in Fluids **30**, 47 (2001).

133. M. Sato, S. Kato, and M. Saito, IEEE Transactions on Industry Applications **32**, 138 (1996).

134. T. S. Leu, C. T. Wang, and J. M. Sun, Journal of Mechanics **26**, 259 (2011).

135. S. Lecuyer, W. D. Ristenpart, O. Vincent, and H. A. Stone, Applied Physics Letters **92**, 104105 (2008).

136. S. Torza, R. G. Cox, and S. G. Mason, Philosophical Transactions of the Royal Society of London. Series A, Mathematical and Physical Sciences **269**, 295 (1971).

137. P. Singh and N. Aubry, Electrophoresis **28**, 644 (2007).

138. O. Ozen, N. Aubry, D. T. Papageorgiou, and P. G. Petropoulos, Physical Review Letters **96**, 144501 (2006).

139. W. D. Ristenpart, J. C. Bird, A. Belmonte, F. Dollar, and H. A. Stone, Nature **461**, 377 (2009).

140. J. Wang, B. Wang, and H. Qiu, Scientific Reports **4**, 7123 (2014).

141. S. Dash and S. Mohanty, Electrophoresis **35**, 2656 (2014).

142. P. D. S. Reddy, D. Bandyopadhyay, and A. Sharma, The Journal of Physical Chemistry C **114**, 21020 (2010).

143. S. Holmberg, A. Perebikovsky, L. Kulinsky, and M. Madou, Micromachines **5**, 171 (2014).

144. M. Bhattacharjee, H. B. Nemade, and D. Bandyopadhyay, Biosensors and Bioelectronics **94**, 544 (2017).

145. S. Dutta, N. Mandal, and D. Bandyopadhyay, Biosensors and Bioelectronics **78**, 447 (2016).

146. P. Saenz, A. Wray, Z. Che, O. Matar, P. Valluri, J. Kim, and K. Sefiane, Nature Communications **8**, 14783 (2017).

147. M. K. Tripathi, K. C. Sahu, and R. Govindarajan, Nature Communications **6** (2015).

148. A. K. Singh, K. K. Dey, A. Chattopadhyay, T. K. Mandal, and D. Bandyopadhyay, Nanoscale **6**, 1398 (2014).

149. S. Kumar, A. K. Singh, A. K. Dasmahapatra, T. K. Mandal, and D. Bandyopadhyay, Carbon **89**, 31 (2015).

150. E. Becquerel, Comptes Rendues **9**, 561 (1839).

151. W. Smith, Nature **7**, 303 (20 Feb, 1873).

152. C. E. Fritts, American Journal of Science **26**, 465 (1883).

153. A. Einstein, Annalen der Physik **322**, 132 (1905).

154. R. A. Millikan, Physical Review **4**, 73 (1914).

155. D. M. Chapin, C. S. Fuller, and G. L. Pearson, (US Patents US2780765, 1957).

156. J. D. C. Dickson, (US Patent US2938938, 1960).

157. L. Mei, L.-H. Yeh, and S. Qian, Nano Energy **32**, 374 (2017).

158. F. C. Krebs, H. Spanggard, T. Kjær, M. Biancardo, and J. Alstrup, Materials Science and Engineering: B **138**, 106 (2007).

159. K. Schwarzburg and F. Willig, The Journal of Physical Chemistry B **103**, 5743 (1999).

160. R. R. King, D. C. Law, K. M. Edmondson, C. M. Fetzer, G. S. Kinsey, H. Yoon, R. A. Sherif, and N. H. Karam, Applied Physics Letters **90**, 183516 (2007).

161. M. A. Green, Solar Energy **76**, 3 (2004).

162. R. B. Bergmann, Applied Physics A **69**, 187 (1999).

163. C. M. Lampert, Solar Energy Materials and Solar Cells **76**, 489 (2003).

164. S. Th, M. Pietsch, G. Andra, F. Falk, E. Ose, and S. Christiansen, Nanotechnology **19**, 295203 (2008).

165. A. C. Mayer, S. R. Scully, B. E. Hardin, M. W. Rowell, and M. D. McGehee, Materials Today **10**, 28 (2007).

166. Y.-J. Cheng, S.-H. Yang, and C.-S. Hsu, Chemical Reviews **109**, 5868 (2009).

167. S. K. Hau, H.-L. Yip, N. S. Baek, J. Zou, K. O'Malley, and A. K.-Y. Jen, Applied Physics Letters **92**, 253301 (2008).

168. M. Yamaguchi, Solar Energy Materials and Solar Cells **75**, 261 (2003).

169. N.-G. Park, The Journal of Physical Chemistry Letters **4**, 2423 (2013).

170. B. M. Kayes, H. A. Atwater, and N. S. Lewis, Journal of applied physics **97**, 114302 (2005).

171. B. Tan and Y. Wu, The Journal of Physical Chemistry B **110**, 15932 (2006).

172. A. B. Martinson, J. W. Elam, J. T. Hupp, and M. J. Pellin, Nano letters **7**, 2183 (2007).

173. J. Liu, T. Tanaka, K. Sivula, A. P. Alivisatos, and J. M. Fréchet, Journal of the American Chemical Society **126**, 6550 (2004).

174. A. Heller, Solar energy **29**, 153 (1982).

175. M. Gratzel, Nature **414**, 338 (2001).

176. C. Bakli and S. Chakraborty, Electrophoresis **36**, 675 (2015).

177. R. Dey, U. U. Ghosh, S. Chakraborty, and S. Dasgupta, Langmuir **31**, 11269 (2015).

178. K. Chopra, P. Paulson, and V. Dutta, Progress in Photovoltaics: Research and Applications **12**, 69 (2004).

179. C. Krumm, S. Maduskar, A. D. Paulsen, A. D. Anderson, N. L. Barberio, J. N. Damen, C. A. Beach, S. Kumar, and P. J. Dauenhauer, Energy & Environmental Science **9**, 1645 (2016).

180. D. Wöhrle and D. Meissner, Advanced Materials **3**, 129 (1991).

181. D. Tahir and S. Tougaard, Journal of Physics: Condensed Matter **24**, 175002 (2012).

182. D. S. Murali, S. Kumar, R. Choudhary, A. D. Wadikar, M. K. Jain, and A. Subrahmanyam, AIP Advances **5**, 047143 (2015).

183. I. S. Brandt, C. A. Martins, V. C. Zoldan, A. D. C. Viegas, J. H. Dias da Silva, and A. A. Pasa, Thin Solid Films **562**, 144 (2014).

184. T. Minami, Y. Nishi, T. Miyata, and J.-i. Nomoto, Applied physics express **4**, 062301 (2011).

185. L. Olsen, R. Bohara, and M. Urie, Applied physics letters **34**, 47 (1979).

186. C. Li, F. Wang, and C. Y. Jimmy, Energy & Environmental Science **4**, 100 (2011).

187. J. Li, S. K. Cushing, F. Meng, T. R. Senty, A. D. Bristow, and N. Wu, Nature Photonics **9**, 601 (2015).

188. T. Minami, Y. Nishi, and T. Miyata, Journal of Semiconductors **37**, 014002 (2016).

189. L. Papadimitriou, N. A. Economou, and D. Trivich, Solid-State Electronics **26**, 767 (1983).

190. H. M. Wei, H. B. Gong, L. Chen, M. Zi, and B. Q. Cao, The Journal of Physical Chemistry C **116**, 10510 (2012).

191. S. Noda, H. Shima, and H. Akinaga, in *Journal of Physics: Conference Series* (IOP Publishing, 2013), p. 012027.

192. S. H. Wee, P.-S. Huang, J.-K. Lee, and A. Goyal, **5**, 16272 (2015).

193. T. N. Krupenkin, (US Patent 7898096B1, 2011).

194. T. N. Krupenkin and J. A. Taylor, (US Patent 2012018190A1, 2012).

195. M. Bhattacharjee, V. Pasumarthi, J. Chaudhuri, A. K. Singh, H. Nemade, and D. Bandyopadhyay, Nanoscale **8**, 6118 (2016).

196. M. Bhattacharjee, S. Timung, T. K. Mandal, and D. Bandyopadhyay, (Indian Patent 201631036408A, 2016).

197. J. K. Moon, J. Jeong, D. Lee, and H. K. Pak, Nature communications **4**, 1487 (2013).

198. T. Krupenkin and J. A. Taylor, Nature Communications **2**, 448 (2011).

199. J. A. Paradiso and T. Starner, IEEE Pervasive computing **4**, 18 (2005).

Chapter 2

Prediction of flow patterns using neural network

ABSTRACT

`The work in the present chapter attempts to develop a flow pattern indicator for both gas-liquid and liquid-liquid flow in microchannel with the help of artificial neural network (ANN). Out of many neural networks present in the literature, probabilistic neural network (PNN) was chosen for the present study due to its speed in operation and accuracy in pattern recognition. The inbuilt code in MATLAB^{TM} R2008a was used to develop the PNN model. During the training of PNN, superficial velocity of both phases, channel diameter, angle of inclination, interfacial tension, density difference and viscosity ratio of phases was considered as the governing parameters of the flow pattern. The data was collected from various literature for both gas-liquid and liquid-liquid system through different microchannel with hydraulic diameters (d_h = 0.53 – 0.050 mm for gas-liquid and d_h = 0.793 and 0.250 mm for liquid-liquid system). For the convenience of the study, the flow patterns were classified into six categories namely; bubbly or droplet, plug, slug, annular, churn, liquid ring and liquid lump flow. The prediction for gas-liquid flow pattern showed that a single PNN was incapable to predict the flow pattern for the whole range (d_h = 0.53 – 0.050 mm) of microchannel diameter. That is why two separate PNN models were developed to predict the flow patterns of gas-liquid flow through different channel diameter, one for diameter ranging from 0.53 – 0.22 mm and another for 0.100 – 0.05 mm. The predicted map and their transition boundaries were compared with the corresponding experimental data and were found to be in good agreement. Whereas accuracy in prediction of transition boundary obtained from available analytical models used for conventional channel were less for all diameter of channel as compared to the present work. The percentage accuracy of PNN (~ 94% for d_h = 0.53 mm and ~ 73% for d_h = 0.100 mm) were also found to be higher than the model based on Weber number (~ 86%

for d_h = 0.53 mm and ~ 36% for d_h = 0.05 mm). The prediction for liquid-liquid flow patterns were also performed in a similar fashion. While, the PNN showed high prediction accuracy (~ 91.46 %) but due to lack of enough of data for some flow patterns, it showed few mismatching. The PNN model can be improved with incorporation of more data of varying microchannel diameters.

This chapter is published in Appl. Soft Comput. **13**, 1674 (2013).

2.1 INTRODUCTION

In this chapter we develop a flow pattern indicator capable of predicting all the flow patterns for both gas-liquid and liquid-liquid systems in horizontal microchannel using artificial neural network (ANN). The results are organized in the form of flow pattern maps which are compared with the corresponding literature data. In addition, the predicted flow transitions lines were also compared with various existing analytical models.

2.2 ANN PREDICTION METHODOLOGY

2.2.1 Artificial neural network (ANN)

An artificial neural network (ANN) or neural network is a computational tool which finds a broad range of applications for image processing, clustering of data, forecasting,[1] prediction and identification of flow patterns.[2-7] ANN is employed as an alternative tool for various classical regression models, due to its speed and accuracy in solving highly complex and many non-linear tasks.[8]

The basic theory of an ANN is generally motivated by biological nervous system. It consists of vast interconnection of group of artificial nodes which are quite similar to the large network of neurons in the human brain. There are many types of neural networks such as feed forward back propagation (FFBP), radial basis network (RBN), probabilistic neural network (PNN), support vector machine (SVM) and many more. The operation of each ANN is based on different mathematical theories which has its pros and cons. Some of the qualities that are expected out of a neural network for the present study are accuracy in prediction, swiftness and ease in operation. So, out of many neural networks, PNN has been chosen for the prediction of flow patterns. While, a brief description of PNN has been mentioned in the next sub-section to give a brief overview of this technique.

2.2.2 Probabilistic neural network (PNN)

A probabilistic neural network (PNN) is a feed forward neural network based on the Bayes-Parzen classification theory. It was Specht[9] who first introduced the PNN and presented the basic strategy to break Bayes-Parzen classifier into large number of unit processes which could perform in a multilayer neural network capable of operating each individual process autonomously in parallel. But before proceeding towards PNN, it is really important to have a fundamental understanding of both Bayes' theorem for conditional probability and the strategy to estimate the probability density function (PDF) of any random variables by Parzen's method.

To understand Bayes' strategy for classification, consider a set of samples, $X = [x_1, x_2, ..., x_p]$ obtained from any source, which belongs to a number of different classes $(1, 2, ..., k, ..., K)$. Let the probability that a sample belonging to k^{th} class be 'h_k', and the cost associated for misclassification of that sample is 'c_k'. Now, if it is assumed that the true probability density function of all classes $f_1(x), f_2(x), ..., f_k(x), ..., f_K(x)$ are known, then the Bayes theorem classifies any unknown sample into i^{th} class if

$$h_i c_i f_i(x) > h_j c_j f_j(x) \qquad (2.2.1)$$

where $j \neq i$.

The probability density function, $f_k(x)$ represents the population distribution density of class 'k' samples around an unknown sample. There is a major difficulty with the Bayes' classification strategy, as the probability density $f_k(x)$, in most of the case is not usually known. But in most classification algorithm, the prior knowledge of sample distribution is extremely necessary. In most of the cases, the Gaussian distribution is assumed. If the

assumed distribution and the true distribution samples show large deviation, then it could result in high scale misclassification of samples.[10] In such situation it becomes extremely important to derive a probability density function (PDF) estimator for each class from the set of training data itself. This calls for a multivariate PDF which combines all the features of randomly scattered variables.

Parzen[11] proposed a method to estimate univariate PDF which was later extended to multivariate by Cacoullos.[12] The multivariate PDF estimator, $g(x)$, can be expressed as,

$$g_k(x_1, x_x, ..., x_p) = \frac{1}{n\sigma_1\sigma_2....\sigma_p} \sum_{i=1}^{n} W\left(\frac{x_1 - x_{1,i}}{\sigma_1}, \frac{x_2 - x_{2,i}}{\sigma_2}, ..., \frac{x_p - x_{p,i}}{\sigma_p} \right) \quad (2.2.2)$$

where σ_1, σ_2,….., and σ_p are the smoothing parameters (also called bandwidth or kernel width) representing standard deviation around the mean of 'p' random variables $x_1, x_2, ..., x_p$, W is the activation function and 'n' is the total number of training data in the sample. Now, on assuming that all the smoothing parameters are equal (i.e. $\sigma_1 = \sigma_2 = \sigma_3 = ... = \sigma_p = \sigma$), and using a bell-shaped Guassian function for W, Eq. (2.2.2) is reduced to,

$$g_k(x) = \frac{1}{(2\pi)^{\frac{p}{2}} n\sigma^p} \sum_{i=1}^{n} \exp\left(-\frac{\|x - x_i\|^2}{2\sigma^2} \right) \quad (2.2.3)$$

where 'x' is the vector of scattered variables and 'x_i' is the i^{th} training vector. Here Eq. (2.2.3) represents the average of the multivariate distributions where each distribution is centered at one distinct training sample.

The schematic representation of the basic architecture of PNN is shown in Figure 2.1. The figure shows that a PNN is composed of four layers namely input layer (containing input

nodes), hidden layer (containing hidden nodes), pattern layer (containing class nodes) and output layer (with a decision node). The input nodes does not perform any computational operation and thus simply pass out the inputs of random variables 'x' to each neuron in hidden layer. The hidden layer consists of neurons equal to the total number of training variables. The hidden layer on receiving the input from input layer calculates the Euclidean distance between each random variable and the training set of data that constitute the hidden layer which is then passed through an activation function ϕ_i,

$$\phi_i(x) = \exp\left(-\frac{\|x - x_i\|}{2\sigma^2}\right) \tag{2.2.4}$$

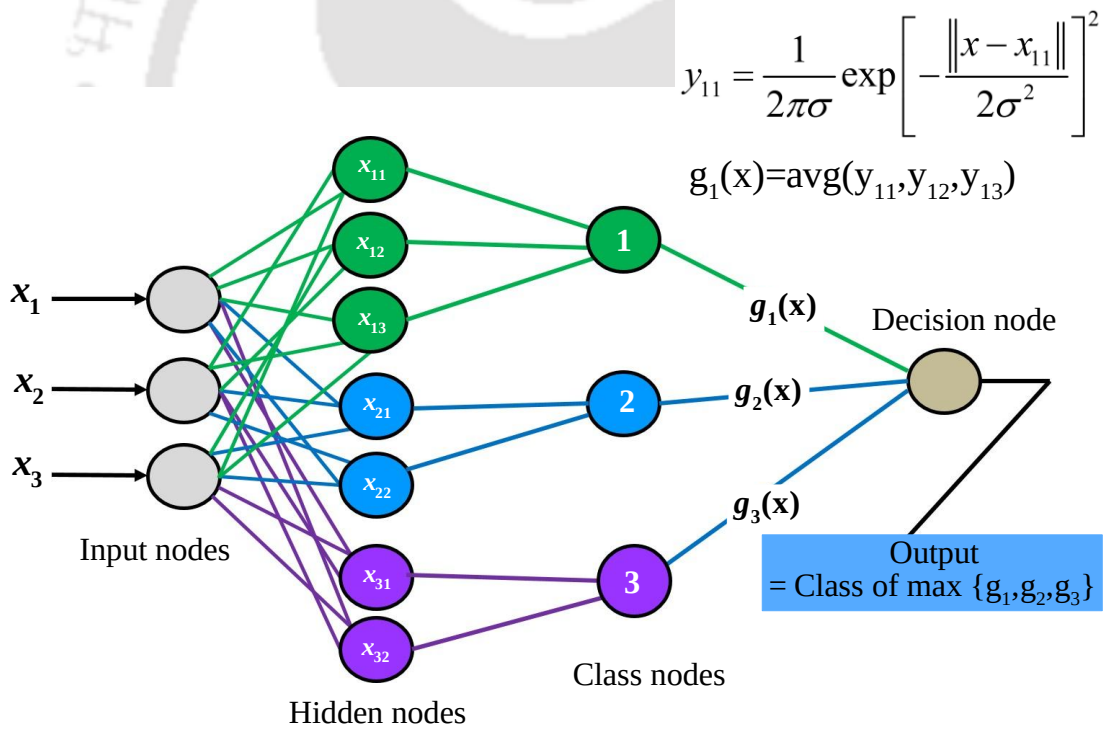

Figure 2.1: Schematics of PNN architecture.

The class layer then computes the summation and gives out the arithmetic mean of the output of the hidden layer for each class, 'C_k' using Eq. (2.2.3). Assuming the prior probability for each class and the cost associated for each misclassification to be equal, the

output layer classifies any random variable 'x' by comparing the output of class layer for each class and then following the Bayes' classification theorem as,

$$C_k(x) = \arg\max\left\{g_k(x)\right\} \tag{2.2.5}$$

In order to implement the PNN model for prediction of flow patterns, it is required to collect data from the past literature. This is because PNN requires huge amount of data for training as well as test. The final performance of a PNN is totally dependent on how well the PNN was trained. So, the first step prior to the PNN prediction is the collection of data from literature and classification of flow patterns into various groups. Then subsequent steps of PNN are training, testing, prediction and development of a flow pattern map. For this reason, the PNN was trained using the data collected from literature with the incorporation of significant parameters, namely, superficial velocity of dispersed (U_d) and continuous phase (U_c), channel hydraulic diameter (d_h), density difference of dispersed phase and continuous phase ($\Delta\rho$), viscosity ratio of dispersed and continuous phase (μ_d / μ_c) and surface tension (γ).

2.2.3 Collection of data

The experimental flow pattern data for gas-liquid[13,14] and liquid-liquid[15,16] flow in microchannel were collected from various literatures. These literatures were selected for extraction of data because their works altogether covers various ranges of microchannel diameters from ~500 – 50 μm. After the collection of data, it became very clear that the flow pattern terminology in microchannel used by each author for a particular interfacial configuration is quite different from each other which created a lot of confusion. So, for convenience in the present study, it was decided to classify all the flow patterns and grouped them into a few categories in accordance to its morphology.

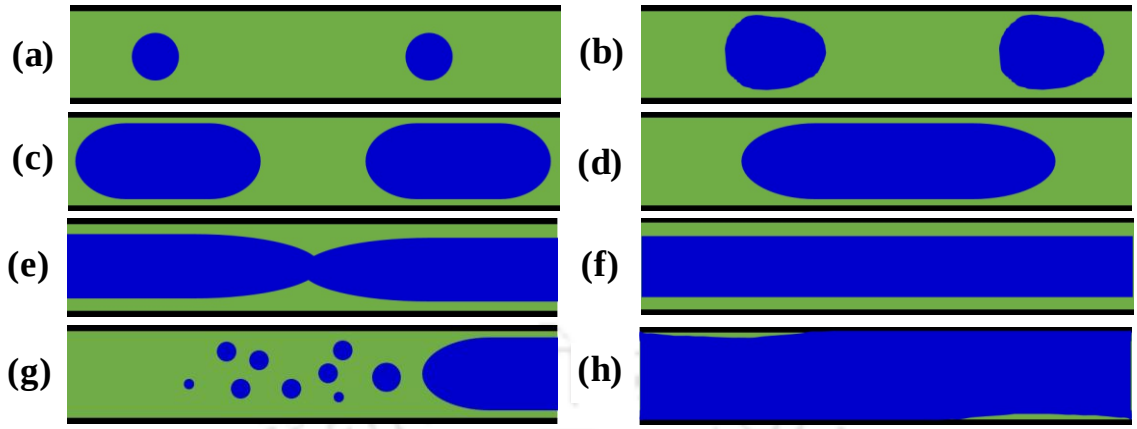

Figure 2.2: Representative diagrams of flow patterns in circular microchannel: (a) bubbly/droplet; (b) plug; (c), (d) slug; (e) liquid-ring; (f) annular; (g) churn; (h) liquid lump flow.

2.2.4 Classification of flow patterns in microchannel

Generally, any two-phase flow consists of a dispersed phase which is surrounded by the continuous phase. Almost all the authors have pointed out the issue of inconsistency in the terminology of flow patterns that needs to be addressed.[17,18] For example, Chung and Kawaji[13] observed slug-annular flow in 0.53 and 0.25 μm microchannels, which is very much similar to the throat-annular flow observed by Saisorn and Wongwises.[14] Similarly, the annular-rivulet flow reported by Saisorn and Wongwises[14] and liquid lump flow reported by Serizawa et al.[19] could be placed in the same group of flow regime. Thus, it is very important to properly classify these flow patterns, in accordance to its characteristic properties and place them in their respective flow regime. So, with careful observations and understanding, all the flow patterns observed were divided into seven categories, which would be able to cover all the flow patterns observed in the range of microchannel. These seven flow patterns are as follows:

i. Bubbly or droplet flow: This type of flow is characterized by the occurrence of spherical or spheroid shape distribution of dispersed phase with size smaller than

the channel diameter, in a continuous phase which is shown in Figure 2.2(a). Here, the blue and green color represents dispersed and continuous phases, respectively.

ii. Plug flow: This type of flow generally occurs in the form of a bullet shape bubble or droplet with pointy frontal side and flat interface along its trailing end with size mostly equal or slightly larger than channel diameter. A typical schematic diagram of a plug flow is shown in Figure 2.2(b).

iii. Slug flow: Slug flows (Taylor bubble or elongated bubble) are generally characterized by the occurrence of elongated shape bubble or Taylor bubbles of size larger (~5d_h) than that of channel diameter,[15] as shown in Figure 2.2(b, c). A thin film of continuous phase may occur in between the slug and channel wall. A liquid bridge is often observed separating two consecutive slugs of dispersed phase. The basic nature of elongated bubble and slug-ring flow described in literature is quite similar and has been grouped as a slug flow.

iv. Liquid ring flow: This is an intermediate flow morphology which occur in between the transition of slug to annular flow following a steady[15,20] or unsteady[13,21] flow in nature. This flow morphology occurs when the length of slugs increases with increase in the flow velocity of dispersed phase at constant velocity of continuous phase, as a result of which the two consecutive slugs touch each other and the interfacial barrier between them is broken. This leads to the merging of neighboring slugs into a single entity with the formation of many ring shape ripples,[22,23] as shown in Figure 2.2(d). The mechanism of formation is quite similar to the formation of slug-annular flow reported by Triplett et al.[20] and throat-annular flow reported by Saisorn and Wongwises.[14,24] The similarity between these flow

patterns were mention by Shao et al.[17] in a review paper. So, for sake of simplicity, slug-annular, throat-annular and ring-slug was placed under the liquid ring flow category in the present study.

v. Annular flow: This flow morphology is characterized by the presence of a dispersed phase in the core and continuous phase in the annulus region which is shown in Figure 2.2. It is usually observed when the velocity of the dispersed phase is increased beyond the range where liquid ring flow occurs. With increase in velocity of dispersed phase the ripples or undulations are stabilized into smooth interface and the ring shape interface disappears. The semi-annular flow of Chung and Kawaji[13] was found to be of similar characteristics and so it was placed under the annular flow.

vi. Liquid lump flow: This type of flow is observed in microchannel at high gas flow rate and lower range of pipe diameter. It is generally identified as a high-speed moving gas core with lumps of liquid sliding on the wall,[19] as shown in Figure 2.2(h). Here the high surface tension force restricts the liquid from spreading at the wall to form a thin liquid film. This flow resembles a meandering flow which is very much similar to annular-rivulet flow observed by Saisorn and Wongwises.[14] So, liquid lump and annular-rivulet flow has been placed together as liquid lump flow.

vii. Churn: This type of flow morphology occurs at relatively high velocity of continuous flow where disruption of smaller size bubbles take place along the tail side of a long slug flow,[13,14] as shown in Figure 2.2(g). Alongside, it can also occur due to the random swirling waves which disturbs the wavy-annular flow leading to

formation of smaller bubbles or droplets.[20] Multiple flow[13,21] identified based on the probability of appearance of smooth, ring shaped, serpentine gas core has also been placed under churn flow regime.

Table 2.1: Numerical value and symbol assigned for different flow patterns.

Flow patterns	Numerical value	Representative symbols
Bubbly/droplet flow	1	●
Slug flow	2	▲
Liquid ring flow	3	●
Liquid lump flow	4	◀
Annular flow	5	■
Churn flow	6	♦
Plug	7	▼

The training, testing and prediction is discussed in results and discussion section. During the training of the PNN, the flow patterns are represented by numeral values and together with different symbols in the flow pattern map. The numerical value and symbols of the corresponding flow patterns are shown in Table 2.1.

2.3 RESULTS AND DISCUSSION

The training of PNN was performed using the inbuilt code of Matlab R2008a. In the beginning, an attempt was made to develop a single network which could predict the flow pattern for gas-liquid flow system with diameter ranging, 0.53 mm $\geq d_h \leq$ 0.050 mm. But the predicted results obtained from developed PNN were found to be of poor accuracy. One of the reasons behind such misclassification could be due to the dissimilar trend in

flow patterns observed in microchannel with diameter, $d_h \leq 0.200$ mm and $d_h \geq 0.200$ mm, which can be attributed to the simultaneous occurrence of more than one flow patterns at a given set of phase velocities.[13,21] It was predicted that the effect of surface force is more dominant in microchannel with diameter, $d_h \geq 0.200$ mm whereas both surface and viscous force together are dominant in $d_h \leq 0.200$ mm, opposing the gravity and inertial force. Considering this factor, the whole diameter range were divided in two regions, one is surface force dominated region with diameter ranging, 0.22 mm $\leq d_h \leq$ 0.53 mm and combined surface and viscous force dominated region with diameter, $d_h \leq 0.200$ mm. So, based on these two regions, two PNN models were developed for the flow pattern prediction.

2.3.1 Prediction of flow pattern in surface force dominated region

The data collected for nitrogen-water flow (d_h = 0.53 mm) and air-water flow (d_h = 0.53 and 0.22 mm) was used for training and testing of the network. About 874 data out of 1096 data (79.74%) was used for training and the remaining 222 data (20.26%) were used for test. During the training of PNN, the selection of an optimum value of spread constant or smoothing parameter (σ) is very important as the shape of Gaussian function is totally influenced by this constant value. An ideal spread constant for a PNN is the one, which gives the minimum prediction error during training and test of the network. Various algorithm and techniques has been reported, to estimate the optimum spread constant such as genetic algorithm[25] trial and error method.[7,10] In the present study, the selection of 'σ' was carried out using the trial and error method as it involves simple operation processes. So, number of PNN test has been conducted on a set of flow pattern data with different values of spread constant.

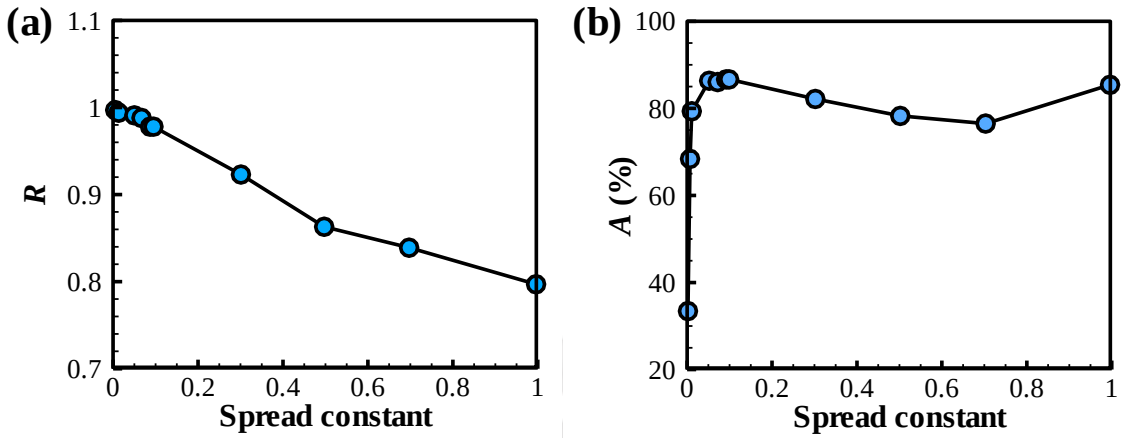

Figure 2.3: Selection of spread constant and regression constant for microchannels diameter ranging from 0.53 – 0.22 mm where, (a) shows the variation of value of regression constant with spread constant and (b) shows the variation percentage (%) of accuracy in prediction with spread constant.

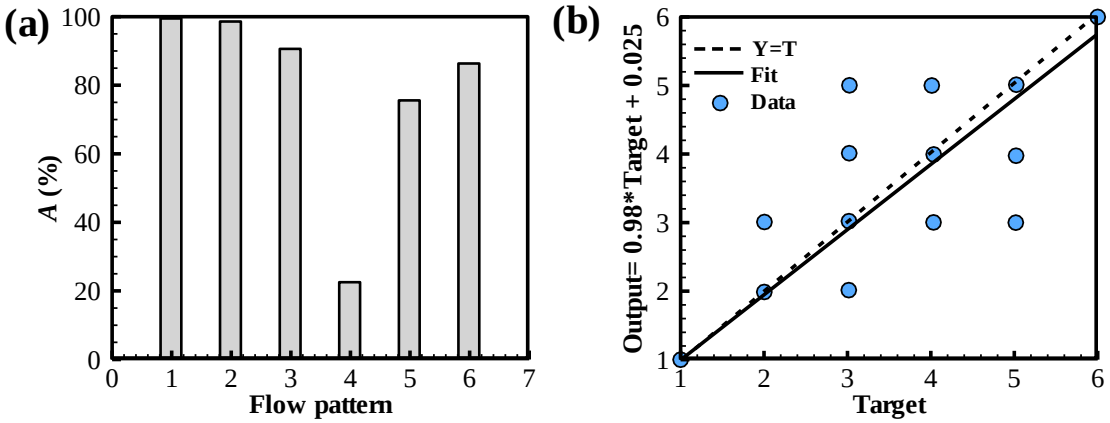

Figure 2.4: Training and test results of PNN for microchannels with diameter ranging from 0.53 mm to 0.22 mm at selected spread constant: (a) percentage accuracy in prediction accuracy and (b) graphical representation of correlation of various targets.

The value of 'σ' which produces the minimum misclassification along with good training (if $0.9 \leq R \leq 1$) is usually chosen as the optimum spread constant. The plot for regression constant (R) and percentage accuracy (A) in prediction at different values of spread constant is shown in Figure 2.3. A spread constant, $\sigma = 0.1$, was selected as optimum as it gives maximum prediction accuracy. So, using $\sigma = 0.1$, various available flow pattern

maps for air-water and nitrogen- water flow are predicted using the PNN developed and compared with its corresponding experimental data from literature.

As it can be seen from Figure 2.4(a) and 2.4(b), that the percentage accuracy for prediction of flow patterns has been good and regression constant, R = 0.98162 shows good training. Different correlation for different flow pattern is obtained with this spread constant and regression constant from the trained network shown in Figure 2.4(b). The X-axis represents the target as fed in data for training and the Y-axis represents the prediction of the training data itself after training. The thick and the dotted lines represent the fit of the plot and $Y = X$ fit line. The dot points on the line represent correct prediction and dot points outside the line represents the mismatching. It should be noted that each dot points in the graph contains more than one points overlapping one upon another. Here, in the plot of Figure 2.4(b), a total of 874 data are present. The graph in Figure 2.4(a) shows the percentage accuracy of PNN in predicting (at σ = 0.1) the seven flow patterns represented by its numeral values assign. As can be seen from the same figure, the predicted results for all the flow patterns is good, except for liquid lump flow (pattern 4). This is because of the availability of less number of data of liquid lump flow for training the PNN. But as the prediction accuracy of other flow patterns is quite good, the PNN can be used for prediction of flow patterns of unknown data.

Predicted flow pattern map of nitrogen-water flow in 0.53 mm channel was shown in Figure 2.5(a). Experimental data for the same system were collected from literature[13] and is shown in Figure 2.5(b) in the form of flow pattern map for comparison. The Y-axis of both the maps represents the flow velocity of liquid phase and X-axis represents the flow velocity of gas phase. Each symbol represents a particular flow pattern as mentioned in

figure caption and in Table 2.1. Solid lines in the predicted and experimental map indicate the experimental transition boundary of the corresponding flow pattern drawn by respective investigators.

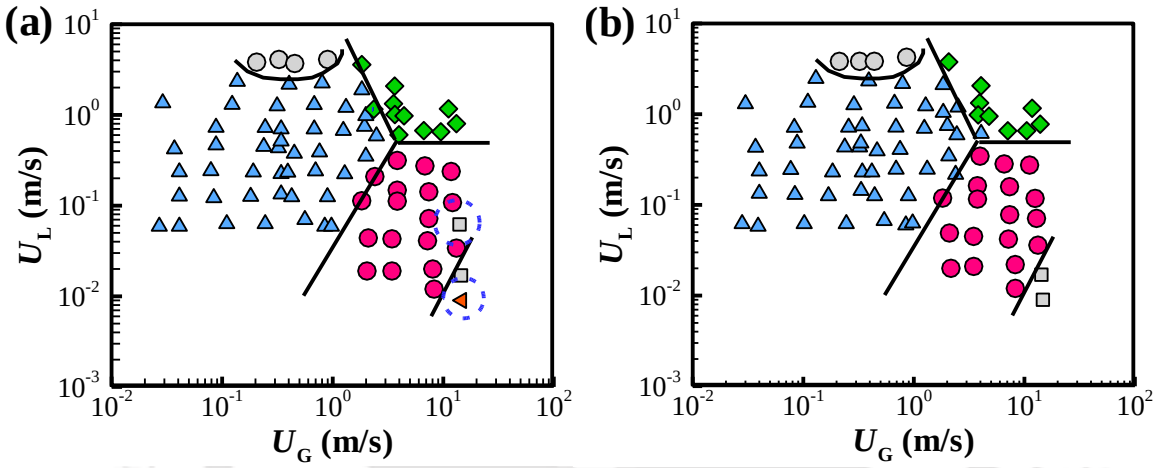

Figure 2.5: Comparison of (a) predicted map with the (b) experimental data for nitrogen–water flow in microchannel with diameter, d_h = 0.53 mm using the notation ((●) bubbly/droplet flow, (▲) slug flow, (●) liquid ring flow, (◀) liquid lump flow, (■) annular flow, (♦) churn flow, (▼) plug flow and transition lines (—) from literature.[14]

Here, the plot in Figure 2.5(a) indicates the good prediction with few mismatching which could be easily pointed out when compared with that of its corresponding experimental results (Figure 2.5(b)). The mismatching in predictions are marked with dashed circle in Figure 2.5(a). The percentage (%) accuracy (*A*) in prediction of different flow pattern is shown in Figure 2.6. In this figure, the % accuracy in PNN prediction of various flow patterns is plotted against the microchannel diameters. Figure 2.6 indicates that the % accuracy varies for different flow patterns with tube diameter. A general trend of fall in accuracy with increase in hydraulic diameter is observed which may be due to the less number of training data available for flow patterns occurring at higher hydraulic diameter.

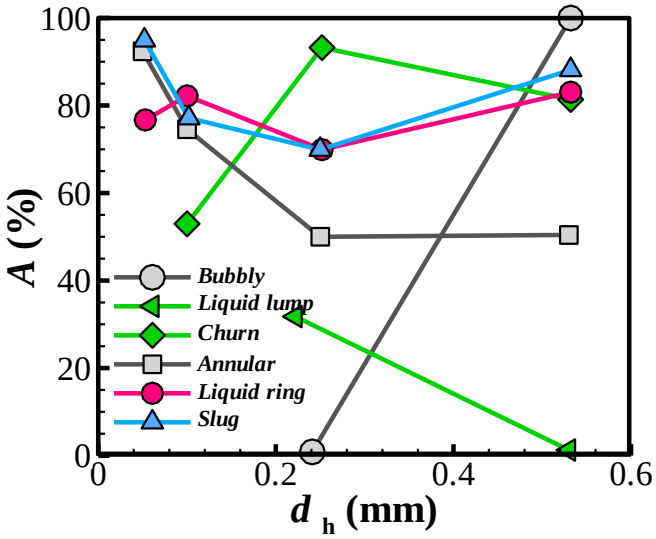

Figure 2.6: Accuracy, *A* (%) in PNN prediction of different flow pattern at various microchannel diameters, d_h.

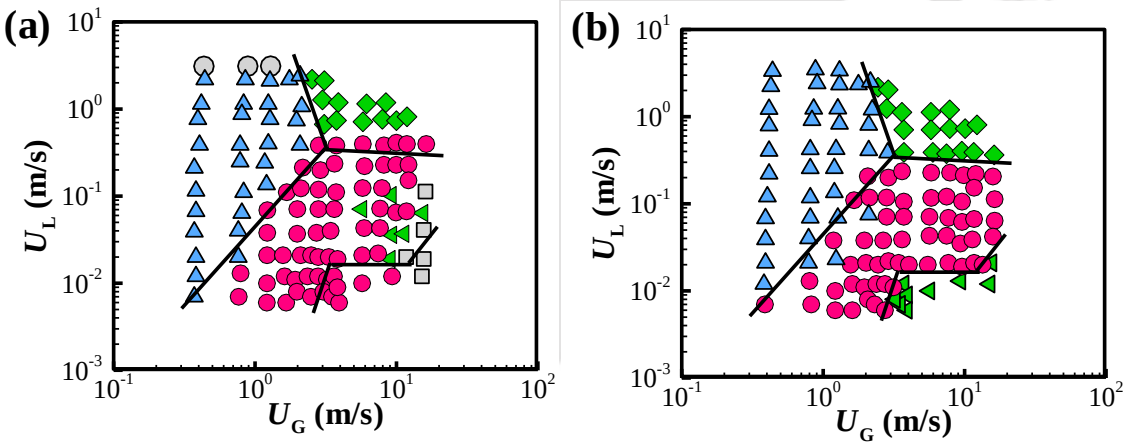

Figure 2.7: Comparison of (a) PNN predicted map with the (b) experimental flow pattern map for air-water flow in microchannel with diameter, d_h = 0.53 mm using different notations ((●) bubbly/droplet flow, (▲) slug flow, (●) liquid ring flow, (◀) liquid lump flow, (■) annular flow, (♦) churn flow, (▼) plug flow and transition lines (—) from literature.[14]

Similarly flow pattern map was predicted for air-water flow as shown in Figure 2.7(a), through microchannel with diameter of 0.53 mm. The predicted map can be compared with experimental map (Figure 2.7(b)) as done for nitrogen-water system. Here also overall prediction is good except for liquid-lump flow. This discrepancy arises due to two things; - (i) because of less number of data available during training and (ii) the region for liquid lump flow and annular flow lies quite very close to each other, Most of the mismatching occurred along the transition zones, where it is difficult to identify a distinct flow pattern at such flow condition due to its unstable nature.

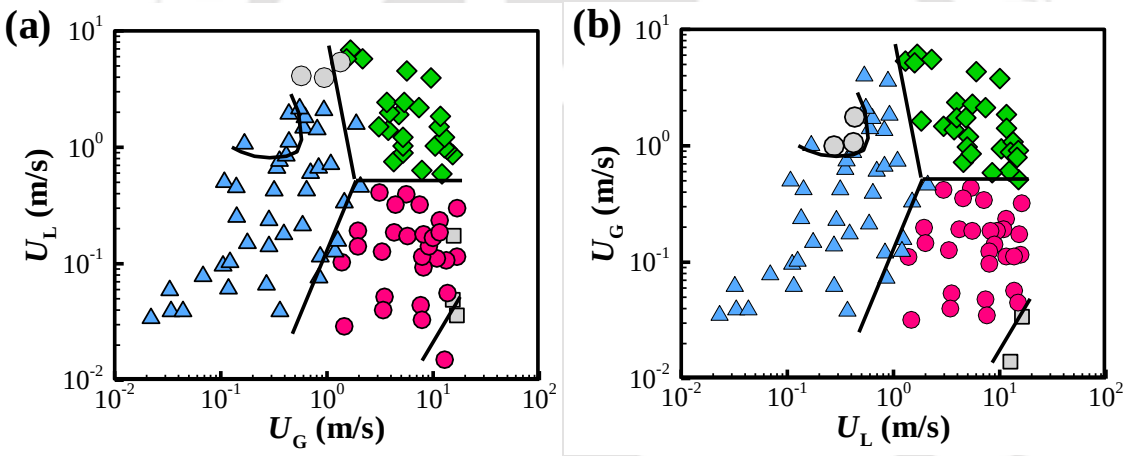

Figure 2.8: Comparison of (a) PNN predicted flow pattern map with the (b) experimental flow pattern map for nitrogen-water flow in microchannel with diameter, d_h = 0.25 mm using different symbols: ((●) bubbly/droplet flow, (▲) slug flow, (●) liquid ring flow, (◀) liquid lump flow, (■) annular flow, (♦) churn flow, (▼) plug flow and transition lines (—) from literature.[13]

A comparison between predicted and experimental results were made for nitrogen water flow in 0.25 mm and air-water flow in 0.22 mm diameter channel. The result for 0.25 mm pipe is shown in Figure 2.8 and that for 0.22 mm in Figure 2.9. Significance of the axis and legends represents same meaning as discussed for 0.53 mm channel. Here, Figure

2.8(a) clearly shows that PNN is unable to predict bubbly flow region in 0.25 mm microchannel. Probably this is due to lack of sufficient literature data for this region. For the other flow pattern the deviation is quite low and it is comparable with the results of 0.53 mm microchannel. Figure 2.9(a) shows the larger deviation in liquid lump flow. Due to this, the overall prediction accuracy reduces in this case. Microchannel of diameter 0.22 mm lies near the transition zone of surface force dominated region and combined surface and viscous force dominated region. The flow patterns beyond this range of microchannel diameter exhibits dissimilar characteristics in nature, where more than one type of flow patterns can be observed for a single flow parameter.

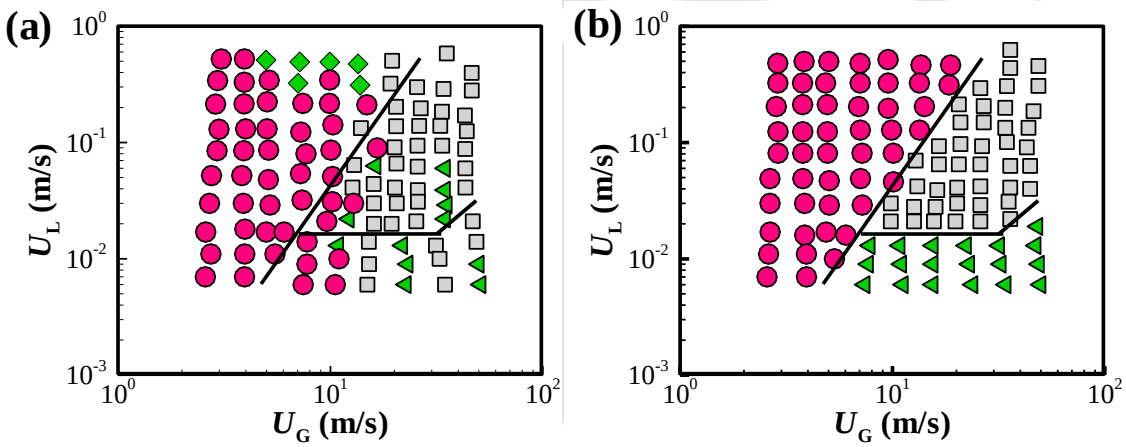

Figure 2.9: Comparison of (a) PNN predicted map with the (b) experimental data for air-water flow in microchannel with diameter, d_h = 0.22 mm using different symbols ((●) bubbly/droplet flow, (▲) slug flow, (●) liquid ring flow, (◀) liquid lump flow, (■) annular flow, (♦) churn flow, (▼) plug flow and transition lines (—) from literature.[14]

The PNN developed was also used to predict map for nitrogen-water flow through 100 and 50 μm microchannels.[13] But large number of mismatching in classification were found when compared with the experimental results because the flow patterns observed in this region are different as compared to the higher diameter as mentioned above. At the same

time the flow patterns were identified in this region based on the probability of appearance of a particular flow pattern as discussed in introduction. These two points motivates in developing another PNN in order to predict flow patterns in microchannels with diameter, $d_h \leq 200$ μm.

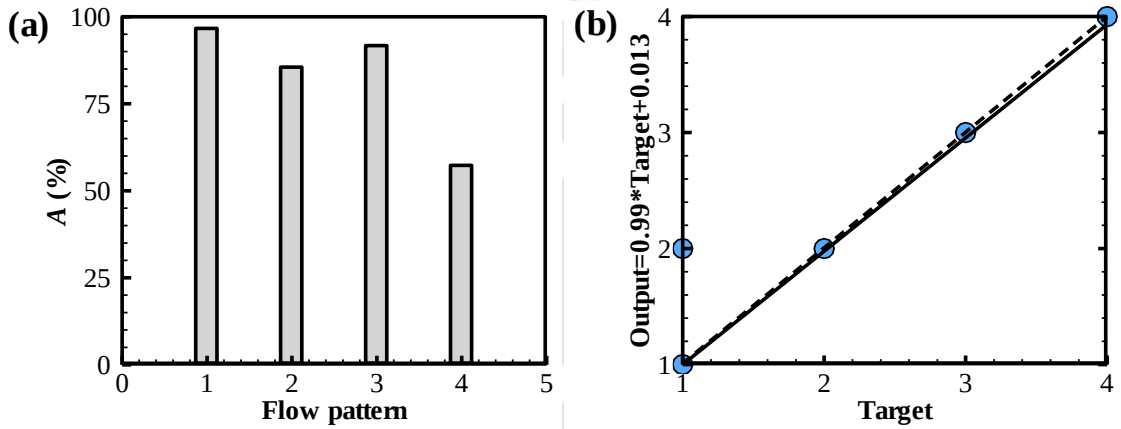

Figure 2.10: Training and test results of PNN for flow patterns in microchannels with diameter, $d_h < 200$ μm where plots (a) and (b) shows the percentage accuracy in prediction and graphical representation of correlation of various targets, respectively.

2.3.2 Prediction of flow pattern in surface and viscous force dominated region

The development of network for prediction of flow patterns in $d_h < 200$ μm were carried out using data obtained from Chung and Kawaji[13] map for 100 and 50 μm. In this region four flow patterns namely; slug, liquid ring, annular and churn flow were reported in literature. A total of 783 data could be collected. Out of which 623 data (79.57%) data were used for training and the rest 160 data (20.43%) were used for test. The training and test of the network for microchannel were carried out in the same way as described in Section 2.3.1. In similar fashion spread constant, σ = 0.1 was selected for training where regression constant of 0.98846 shows good training. The corresponding curves are not mentioned here to avoid the repetition.

Accuracy in test and correlation for the flow patterns obtained using these two values are shown in Figure 2.10. The plot indicates that maximum accuracy (96.55%) decreases whereas minimum accuracy (57.14%) increases as compared to the higher diameter of microchannel. Using this PNN flow pattern map of nitrogen-water flow through 0.100 mm microchannel were predicted as shown in Figure 2.11(a). While, the plot in Figure 2.11(b) is the experimental map for the same and is shown for comparative study. These two figures show higher mismatching in prediction of liquid ring flow and churn flow as compared to the other flow patterns.

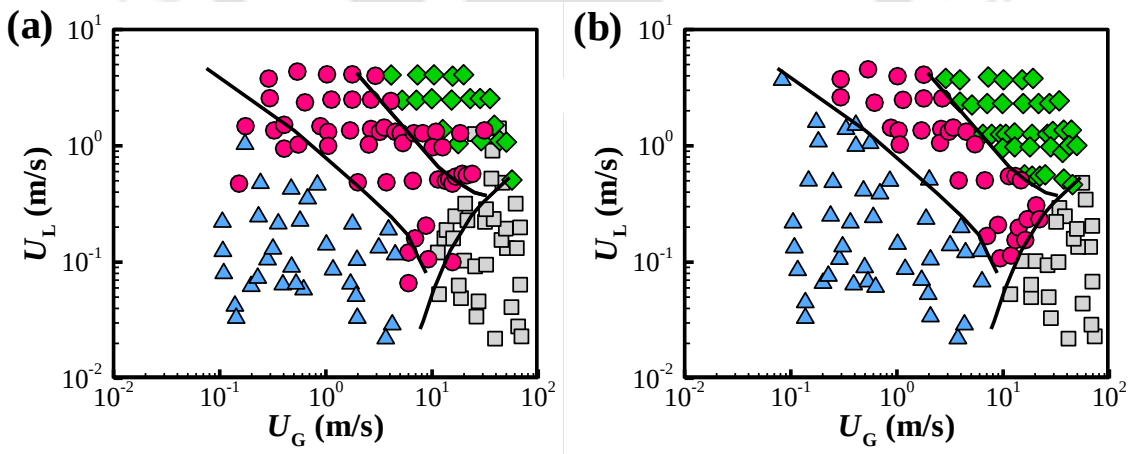

Figure 2.11: Comparison of (a) PNN predicted flow pattern map with the (b) experimental flow pattern map for nitrogen-water flow in microchannel with diameter, d_h = 0.100 mm using different symbols: ((●) bubbly/droplet flow, (▲) slug flow, (●) liquid ring flow, (◀) liquid lump flow, (■) annular flow, (♦) churn flow, (▼) plug flow and transition lines (—) from literature.[13]

Similar comparison is shown in Figure 2.12 for nitrogen-water flow through 0.050 mm microchannel. Only three flow patterns called slug, liquid ring and annular flow, are reported in literature for this microchannel. While, the PNN showed high accuracy in prediction for all the cases except few points in the liquid ring flow region. The accuracy

in prediction of liquid ring flow and accuracy of liquid lump flow is shown in Figure 2.6. PNN prediction of flow patterns map also shows various transition zones from which transition boundaries or lines can be drawn on a flow pattern map. These predicted transition boundaries are compared with the transition boundaries obtained from various analytical models available in literature to show the efficiency of probabilistic neural network (PNN) in pattern recognition.

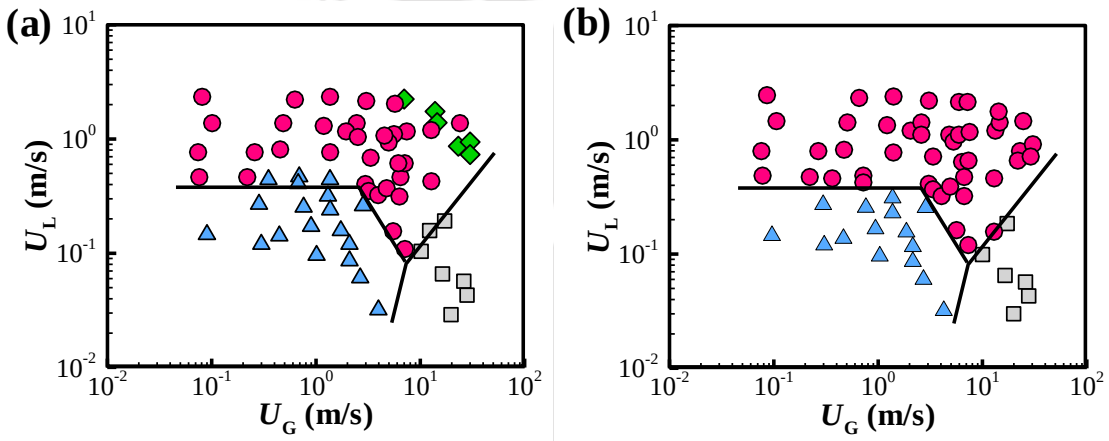

Figure 2.12: Comparison of (a) PNN predicted flow pattern map with the (b) experimental flow pattern map for nitrogen-water flow in microchannel with diameter, d_h = 0.050 mm using different notations: ((●) bubbly/droplet flow, (▲) slug flow, (●) liquid ring flow, (◀) liquid lump flow, (■) annular flow, (♦) churn flow, (▼) plug flow and transition lines (—) from literature.[13]

2.3.3 Comparison with analytical models

Four analytical models were employed for prediction of four transition boundaries namely; (i) bubbly to slug, (ii) slug to liquid ring, (iii) liquid ring to annular and (iv) slug to churn flow. Bubbly to slug transition region can be predicted using Eq. (2.3.1) which was proposed by Brauner[26] and later extended by Brodkey[27].

$$\Delta U = U_L - U_G \geq 4.36\left[\frac{\gamma\left(\rho_L-\rho_G\right)\cos\beta'}{\rho_L^2}\right]^{1/4}\left\{1+1.443\left(N_{vg}\cos\beta'\right)^{0.4}\right\}^{1/2} \qquad (2.3.1)$$

where, N_{vg} is the gas viscosity number defined as,

$$N_{vg} = \frac{\mu_G^4 (\rho_L - \rho_G) g}{\rho_G^2 \gamma^3} \tag{2.3.2}$$

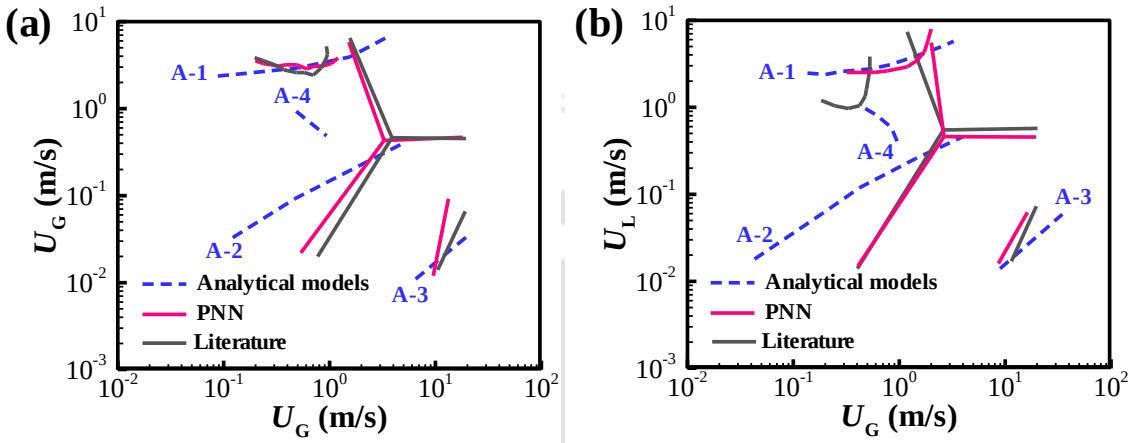

Figure 2.13: Comparison of PNN predicted transition lines for flow patterns with d_h = 0.53 and 0.25 mm for nitrogen-water system with that of experimental and theoretical transition lines.

According to this model, the entrainment of bubbles will take place when the velocity difference (ΔU) between gas and liquid phase exceeds a threshold value as given in the R.H.S. of Eq. (2.3.1). It was found that the constant coefficient 4.36 in Eq. (2.3.1) can be tune to obtain a close match with experimental transition lines. A value of 12.5 as the constant in Eq. (2.3.1) does show good agreement for the slug to bubbly transition as shown by line A-1 in Figure 2.13 and 2.14, respectively. Here, PNN prediction of the same transition boundaries (—) are superimposed on the same figure for comparison. Figures 2.13 and 2.14 represent the transition boundary for nitrogen-water and air-water system, respectively. This prediction is also in good agreement with the experimental transition boundary.

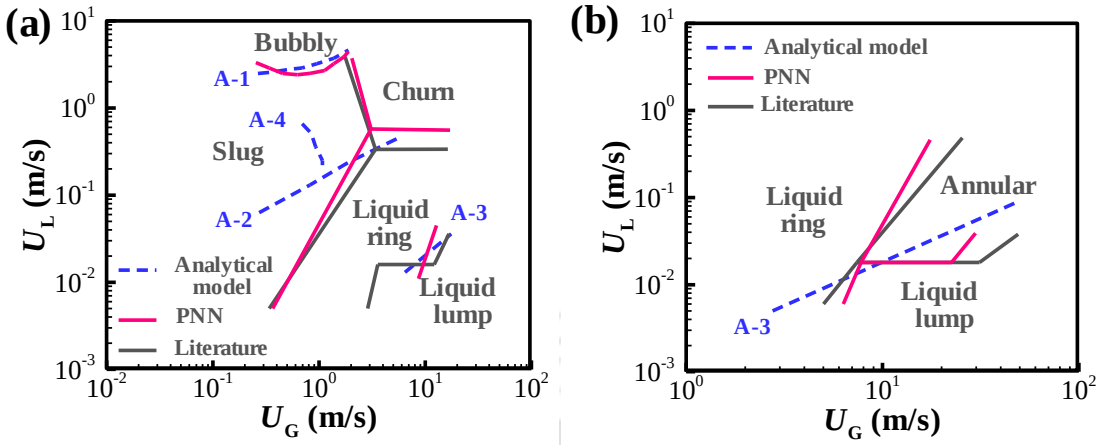

Figure 2.14: Comparison of PNN predicted transition lines for flow patterns in microchannel with d_h = 0.53 and 0.22 mm for air-water system with that of experimental and theoretical transition lines.

The transition boundary for slug to liquid ring and liquid ring to annular was obtained from annular flow model developed based on two-fluid model.[28] The criteria for avoiding the transition of an annular flow to slug flow was combined with the annular flow model[29] to get the transition boundaries. The expression for the transition boundary for slug to liquid ring is given by,

$$\frac{U_{GS}}{U_{LS}} \geq 2.875\times10^{-3}\,\frac{\mu_L}{\mu_G}\,\mathrm{Re}_{LS}^{0.8}+1.15 \qquad \text{laminar core- turbulent annulus} \qquad (2.3.3)$$

whereas the transition from liquid ring to annular can be represented as,

$$\frac{U_{GS}}{U_{LS}} \equiv \frac{U_{CS}}{U_{AS}} \geq \frac{\mu_L}{\mu_G}+2 \qquad \text{laminar core- laminar annulus} \qquad (2.3.4)$$

where U_{CS} and U_{AS} represents the superficial velocity of the core and annular respectively and Re_{LS} is the superficial Reynolds number of liquid phase. In Figure 2.13 and 2.14(a), the transition boundary for slug to liquid ring and liquid ring to annular are shown by line A-2 and line A-3. It can be seen that both the transition lines (A-2 and A-3) contains large deviation from that of experimental curves which needs to be modified. But the PNN

predicted transition line (—) showed good agreement with the experimental one. While Slug to churn flow is absent in 0.22 mm pipe, so this transition line is not shown in Figure 2.14(b).

The mechanism and criteria for transition of slug to churn has been discussed in literatures such as Hewitt and Jayanti[30] and Brauner and Barnea[31]. It describes that if the gas holdup (α_s) in the liquid slug is greater than 0.52, then slug flow will be converted into churn. This gas hold up can be predicted using the model proposed by Barnea and Brauner[32] which is given in the form of the following expression as,

$$\alpha_S = 0.058\left[d_c\left(\frac{2 f_M}{D} U_M^3\right)^{2/5}\left(\frac{\rho_L}{\gamma}\right)^{3/5} - 0.725\right]^2 \qquad (2.3.5)$$

where U_M (=U_{GS} + U_{LS}) is the mixture velocity, f_M the friction factor based on mixture velocity, d is the diameter of channel, ρ_L is the density of liquid phase and γ is the surface tension of the gas-liquid interface. Here, d_C is taken as the minimum value between d_{CD} and d_{CB} as mentioned by Barnea.[33]

$$d_{CD} = 2\left[\frac{0.4\gamma}{(\rho_L - \rho_G) g}\right]^{1/2} \qquad (2.3.6)$$

$$d_{CB} = \frac{3}{8}\left[\frac{\rho_L}{(\rho_L - \rho_G)}\right]\frac{f_M U_M^2}{g\cos\beta} \qquad (2.3.7)$$

where, d_{CD} is the critical bubble size above which the bubble will get deformed and d_{CB} is the critical bubble size below which migration of bubbles to the upper part of the channel is prevented.

The friction factor as in Jayanti and Hewitt[34] is as,

$$f_M = \frac{16}{\mathrm{Re}_M} \qquad \text{if } Re \le 2100, \qquad (2.3.8)$$

$$f_M = 0.046\,\mathrm{Re}_M^{-0.2} \qquad \text{if } Re > 2100, \tag{2.3.9}$$

$$\text{where, } \mathrm{Re}_M = \frac{\rho_L U_M D}{\mu_L} \tag{2.3.10}$$

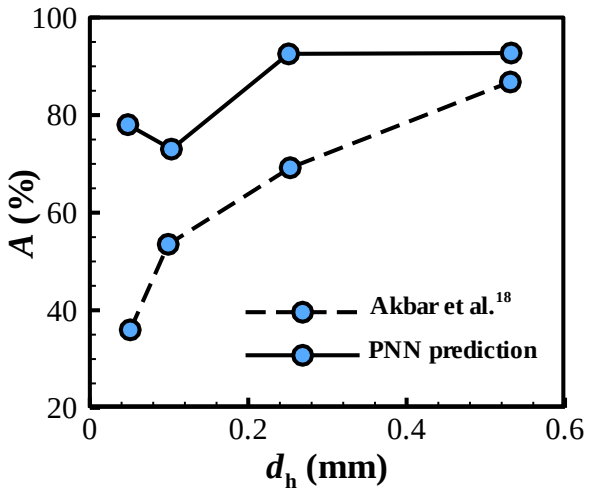

Figure 2.15: Comparison of predicted results obtained from ANN and Weber number model.[18]

Finally, the locus for α_s = 0.52 was obtained from Eq. (2.3.5) and the locus gives the transition boundary for slug to churn flow. This was shown by line A-4 in Figure 2.13 and 2.14(a). It shows a large deviation from the experimental one. It seems that slug to churn transition in small diameter channel occurs at much higher gas superficial and liquid superficial velocities and the mechanism are quite different from that of conventional channel to microchannel. So the nature of transition boundary located using Eq. (2.3.5) showed wide disagreement. The figures show that the transition boundary predicted by PNN is very much closer to the experimental boundary. It should be noted that slug to churn flow is absent in case of flow through 0.22 mm pipe and so, this transition is not shown in Figure 2.14.

2.3.4 Comparison with Weber number model

Akbar et al.[18] proposed a flow pattern map for microchannel with diameter, d_h < 1 mm based on the Weber number. The flow patterns in the whole range of microchannel diameter can be predicted using this model. In the present study it was also used to predict the flow pattern for nitrogen-water system. The percentage (%) accuracy of this model for different microchannel diameters (0.53, 0.25, 0.100, and 0.050 mm) are shown in Figure 2.15. A comparison between this model and PNN is also been shown in the same figure. The solid line represents the average accuracy of PNN and the dashed line shows the same obtained from Weber number model. In this figure, X-axis represents the internal tube diameter and Y- axis shows the % accuracy in prediction of the models. The overall ANN prediction accuracy for nitrogen-water flow was found to be higher than that of the Akbar et al.[18] which is shown in Figure 2.15. From this figure it is clear that percentage (%) accuracy of this PNN is greater than 90% in the range of pipe diameter from 0.53 mm to 0.25 mm. But it reduces below this pipe diameter.

Weber number based model was found to be less accurate with decrease in channel diameter below 200 μm which was also been found in literature.[35] This clearly shows that, apart from inertial and interfacial forces, there are other forces which influences the flow pattern in this region. One of them could be the viscous force which is very dominant in this range of microchannel. The decrease in accuracy of prediction of Akbar et al.[18] could be also related to the simultaneous presence of more than one flow pattern, as discussed earlier.

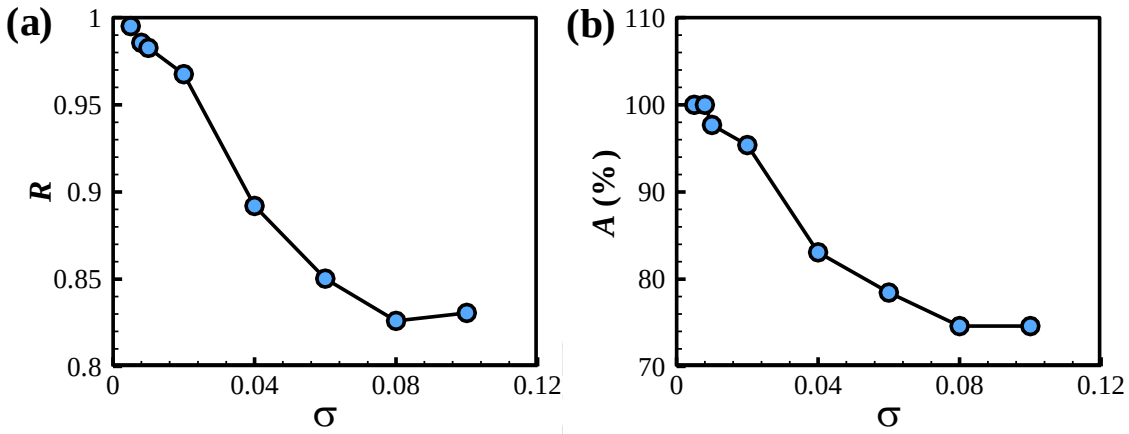

Figure 2.16: Values of regression constant (R) and accuracy, A (%) at various spread constant, (σ).

2.3.5 Prediction of liquid-liquid flow patterns

The prediction of flow patterns for liquid-liquid system were also performed by following similar steps which were executed for gas-liquid flow. The data were collected from experimental flow pattern maps of Salim et al.[16] and Foroughi et al.[15] where mostly droplet, plug, slug and annular flow were observed. The PNN was developed using the collected data where parameters such as phase velocity, diameter of channel, density difference, viscosity ratio, and interfacial tension were incorporated. While training of the PNN was accomplished at σ` = 0.005 where maximum accuracy of A = 97.37 % and maximum value of R = 0.99514 were obtain during test, as shown in Figure 2.16(a) and 2.16(b).

The predicted flow pattern map is shown in Figure 2.17(a) where symbols indicates differents flow patterns. While, the corresponding experimental flow pattern map[16] is shown in Figure 2.17(b). Comparing both the plots, it can be seen that the prediction results is very good with very few mismatching. Similar prediction was also performed for flow pattern map of Foroughi et al.[15] which is shown in Figure 2.17(c) and 2.17(d). The

accuracy of prediction was found to be 91.46 % which is quite good. The accuracy could be improved by incorporating more number of data for training. While the generalized PNN model is not possible without incorporating a huge sets of data for liquid-liquid flow systems which covers the range of microchannel diameters, i.e. d_h = 1000 – 50 µm. So, the study in the current stage lacks a continous sets of flow pattern data with gradual changes in microchannel diameter. So, the prediction of flow patterns and its transition boundaries for liquid-liquid systems in microchannel is left for future scope of study.

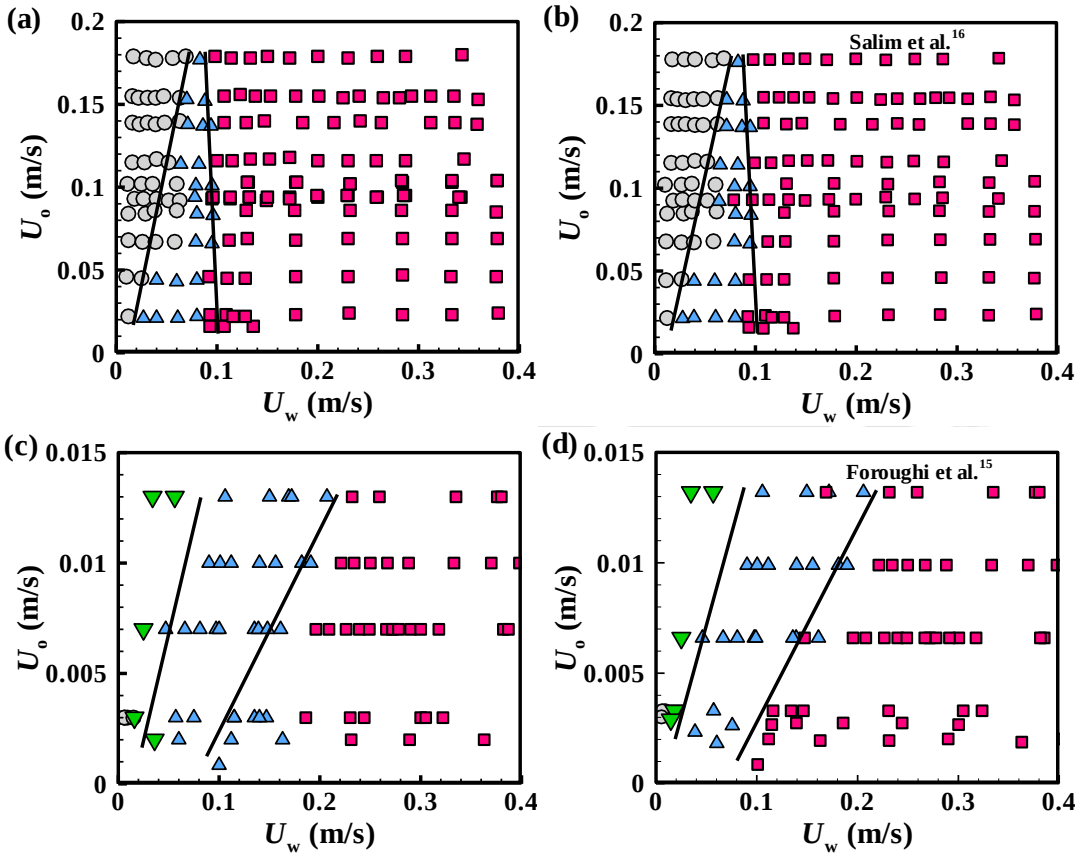

Figure 2.17: Comparison of predicted map with the experimental data for oil-water flow in microchannel with diameter, where (a) and (b) shows the flow pattern in microchannel with d_h = 0.793 mm, obtained by PNN prediction and literature data, respectively. While, (c) and (d) shows the flow pattern in microchannel with d_h = 0.25 mm, obtained by PNN prediction and literature data, respectively. The notations represents various flow patterns:

((●) bubbly/droplet flow, (▲) slug flow, (●) liquid ring flow, (◀) liquid lump flow, (■) annular flow, (♦) churn flow, (▼) plug flow, and (—) transition lines from literature.[15,16]

2.4 SUMMARY

The study in the present chapter reports a probabilistic neural network (PNN) for prediction of flow patterns and their transition boundaries in the range of microchannel for both gas-liquid and liquid-liquid flows. The PNN was trained with various input parameters such as superficial velocities of both phases, channel inclination, interfacial tension, density difference and viscosity ratio of phases. Overall, the PNN showed high accuracy in prediction for the tube diameter of 530 – 50 μm for gas-liquid flow. The flow patterns predicted were compared with its corresponding literature data and found to be in good agreement for all flow patterns except for liquid lump flow. This was because of less number of data available for this flow pattern in literature. The transition boundaries obtained from predicted flow pattern maps were also compared with analytical models. The percentage accuracy of PNN has been found to be higher than the same obtained from various analytical models. The accuracy of PNN prediction was also higher than the Weber number model. This PNN prediction could further be improved by incorporating larger sets of data for those flow patterns (such as, liquid-lump flow) where the prediction accuracy were quite low.

In order to show the potential use probabilistic neural network (PNN) apart gas liquid flow, we carried out flow pattern predictions for liquid-liquid flow patterns. While the prediction for liquid-liquid flow patterns has also been accomplished in similar fashion. Overall, the PNN showed high prediction accuracy (~ 91.46 %) but due to lack of enough of data for some flow patterns, it showed few mismatching. The accurate prediction of

flow patterns for liquid-liquid system will need huge collection of data at various microchannel diameters. Due to unavailability of data in vast numbers, we leave the detailed study on the prediction of liquid-liquid flow system for future scope.

REFERENCES

1. I. A. Basheer and M. Hajmeer, Journal of Microbiological Methods **43**, 3 (2000).
2. J. E. Julia, B. Ozar, J.-J. Jeong, T. Hibiki, and M. Ishii, International Journal of Heat and Fluid Flow **32**, 164 (2011).
3. Y. Mi, M. Ishii, and L. H. Tsoukalas, Nuclear Engineering and Design **204**, 87 (2001).
4. T. Xie, S. M. Ghiaasiaan, and S. Karrila, Chemical Engineering Science **59**, 2241 (2004).
5. T. Tambouratzis and I. Pazsit, Annals of Nuclear Energy **37**, 672 (2010).
6. W. Zhang, F. Y. Shih, N. Jin, and Y. Liu, International Journal of Multiphase Flow **36**, 793 (2010).
7. H. Sharma, G. Das, and A. N. Samanta, AIChE Journal **52**, 3018 (2006).
8. E. Z. Panagou, V. Kodogiannis, and G. J. E. Nychas, International Journal of Food Microbiology **117**, 276 (2007).
9. D. F. Specht, Neural Networks **3**, 109 (1990).
10. M. Hajmeer and I. Basheer, Journal of Microbiological Methods **51**, 217 (2002).
11. E. C. F. p. d. S. Parzen, The Annals of Mathematical Statistics **33**, 1065 (1962).
12. T. Cacoullos, Annals of the Institute of Statistical Mathematics **18**, 179 (1966).
13. P. M. Y. Chung and M. Kawaji, International Journal of Multiphase Flow **30**, 735 (2004).

14. S. Saisorn and S. Wongwises, Experimental Thermal and Fluid Science **34**, 454 (2010).

15. H. Foroughi and M. Kawaji, International Journal of Multiphase Flow **37**, 1147 (2011).

16. A. Salim, M. Fourar, J. Pironon, and J. Sausse, The Canadian Journal of Chemical Engineering **86**, 978 (2008).

17. N. Shao, A. Gavriilidis, and P. Angeli, Chemical Engineering Science **64**, 2749 (2009).

18. M. K. Akbar, D. A. Plummer, and S. M. Ghiaasiaan, International Journal of Multiphase Flow **29**, 855 (2003).

19. A. Serizawa, Z. Feng, and Z. Kawara, Experimental Thermal and Fluid Science **26**, 703 (2002).

20. K. A. Triplett, S. M. Ghiaasiaan, S. I. Abdel-Khalik, and D. L. Sadowski, International Journal of Multiphase Flow **25**, 377 (1999).

21. A. Kawahara, P. M. Y. Chung, and M. Kawaji, International Journal of Multiphase Flow **28**, 1411 (2002).

22. Z. P. Feng and A. Serizawa, Proceedings of the 18th Multiphase Flow Symposium of Japan, Suita, Osaka, Japan, 33 (1999).

23. Z. P. Feng and A. Serizawa, Proceedings of the 37th National Heat Transfer Symposium of Japan I, 351 (2000).

24. S. Saisorn and S. Wongwises, Experimental Thermal and Fluid Science **32**, 748 (2008).

25. K. Z. Mao, K. C. Tan, and W. Ser, IEEE Transactions on Neural Networks **11**, 1009 (2000).

26. N. Brauner, Internal Report-5101, Faculty of Engineering, Tel-Aviv, Israel (2000).

27. R. S. Brodkey, *The Phenomena of Fluid Motions* (Brodkey Publishing, 2004).

28. N. Brauner, International Journal of Multiphase Flow **17**, 59 (1991).

29. N. Brauner, G.F. Hewitt (Ed.), HEDU: Heat Exchanger Design Update **1**, 40 (1998).

30. G. F. Hewitt and S. Jayanti, International Journal of Multiphase Flow **19**, 527 (1993).

31. N. Brauner and D. Barnea, Chemical Engineering Science **41**, 159 (1986).

32. D. Barnea and N. Brauner, International Journal of Multiphase Flow **11**, 43 (1985).

33. D. Barnea, International Journal of Multiphase Flow **13**, 1 (1987).

34. S. Jayanti and G. F. Hewitt, International Journal of Multiphase Flow **18**, 847 (1992).

35. A.-L. Dessimoz, P. Raspail, C. Berguerand, and L. Kiwi-Minsker, Chemical Engineering Journal **160**, 882 (2010).

Chapter 3

Capillary force mediated flow patterns of oil-water microflows

ABSTRACT

In the present chapter, we report the capillary and frictional force mediated transitions of morphologies of an oil-water flow inside a microchannel using experiments and computational fluid dynamic simulations. A number of steady and time-periodic flow patterns is reported with the variations in the interfacial tension, flow ratio, viscosity ratio of the phases, and exchange of inlets. Transitions from slug to plug to droplet to stratified flow patterns were obtained by tuning the interfacial tension. Progressive reduction in the interfacial tension at a constant water-to-oil flow ratio transformed big slugs into smaller plugs, plugs into smaller droplets, and droplets into the stratified flow pattern. Interestingly, the simulation results uncovered a non-monotonic and nonlinear trend of reduction in pressure drop with the decrease in interfacial tension. The change in the pressure drop was correlated to the variation in the slug, plug, or droplet frequency of water at the outlet. The variations in the pressure drop were also associated with the transition from dripping to jetting of water droplet ejection near the channel inlet. Apart from the interfacial tension, the viscosity stratification across the phases was also found to play an important role in converting the slug flow patterns into smaller plugs or droplets. The study also reports the parametric space in which the droplet flow patterns could be obtained inside a microchannel by tuning the flow and viscosity ratios of the phases alongside the interfacial tension. The reported transitions of flow patterns and the pressure drop characteristics can be of significance in improving the efficiency of future microfluidic devices.

This chapter is published in Can. J. Chem. Eng. **93**, 1736 (2015).

3.1 INTRODUCTION

In the present study, using experimental and computational fluid dynamic (CFD) simulations, we explore the transitions of various interfacial flow morphologies with variations in capillary forces. We validated experimental results by estimating the different flow regimes with variations in the water-to-oil flow rate ratio (Q_r).[1] Following this, the interfacial tension was systematically altered for a constant Q_r and the transitions of a host of steady and unsteady flow morphologies including slug, plug, droplet, stratified, and core-annular flow patterns were investigated. Importantly, the experiments and simulations together uncovered that variation in interfacial tension could also lead to a transition from dripping to jetting of drop, plug, or slug release near the inlet. Strikingly, the change in flow patterns with interfacial tension led to variation in slug, plug, or droplet frequencies at the outlet, which in turn led to a non-monotonic change in pressure drop across the channel. The proposed CFD-based methodology to calculate the pressure drop expansively took into account the effects of volume fractions of the liquid phases, curvatures of flow patterns, velocity and viscosity of liquid phases, and the influence of shear forces near the wall and across the interface, which have not been attempted discretely through the previous correlation-based methods for gas-liquid and liquid-liquid microflows.[1-6] The study also uncovered that extreme reduction of interfacial tension might not always produce droplets, because stratified flows could emerge below a critical interfacial tension value. Apart from the variation in the interfacial tension, tuning the viscosity ratio of the fluid phases was found to play an important role in the miniaturization of flow patterns. Transitions in various steady and unsteady flow patterns were also observed when both the interfacial tension and viscosity ratio were varied

together. The results reported can be of significance in improving the efficiencies of future microfluidic devices.

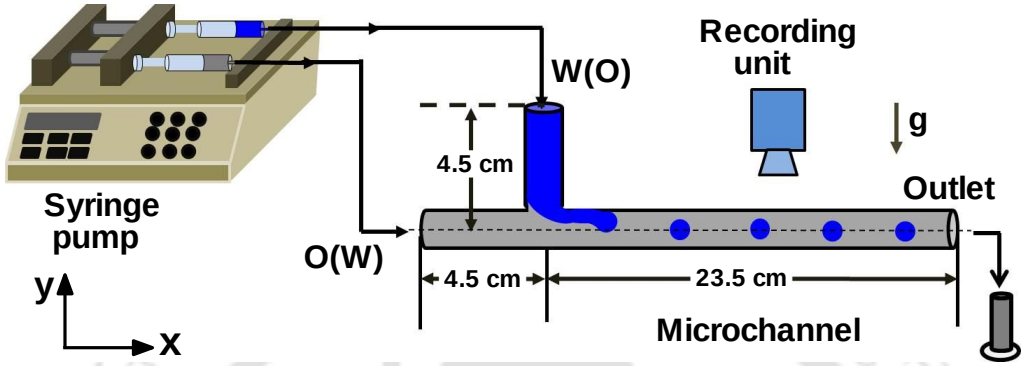

Figure 3.1: Schematic diagram of experimental setup with dimensions (cm) of the circular T-junction microchannel for oil (O)–water (W) flow. Microchannel radius r = 450 µm.

3.2 EXPERIMENTAL METHODS

Table 3.1: Physical properties of oil and water in the experiments and computation.

Physical properties	**Water**	**Silicone oil**	**Water**	**Silicone oil**
	Experiments		Computation	
Density (kg m^{-3})	997	970	1000	1000
Viscosity (Pa s)	0.001	0.34	0.001	0.01
Interfacial tension (mN/m)	25.8		25.8	

The schematic diagram of the experimental set-up (Figure 3.1) consists of a T-shaped microchannel with a circular cross-section, a syringe pump, an image recording unit, and a collector at the outlet. The T-shaped microchannels of length l = 0.28 m, and radius r = 450 × 10^{-6} m were molded from glass. The inlets of the channels were I = 0.045 m long. Silicone oil (Merck Millipore; SD2S620068) and deionized (DI) water were used as working fluids to generate oil-water flow features inside the channel. Channel lengths were deliberately made longer in order to obtain fully-developed flow morphologies in the

downstream flow. The physical properties of the liquids employed in the experiments at room temperature appear in Table 3.1. Fluids were introduced interchangeably from both inlets. For example, in one set of experiments, the oil (water) was introduced from the horizontal (vertical) inlet, whereas in the other set the oil (water) was introduced from the vertical (horizontal) inlet.

Table 3.2: Velocities of water and oil phase used for experiment.

Velocity Ratio $Q_r = U_w/U_o$	Experimental ($m\ s^{-1}$: $m\ s^{-1}$)
0.1	0.001:0.01
0.5	0.001:0.002
1	0.001:0.001
5	0.005:0.001
10	0.01:0.0.001

Table 3.3: Oil-water interfacial tension with variation in the surfactant concentration.

Weight of SDS (gm)	**Volume of water (ml)**	**Concentration (mol/L)**	**Interfacial tension (mN/m)**
0	40	0	25.8
3.33	40	0.29	8.2
6.68	40	0.58	8.0
13.45	40	1.165	7.5
26.6	40	2.30	5.3

Table 3.4: Viscosity of glycerol solution at different concentration (v/v).

% (v/v) of glycerol in water	**Viscosity (Pa s)**
0% glycerol	0.001
25% glycerol	0.003
50% glycerol	0.005
75% glycerol	0.03

The glass microchannels were cleaned thoroughly following the standard protocol[7] before the experiments were started. The cleaning of the microchannel started with ultra-sonication for 10 min in acetone and methanol baths, followed by a treatment with piranha solution (H_2SO_4:H_2O_2, 3:1) for 15 min. The microchannel was then immersed in DI water for 5 min. The channels were dried initially by blowing nitrogen gas, followed by being put in an air-oven for 20 min at 85 °C. Oil and water were injected into the channel with the help of a syringe pump (Harvard, PHD 2000). Leak-proof connections were made between the pump and the microchannel. Different interfacial morphologies were obtained by varying the flow rates of oil and water, and then subsequently changing the interfacial tension and the ratio of the viscosities of the fluids. The flow ratio was typically varied from $Q_r = U_w/U_o = 0.1 – 10$, the interfacial tension (γ) was varied from 0.0258 – 0.0053 N/m, and the viscosity of the water layer (μ_w) was varied from 0.001 – 0.03 kg/m s, as shown in Tables 3.2 – 3.4.

An anionic surfactant, sodium dodecyl sulphate (SDS), was added at different concentrations with water to vary the interfacial tension. Table 3.3 summarizes the variation in the interfacial tension with changes in surfactant concentration (mol/L) in the water. Interfacial tensions were measured with a digital tensiometer (Krüss) employing a standard du Noüy ring (Pt/Ir) method following the ASTM Standard procedure D1331-11 (2001). In order to change the viscosity of the water layer, we introduced glycerol at different concentrations: (volume of glycerol/volume of solution) 0, 0.25, 0.50, and 0.75 L/L. The viscosities of the water phases which were mixed with glycerol at different concentration were measured employing a plate and cone viscometer following the ASTM Standard procedure D1331-11 (2001), as shown in Table 3.4.

The flow patterns and various interfacial phenomena were video-recorded using a CCD camera at 50 fps (HDR-XR160E, Sony). After the oil-water mixture issued from the outlet of the channels, it was kept undisturbed for ~20 min in order for complete separation of the phases, and then the volumetric flow rates for each phase were calculated by evaluating the volume accumulated per unit time of oil and water. In order to determine the uncertainty in flow velocity, a total of three readings were made for each flow parameter and was found to be a maximum of 1%.

3.3 COMPUTATIONAL METHODOLOGY

The fluids were assumed to be Newtonian and incompressible. The two-dimensional (2D) rectangular geometry T-shaped microchannel, aligned along the *x*-*y* plane, was taken as the computational domain, as shown in the Figure 3.1. A series of simulations showed that the downstream flow characteristics remained similar when the length of the microchannel was > 25 mm, which reduced the computational domain and saved computational time. The constant physical properties of the liquids employed for the simulations are provided in the Table 3.1, and the flow conditions are provided in Table 3.2.

It may also be noted here that the comparison between the experimental and computational results in the present work was rather qualitative in nature because the viscosity of oil was set to a much lower value in the computations than in the experiments. This helped us avoid the 'stiffness' of the computational system, which the dimensional numerical solver could have encountered while tracking the interface of a two-phase flow with a large viscosity ratio. The use of lower viscosity for computations could also be justified from recent experimental and computational results,[2,8] which showed minimal changes in flow morphologies beyond a critical value of the phase viscosity ratio. Gravitational force was

assumed to be in the negative *y*-direction. The following continuity and equations of motion were employed to describe the motions of oil and water layers inside the microchannel.

$$\nabla \cdot \mathbf{u} = 0 \tag{3.3.1}$$

$$\frac{\partial \mathbf{u}}{\partial t} + \mathbf{u} \cdot \nabla \mathbf{u} = -\frac{1}{\rho}\nabla p + \nu \nabla^2 \mathbf{u} + \mathbf{g} \tag{3.3.2}$$

where **u**, p, μ, ρ, and $\nu (= \mu / \rho)$ denote the velocity vector, pressure, viscosity, density, and kinematic viscosity, respectively. The notation **g** represents the vector for acceleration due to gravity. The oil-water flow was modelled employing the volume of fluid method (VOF) from the commercial software ANSYS FLUENT™. The VOF[8-10] method initially solved a single set of momentum equations, and then tracked the interface by solving the following volume fraction equation satisfying the continuity equation with the restriction $\sum_{i=1}^{2} \alpha_i = 1.$

$$\frac{1}{\rho_i}\left[\frac{\partial}{\partial t}(\alpha_i \rho_i) + \nabla.(\alpha_i \rho_i \mathbf{u}_i)\right] = \sum_{j=1}^{2}\left(\dot{m}_{ij} - \dot{m}_{ji}\right) \tag{3.3.3}$$

Here α_i, ρ_i, and μ_i denote the volume fraction, density, and viscosity of the i^{th} fluid. The notation $\dot{m}_{ij}$ ($\dot{m}_{ji}$) denotes the rate of mass transfer from phase *i* (*j*) to phase *j* (*i*). In the simulations, oil and water were treated as the primary (α_i = 1) and secondary (α_i = 2) phases and at the interface the volume fraction was 0 < α_i < 1. The geometry was meshed with the preprocessor from ANSYS FLUENT™. The 2D geometry was divided into a structured orthogonal mesh of 72,500 cells, which provided grid-independent solutions. The inlets were modelled with the velocity inlet and the outlet was modelled employing

the pressure outlet boundary conditions. The walls of the microchannel were assumed to be non-slipping and impermeable ($\mathbf{u} = 0$).

The unsteady governing equations together with the boundary conditions were solved using the CFD solver of ANSYS FLUENT^{TM}, which uses a finite volume method to convert the governing equations to an algebraic form. A time step size between 10^{-6} and 10^{-5} s was found to be the optimum to obtain a converged solution for each time step. In this study, we employed the PRESTO scheme for pressure interpolation, SIMPLE for the pressure-velocity coupling, and QUICK for upwinding the convective terms of the momentum equation. The liquid-liquid interface tracking module of the software follows the continuum surface force (CSF) model.[9] The most accurate geometric reconstruction model, along with the implicit body force treatment, were employed to reconstruct the interface in every time step. The mixing laws $\rho = \alpha_2 \rho_2 + (1-\alpha_2)\rho_1$ and $\mu = \alpha_2 \mu_2 + (1-\alpha_2)\mu_1$ were used to calculate μ and ρ of the mixture.

Most of the earlier studies on two-phase flow show the pressure drop characteristics to be a function of flow ratio. But the effect of reduction of interfacial tension on the pressure drop is yet to be studied. In order to calculate the time-averaged pressure drop across the two inlets and outlet of the channel, firstly, the steady state or time-periodic steady state solutions were obtained for the flow. Following this, the "Data Time Sampling" option was turned on in the "Solve/Iterate" panel of the software while iterative time marching was performed for each cycle of the time periodic solutions. Thereafter, 3 sampling lines were drawn 1 mm downstream of the two inlets, and 2 mm upstream of the outlet to avoid end effects. Then the "Area Weighted Average" of the "Total Pressure" option was evaluated at these sampling lines. The pressure drop across horizontal (vertical) inlet and

the outlet was termed as Δp_h (Δp_v). Finally, pressure drops per unit length ($\Delta p_h/l$ and $\Delta p_v/l$) were calculated by dividing pressure drop values with the respective distance between sampling lines.

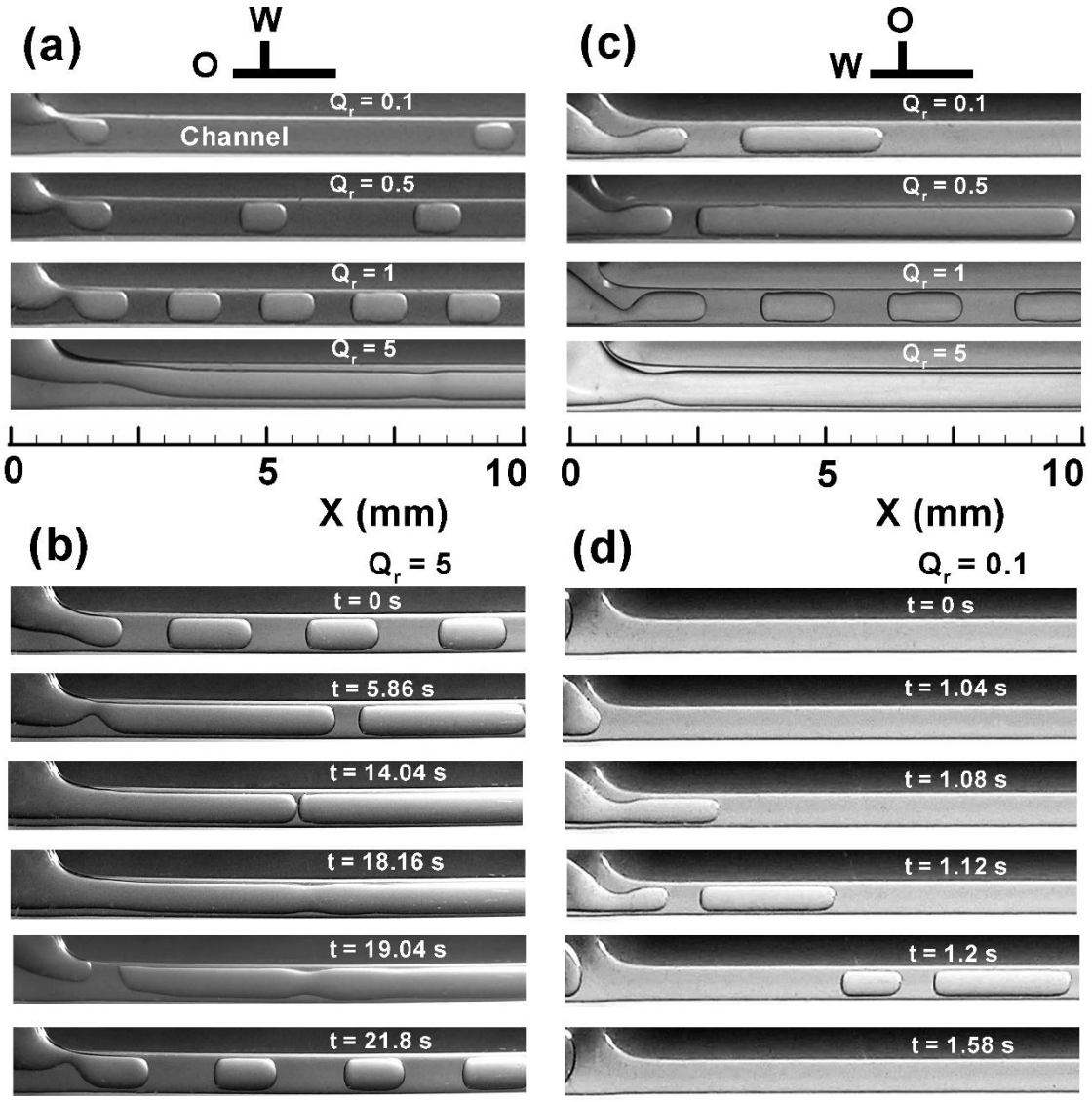

Figure 3.2: Experimental observation of oil-water flow morphologies. (a) Flow patterns at different velocity ratios, $Q_r = U_w/U_o$ with oil (O) in horizontal inlet and water (W) in vertical inlet, as schematically shown above. (b) Time-periodic transition from slugs to core-annular flow at different time intervals when $Q_r = 5$. (c) Flow patterns observed with oil (water) in vertical (horizontal) inlet. (d) Unsteady ejection of non-uniform slugs at

different time intervals when Q_r = 0.1; γ = 0.0258 N/m, Re_w = 0.9 – 4.5, We_w = 3.5 × 10^{-5} – 8.7 × 10^{-4}, Ca_w = 3.9 × 10^{-5} – 2 × 10^{-4}, and Bo = 0.008.

3.4 RESULTS AND DISCUSSION

Microscale flows are often associated with the dominance of either capillary or frictional forces over inertial and gravitational forces.[11] This is also synonymous with the lower values of dimensionless Reynolds ($Re = \rho Ud / \mu$), Bond ($Bo = \Delta\rho g d^2 / \gamma$), and Weber ($We = \rho U^2 d / \gamma$) numbers. Here, the symbols ρ, $\Delta\rho$ (= ρ_w - ρ_o), μ, d, γ, and U denote the density, difference in density of the phases, viscosity, characteristic length scale, interfacial tension, and average velocity, respectively. The subscript 'w' and 'o' represents the water and oil phases, respectively. Furthermore, the magnitude of the capillary number ($Ca = \mu U / \gamma$) indicates the controlling factor between viscous and surface tension forces. A recent study showed interesting transitions in the flow patterns inside 'flow-focused' microchannels when the strength of the weak inertial force is altered.[1] For example, water droplets in a continuous oil medium could be observed when the velocity of water (U_w) at the inlet was significantly lower than the oil phase (U_o). Increase in the water flow rate led to the formation of plug and slug flow patterns, which transformed into a core-annular flow at higher values of Q_r (= U_w / U_o). In the following, we show alternative pathways to developing steady and unsteady flow morphologies by tuning the capillary and viscous forces inside a 'T' shaped microchannel.

Figure 3.2 shows the experimentally observed transitions in the flow morphologies in a 'T' shaped microchannel with the variation in Q_r, emulating the recent experiments inside flow-focused channels.[1] The typical ranges of dimensionless numbers for the experiments were evaluated as Re_w = 0.9 – 4.5, We_w = 3.5 × 10^{-5} – 8.7 × 10^{-4}, Ca_w = 3.9 × 10^{-5} – 2 ×

10^{-4}, and Bo = 0.008. The subscript 'w' in the notations indicate that the parameters were evaluated based on the physical and flow properties of the water phase. Figure 3.2(a) depicts that when water (oil) was introduced vertically (horizontally), the frequency of the water plugs increased, as Q_r was progressively increased. The microchannel was made of glass in which the water (oil) had a much lower (higher) wettability, as reported experimentally in previous research.[1] Thus, wetting of the oil phase on the channel wall was observed while water plugs with lower wettability were found to be rather dispersed into the continuous oil phase. Also to experimentally ensure the correct identification of dispersed phase, we dyed the continuous phase with iodine, which became reddish in color from being transparent as shown in **Appendix A**. The criteria set for identification of slug and plug flow is also mentioned in **Appendix A**. Subsequently, an increase in Q_r amplified the frequency of water plugs (Q_r = 0.5) and at Q_r = 1, and the plug flow patterns were converted into slugs with increased lateral widths. At higher Q_r ~5 and 10, the water slugs coalesced to develop an unsteady core-annular flow pattern with a water core, encapsulated by a thin layer of oil wetting the glass wall.

Importantly, at Q_r = 5, the oil-water interface of the core-annular flow showed a time-periodic behavior, as shown in Figure 3.2(b), which was very similar to the one reported by Kawahara et al.[12] for gas-liquid flows. The time-periodic cycle started with the formation of slugs (t = 0 s) from the core annular flow. Water slugs were surrounded by a highly viscous and thin oil phase, which led to a slow translation of flow structures to downstream in the channel. Over time, the slugs coalesced to develop larger slugs (t = 5.86 s and 14.04 s). At the end of the cycle, the larger slugs coalesced to form a core-annular flow (t = 18.16 s) with an unstable wavy oil-water interface, which underwent

capillary instability to restore the flow pattern to an array of water slugs dispersed in a continuous oil phase (t = 19.04 s). In this situation, the release of the water phase at the inlet followed a combination of dripping and jetting mechanisms during this time-periodic cycle. The larger slugs and core-annular flow patterns were the consequence of a jetting of the water phase into the channel while smaller water slugs or plugs near the inlet were formed following the dripping mechanism.

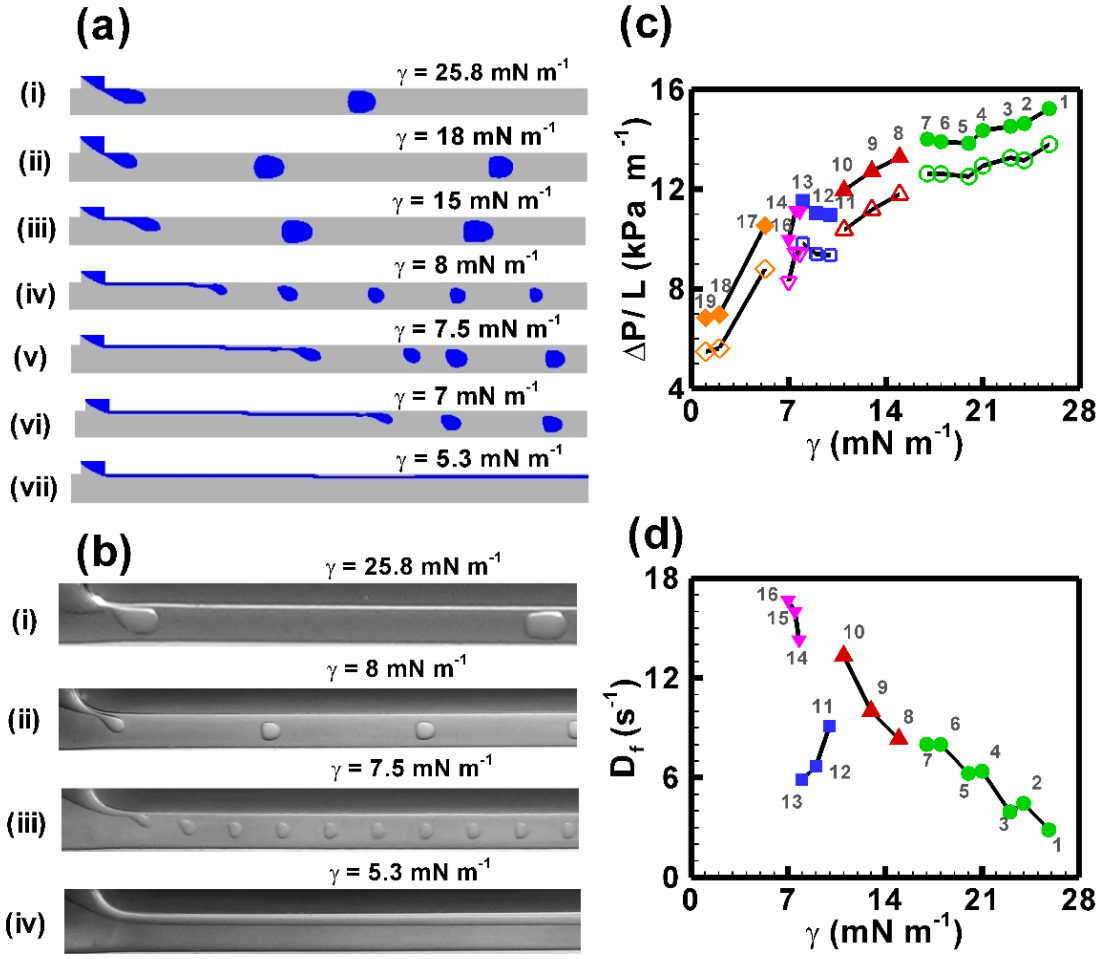

Figure 3.3: Transitions in the flow patterns with variation in interfacial tension γ obtain through (a) CFD simulations, and (b) experiments, for Q_r = 0.1 at various values of γ; darker and lighter shades represent water and oil phases, respectively. Images (i) – (vii) represents flow morphologies at γ = 0.0258, 0.018, 0.015, 0.008, 0.0075, 0.007, and

0.0053 N/m. Images b(i) – b(iv) represents flow morphologies at γ = 0.0258, 0.008, 0.075, and 0.0053 N/m. (c) Variation of $\Delta p / L$ ($\Delta p_h / l$: filled symbols; $\Delta p_v / l$: hollow symbols) with γ, for Q_r = 0.1 obtained through numerical simulations. (d) Variation in D_f with γ obtained through numerical simulations. Here, Bo = 0.008 – 0.04, We_w = 3.5×10^{-5} – 1.7×10^{-4}, Ca_w = 3.9×10^{-5} – 1.9×10^{-4}, Re_w = 0.9.

Exchanging the inlets of the phases was also found to influence the flow patterns especially at the lower Q_r. Figure 3.2 (c) shows that when the water (oil) was introduced horizontally (vertically), the flow patterns in the range of Q_r = 0.1 – 0.5 became unsteady. The length of the water plugs initially increased due to the increased in velocity ratio, ($Q_r = U_w / U_o$). But at Q_r = 1, a steady slug flow is observed whose slug length is almost equal to the distance between two consecutive slugs. It shows the transition from an unsteady to steady flow at Q_r = 1. So, water plug lengths initially increased and then decreased before transition to annular flow takes place. Figure 3.2(d) shows the formation cycles of unsteady non-uniform slug flows at lower values of Q_r. In contrast, for Q_r > 0.5, the flow patterns remained identical to the situation when water (oil) was introduced vertically (horizontally). For example, steady slug patterns were observed for Q_r = 1 in Figure 3.2(c). At a higher value of Q_r = 5, again the time-periodic core-annular flow pattern was observed, as in Figure 3.2(b). Concisely, the experiments revealed that, similar to flow-focusing channels, oil-water flow inside a ‘T’ shaped microchannel could also develop a variety of transient and steady plug, slug, and core-annular flow patterns with variation in phase flow rates.

Importantly, when the inlet flow rates of the phases were kept fixed, the flow patterns could also be altered by changing the oil-water interfacial tension (γ). Figure 3.3 shows transitions in the flow morphologies and subsequent changes in the pressure drop

characteristics across the channel with variation in γ at Q_r = 0.1. The dimensionless numbers were varied in the ranges Bo = 0.008 – 0.04, We_w = 3.5 × 10^{-5} – 1.7 × 10^{-4}, and Ca_w = 3.9 × 10^{-5} – 1.9 × 10^{-4}, while Re_w = 0.9 was kept constant. Images (i) – (vii) of Figure 3.3(a) shows the CFD simulations for oil-water flow at different values of γ where the darker and the lighter shades represent the water and oil phases, respectively. Images (i) – (iv) of Figure 3.3(b) shows the experimental results of a similar system showing the flow transitions with decreasing γ. The simulations suggest that when γ was large the water plugs were ejected out of the vertical inlet following the dripping mechanism, as shown by image (i) of Figures 3.3(a). While image (ii) of Figure 3.3(a) shows that a minor reduction in γ could only increase the frequency of plugs inside the channel. Images (iii) and (iv) show that below a threshold value of γ, a transformation from dripping to jetting took place and the droplets were ejected from the end of jet, nearly at the middle of the channel. Reduction of γ facilitated the formation of smaller droplets with higher surface-to-volume ratio owing to the net reduction in total surface free energy and also showed increase in water jetting length. Images (iv) and (v) show that the miniaturized droplets at higher frequencies continuously issued out of the water jet downstream in the channel. Images (v) – (vii) suggest that with further reduction in γ the droplet flow could transform into a stratified flow inside the channel. It may be noted here that although there were remarkable similarities in the flow morphologies between experimental and computational flow patterns in Figures 3.3(a) and 3.3(b), they did not exactly match in terms of parametric space. The reasons for the differences could be attributed to the dissimilarities between experiments and computations.in the geometrical parameters and physical and flow properties of the phases.

The CFD simulations also helped in estimating the changes in the pressure drop ($\Delta p / l$) characteristics across the channel while the flow pattern transitions took place with the change in γ. Figures 3.3(c) and 3.3(d) show the variations in $\Delta p / l$ and droplet frequency (D_f) with γ. Here, D_f is defined as the number of dispersed phase units, such as slugs, plugs or droplets, passing through the outlet of the channel per unit time. $\Delta p_h / l$ ($\Delta p_v / l$) are represented by the filled (hollow) symbols corresponding to the pressure drop between the horizontal (vertical) inlet and the outlet. It may be noted here that the required pressure drop to maintain the same flow rate across a channel would be larger for a single phase oil flow with higher viscosity than a less viscous water flow. Thus, for the oil-water flow, it could easily be predicted that, with an increase in the frequency of water droplets, plugs, or slugs inside the channel, $\Delta p_h / l$ and $\Delta p_v / l$ would be lower compared to the single phase oil flow. Figures 3.3(c) and 3.3(d) show a striking dependence on the droplet frequency of the water phase with the change in $\Delta p / l$ across the channel. Point 1 shows that when γ was high and very few water plugs were ejected from the inlet following a dripping mechanism, the $\Delta p / l$ was highest and the D_f was lowest. However, the D_f increased and $\Delta p / l$ reduced with the reduction in γ, as shown by points 1–7. In point 8, a transition from a dripping to jetting mechanism of water droplets took place with further reduction in γ which was observed in images (ii) – (iv) of Figure 3.3(a). This was also signified by a non-monotonic increasing trend in D_f and reduction in $\Delta p / l$. Following this, $\Delta p / l$ progressively reduced and D_f increased with reduction in γ, as shown by the points 8 – 10. Importantly, the images (iii) and (iv) of Figure 3.3(a) show that in this parametric window, the length of the ejected jet from the inlet increased with reduction in γ. Points 11 – 13 show a reduction in D_f and increase in $\Delta p / l$. Beyond this point, $\Delta p / l$ progressively

decreased and D_f increased with reduction in γ, as shown by points 14 – 16 and, images (v) and (vi) of Figure 3.3(a). The change from droplet to stratified flow regimes [images (vi) and (vii) of Figures 3.3(a)] was also indicated by a discontinuous transition in $\Delta p / l$, as shown by points 16–17 in Figure 3.3(c). Here, Figure 3.3 uncovers interesting non-monotonic and nonlinear reduction of the pressure drop across the channel with progressive reduction in the oil-water interfacial tension. The figure also highlights that the transitions in flow morphologies were very closely associated with the pressure drop changes and the frequency of flow patterns at the outlet. The pressure drop evaluated in this study from the CFD approach is expected to be far more accurate than the previously employed correlation-based techniques.[1-6]

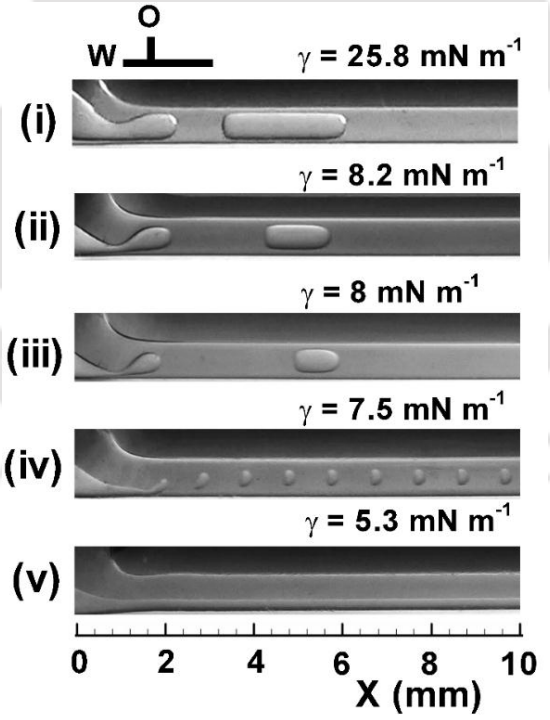

Figure 3.4: Experimental flow transitions from unsteady slug flow to steady droplet to stratified flow. Images (i) – (v) show the flow pattern observed for Q_r = 0.1 with the variation in γ, when oil (water) entered through the vertical (horizontal) inlet.

Figures 3.4(i) – (v) show interesting flow behaviours when water (oil) was introduced vertically (horizontally) and γ was progressively reduced, when Q_r = 0.1. The major observations are: (i) the flow pattern gradually transformed from slug to plug to droplet to stratified regime with reduction in γ; (ii) the periodicity of the slugs, plugs, and droplets increased inside the channel before the stratified flow regime emerged; and (iii) transition from the dripping to jetting mechanism took place for the dispersed water phase while the droplet flow became the stratified flow. Interestingly, steady patterns of water droplets inside the channel were observed when γ was considerably reduced [Figure 3.4(iv)]. Figures 3.3 – 3.4 together show that although the reduction in γ could transform steady or unsteady slug or plug flow patterns into droplets, below a threshold value of γ, stratified flow patterns could emerge, which had a smaller surface-to-volume ratio than droplet flow patterns.

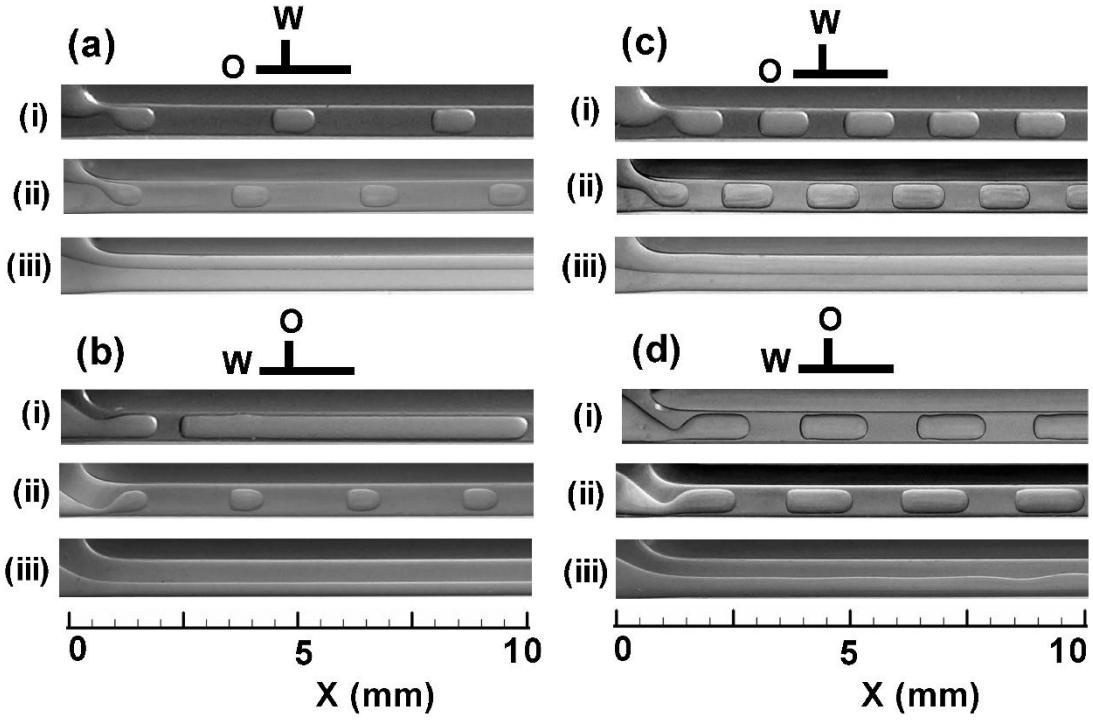

Figure 3.5: Experimental flow transition of plug or slug flow to stratified flow with decreasing γ. Images (a) and (b) corresponds to Q_r = 0.5, (c) and (d) corresponds to Q_r = 1.

Here, (a) and (c) shows the oil (water) entered through horizontal (vertical) inlet. While (b) and (d) shows that the oil (water) entered through vertical (horizontal) inlet. The images (i) – (iii) correspond to flow patterns observed at γ = 0.0258, 0.0075, and 0.0053 N/m, respectively.

Figure 3.5 shows that even when the inlet flow rate of water was significantly higher (Q_r = 0.5 and 1) the miniaturization in flow patterns could be enforced by reducing γ. The dimensionless numbers in these experiments varied in the range of Bo = 0.008–0.04, We_w = 3.5×10^{-5} – 1.7×10^{-4}, and Ca_w = 3.9×10^{-5} – 1.9×10^{-4}, while Re_w = 0.9 was kept constant. The images (i) – (iii) of Figure 3.5(a) show the flow pattern transition for Q_r = 0.5 when the oil was injected through the horizontal inlet. With reduction in γ, the slugs or plugs progressively converted to smaller plugs with higher frequency before stratified flows appeared at very low γ. The images (i) – (iii) of Figure 3.5(b) show that even exchanging the inlets for the oil and water phases could produce similar flow morphologies with reduction in γ. With further increase in the water flow rate to Q_r = 1.0, we observed a direct transition from slug to stratified flow regimes with reduction in γ, as shown by (i) – (iii) of Figure 3.5(c). The dimensionless numbers in experiments were varied in the range Bo = 0.008–0.04, We_w = 3.5×10^{-5} – 1.7×10^{-4}, and Ca_w = 3.9×10^{-5} – 1.9×10^{-4}, while Re_w = 0.9 was kept constant. Again, images (i) – (iii) of Figure 3.5(d) show that exchanging the inlets had very little influence on flow morphologies in this flow regime.

It may be noted here that the time-periodic core-annular flows at higher flow rates Q_r = 5 or 10 (as shown in Figure 3.2) could also be converted into steady stratified flows at lower values of γ. However, for the sake of brevity, the experimental flow patterns are not pictorially reported in this work. At Q_r = 5 or 10, the decrease in interfacial tension due to

higher concentration of surfactant loading also led to increase in wettability of water phase towards channel wall. Due to this both phases wet the wall resulting in a stratified flow.

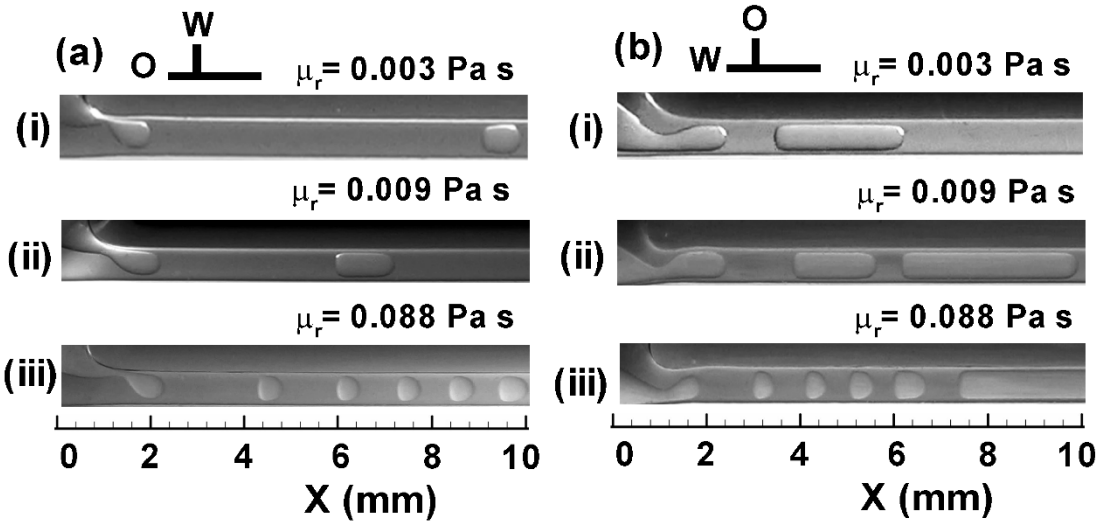

Figure 3.6: Experimental flow transition of plug or slug flow patterns into droplet flow when viscosity of water (μ_w) was increased. In all cases Q_r = 0.1 and γ = 0.0258 N/m. (a): oil (water) entered through horizontal (vertical) inlet; (b): oil (water) entered through vertical (horizontal) inlet. (i – iii) correspond to μ_w = 0.001, 0.003, and 0.03 kg/m s, respectively. Here, viscosity ratio or contrast, $\mu_r = \mu_w / \mu_o$, which is varied by varying the viscosity of water, μ_w as 0.001, 0.003 and 0.03 Kg/m s and keeping the viscosity of oil, μ_o constant at 0.34 Kg/m s. In this way we get values of μ_r as 0.003, 0.009, and 0.088, respectively.

Apart from reducing γ at the oil-water interface by the addition of surfactants, when water is mixed with glycerol at different concentrations the viscosity ratio ($\mu_r = \mu_w / \mu_o$) across the interface changed, as shown in the Table 3.4. It may be noted here that glycerol and water have similar surface tensions, and interfacial tension did not change appreciably when glycerol was added to water to increase the viscosity. Figure 3.6 shows that for a constant flow ratio at the inlet (Q_r = 0.1), a progressive increase in μ_r due to increase in μ_w, could also lead to a droplet flow pattern. The dimensionless numbers for experiments

in this case varied in the range Bo = 0.008, $We_w = 3.5 \times 10^{-5}$, $Ca_w = 3.9 \times 10^{-5} - 1.2 \times 10^{-3}$, and Re_w = 0.03 – 0.9. Previously, Figure 3.2 showed that reduction in inertial influence could lead to flow patterns with a high surface-to-volume ratio having a lower frequency of flow features at the outlet. While, Figure 3.6 shows that when the effect of weak inertial influence was further diminished by increasing the water phase viscosity, droplet flow patterns could emerge with higher frequency inside the flow domain.

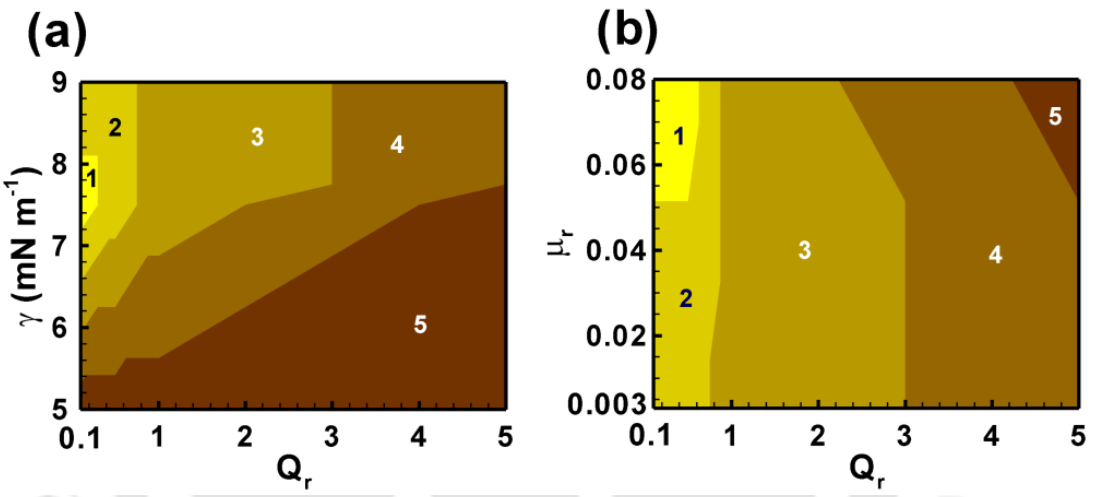

Figure 3.7: Contour plots showing regions for different flow patterns in which droplet, plug, slug, core-annular, and stratified flow patterns are represented by the numbers 1 – 5, respectively. Experimentally observed transitions of flow patterns (a) on the Q_r and γ planes, (b) on the Q_r and μ_r planes.

Figures 3.7(a) – 3.7(b) summarize the variations in experimental flow patterns in the Q_r versus γ and Q_r versus μ_r planes. Location 1 suggests that at intermediate values of γ (0.007 – 0.008 N/m), at considerably lower values of Q_r (< 1), and at moderate-to-high values of μ_r (> 0.05) droplet flow patterns could be expected inside 'T' shaped channels. Further, the plots shows a window of parameters where a progressive transition from the droplet to the plug (location 2), to the slug (location 3), to the annular (location 4), to the

stratified (location 5) flow patterns could be observed with reduction in γ when the $Q_r < 1$ (i.e. a point is moving downward keeping Qr constant). In comparison, for fixed γ and μ_r similar transitions could be observed when Q_r was progressively reduced. The plots also suggest that the effect of μ_r was only prominent in the regime where Q_r was low ($Q_r < 0.8$). Briefly, the contour plots in Figure 3.7 uncover the parameter space in which the flow patterns with higher surface-to-volume ratios, such as droplets and smaller plugs, could be obtained.

3.5 SUMMARY

In the present chapter, a combined experimental and computational study uncovered the effects of interfacial tension and viscosity on the flow patterns and pressure drop characteristics of an oil-water flow inside 'T' shaped microchannels. The important conclusions are as follows.

Transitions from slug, to plug, to droplet, to core-annular, to stratified flow patterns were obtained by tuning the oil-water interfacial tension. Progressive reduction in interfacial tension at a constant oil-to-water flow ratio transformed big slugs into smaller plugs, and plugs into smaller droplets. The simulations uncovered a non-monotonic and nonlinear reduction in pressure drop with a decrease in interfacial tension. The change in pressure drop could be directly correlated to the frequency of the slug, plug, or droplet flow patterns at the outlet. The transitions from dripping to jetting mechanism of water droplet ejection at the inlet were also associated with some distinctive pressure drop change across the channel.

The study also identifies the pathways to miniaturizing the flow patterns, which enables the availability of a higher surface-to-volume ratio for the flow patterns inside

microfluidic devices. At considerably lower values of the water-to-oil flow and water-to-oil viscosity ratios, droplet flow patterns could emerge when the magnitude of the oil-water interfacial tension was moderately low. Importantly, the study indicates that reducing the interfacial tension to extremely smaller values might not always be useful for microfluidic applications, because this could lead to stratified flow patterns with lower surface-to-volume ratios than the targeted droplet flow patterns. The reported transitions of the flow patterns and the subsequent pressure drop characteristics can be significant in improving the efficiency of future microfluidic devices.

3.6 ACKNOWLEDGEMENTS

We acknowledge the financial support for this work from DST SERB, India, (No. SR/S3/CE/0079/2010), DEITY grant no. 5(9)/2012-NANO and DST Fast Track Scheme (No. SR/FTP/ETA-02/2011). Supports from Mr. Vijeet Tiwari and Mr. Amit Kr. Singh are gratefully acknowledged.

3.7 REFERENCES

1. H. Foroughi and M. Kawaji, International Journal of Multiphase Flow **37**, 1147 (2011).
2. P. Garstecki, M. J. Fuerstman, H. A. Stone, and G. M. Whitesides, Lab on a Chip **6**, 437 (2006).
3. M. N. Kashid and D. W. Agar, Chemical Engineering Journal **131**, 1 (2007).
4. A. Salim, M. Fourar, J. Pironon, and J. Sausse, The Canadian Journal of Chemical Engineering **86**, 978 (2008).
5. F. P. Bretherton, Journal of Fluid Mechanics **10**, 166 (1961).

6. M. J. Fuerstman, A. Lai, M. E. Thurlow, S. S. Shevkoplyas, H. A. Stone, and G. M. Whitesides, Lab on a Chip **7**, 1479 (2007).
7. Q. Chen, G. Li, Q. H. Jin, J. L. Zhao, Q. S. Ren, and Y. S. Xu, Journal of Microelectromechanical Systems **16**, 1193 (2007).
8. R. Raj, N. Mathur, and V. V. Buwa, Industrial & Engineering Chemistry Research **49**, 10606 (2010).
9. J. U. Brackbill, D. B. Kothe, and C. Zemach, Journal of Computational Physics **100**, 335 (1992).
10. D. A. Hoang, V. van Steijn, L. M. Portela, M. T. Kreutzer, and C. R. Kleijn, Computers & Fluids **86**, 28 (2013).
11. K. A. Triplett, S. M. Ghiaasiaan, S. I. Abdel-Khalik, and D. L. Sadowski, International Journal of Multiphase Flow **25**, 377 (1999).
12. A. Kawahara, P. M. Y. Chung, and M. Kawaji, International Journal of Multiphase Flow **28**, 1411 (2002).

Chapter 4

Electric field mediated spraying of miniaturized droplets

ABSTRACT

In the present chapter, we report a facile and non-invasive way to disintegrate a microdroplet into a string of further miniaturized ones under the influence of an external electrohydrodynamic field inside a microchannel. The deformation and breakup of the droplet was engendered by the Maxwell's stress originating from the accumulation of induced and free charges at the oil-water interface. While at smaller field intensities (0 – 0.83 MV/m) the droplet deformed into a plug, at relatively higher field intensities (1.16 MV/m) a pair of droplets having opposite surface charge was formed. The charged droplets showed an interesting periodic bridging and breakup during their translation motion across the channel. For even higher field intensities (1.19 – 3.56 MV/m), the entire droplet underwent dielectrophoresis towards one of the electrodes before experiencing a strong attractive force from the other electrode to deform into a shape of a Taylor cone. With progress in time, mimicking the electrospraying phenomenon, the cone-tip periodically ejected a string of miniaturized water droplets to form a microemulsion inside the channel. The frequency and size of the droplet ejection could be tuned by varying the applied field intensity. A water droplet of ~214 μm diameter could continuously eject droplets of size ~10 μm or even smaller to form a microemulsion inside the channel.

This chapter is published in Electrophoresis, **38**, 1450 (2016).

4.1 INTRODUCTION

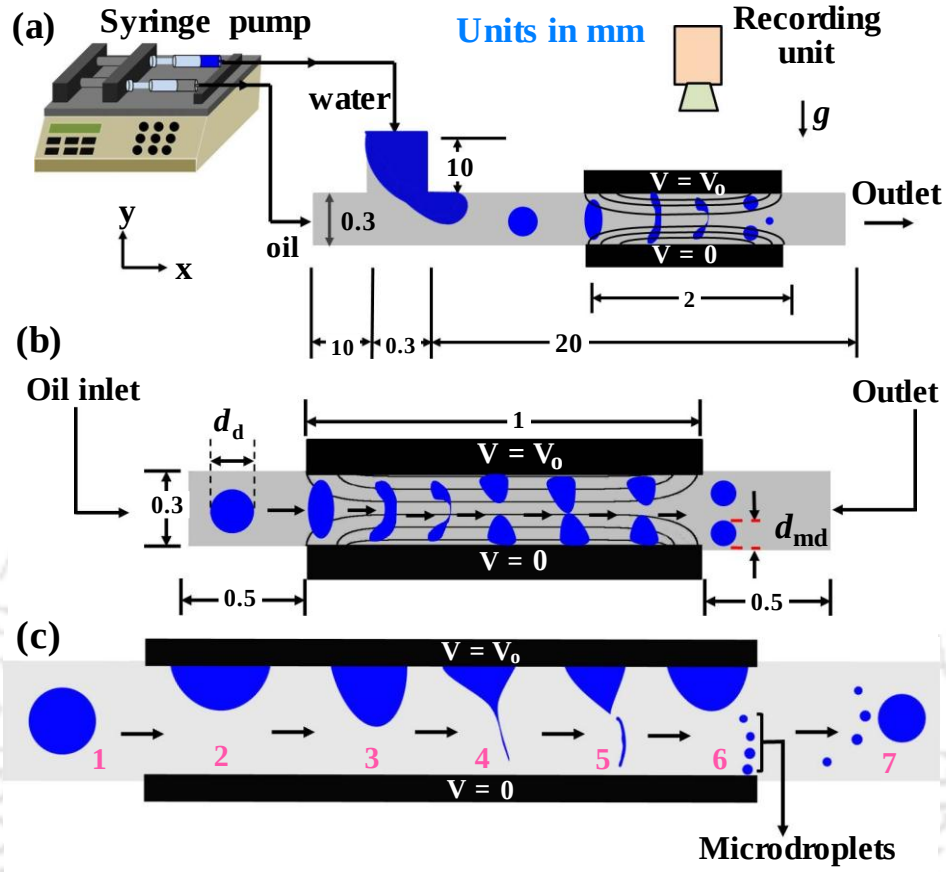

Figure 4.1: (a) Schematic diagram of the experimental setup with dimensions in mm. Oil (Water) was infused through horizontal (vertical) inlet using syringe pumps, represented by the lighter (darker) shade. Image (b) schematically shows the geometry considered for the computational study. The image shows the bridging-breakup mechanism of charged droplets. The notations d, d_d and d_{md} represent the diameter (0.3 mm) of microchannel, diameter of the primary droplet, and diameter of the secondary droplet, respectively. Steps 1–7 in the image (c) schematically show the various stages of droplet ejection from a single droplet mimicking electrospraying.

Herein we experimentally demonstrate some of the exciting features of the DC electric field induced deformation of microdroplets followed by breakup inside a straight microchannel. We also perform computational fluid dynamic simulations to gain insight on the physics associated with these phenomena. The study revealed that a water droplet

flowing inside a continuous oil medium could spontaneously form a plug, disintegrate into a pair of charged droplets, twin-droplets undergoing periodic coalescence and breakup, a Taylor-cone profusely spraying a string of miniaturized droplets when the intensity of the external field was systematically varied, as shown in the form of schematics in Figure 4.1. Following the proposed pathway, experiments uncovered situations where ~20 times miniaturization was possible inside a straight microchannel. In such, situations, we also show the possibility of forming oil-water microemulsion inside the microchannel. The results reported can be of significance in the development of droplet microfluidic devices targeted for the applications such as emulsification, reaction engineering, and flow cytometry, among others.

Table 4.1: Physical properties of the working fluids.

Properties	Experimental		Computation	
	Water	Silicone oil	Water	Silicone oil
Density (kg/m^3)	997	970	1000	1000
Viscosity (Pa s)	0.001	0.34	0.001	0.01
Dielectric constant	80	2.2	80	2.2
Conductivity (S/m)	0.0069	0.8×10^{-12}, ref[1]	10^{-4}	10^{-6}

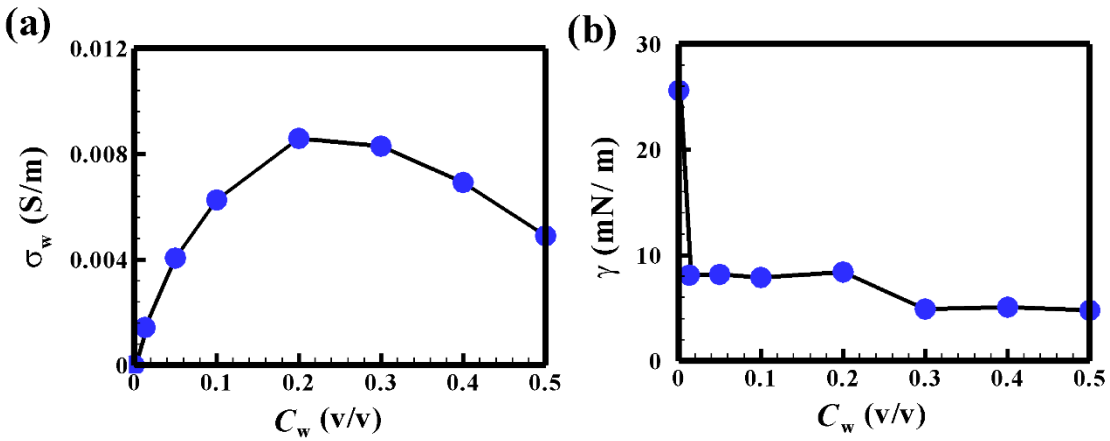

Figure 4.2: Variations in (a) electrical conductivity (σ_w, S/m) of water and (b) interfacial tension (γ, mN/m) at the oil-water interface with the concentration of Tween-20 (C_w, v/v).

4.2 MATERIALS AND METHODS

4.2.1 Materials

Silicone oil (Merck, 330 – 380 cS, 25 °C) and deionized (DI) water (Merck Millipore, grade-I) were used as working fluids. The necessary physical properties of the liquids used in the experiments at room temperature are shown in Table 4.1. A non-ionic surfactant Tween-20 (T-20) was added to water at various concentrations, C_w (v/v), in order to vary the oil-water interfacial tension (γ). The variation of conductivity of water phase (σ_w) in S/m and γ in mN/m with change in surfactant concentration are shown in Figure 4.2(a) and 4.2(b). The interfacial tensions were measured by a digital tensiometer (Krüss) employing a standard du Noüy ring (Pt/Ir) method following the American Society for Testing and Materials (ASTM) Standard Test Method D1331-11 (2001).

4.2.2 Experimental methodology

Figure 4.1 shows the schematics of a T-junction circular microfluidic channel of inner diameter, d = 300 μm and length, l = 30.3 mm which was fabricated using polydimethylsiloxane or PDMS (Dow Corning, Sylgard 184) employing simple microwire molding technique.[2,3] Aluminium sheets of length 2 mm and thickness 0.5 mm were embedded inside the PDMS matrix around the microchannels as electrodes. The cleaning of the microchannel was initiated with ultra-sonication in acetone and methanol baths for 10 minutes. Following this, the channel was treated with 10% (v/v) dilute piranha solution (H_2SO_4:H_2O_2, 3:1) for 15 minutes. The microchannel was then repeatedly washed with DI water for 5 minutes. The microchannel was dried initially by blowing nitrogen gas and then in an air-oven for 20 minutes at 70 °C.

A direct current (DC) power source (SES Instruments Pvt. Ltd, EHT-II) was employed to generate the external electric field through the electrodes by applying a potential in the range of, V = 0 – 1500 V. Syringe pump (Harvard Apparatus, PHD 2000) was used to infuse the fluid phases inside the microchannel at a controlled flow rate. The flow connections from pump to the microchannel were accomplished using silicone tubes (Cole Parmer, 1/16 inch) and micropipette tips (Tarson, 0.2 – 10 μL).

The schematic diagram of the experimental setup is shown in Figure 4.1(a) also shows the connections between the pumping unit and T-junction microchannel alongside the position of the recording unit. The electrodes were placed at a distance of 2 mm from the T-junction to allow the formation of developed flow-patterns such as the droplets. Since we experimented on the EHD field, the electrodes did not make any contact with the fluids and maintained an average distance of 410 μm between them, which ensured that the electrodes were ~ 55 μm away from the walls of the microchannel. This guaranteed the absence of electric current flowing across the microchannel and avoided Joule heating. The distance between electrode and channel wall was maintained by placing a thin plastic sheet near the copper wire during placement of electrode. Initially, the silicone oil was allowed to flow through the horizontal inlet and the microchannel was filled up with the oil medium. This was followed by the infusion of water phase (C_w = 0.4, v/v)) through the vertical inlet. After ~10 minutes, when the oil-water pressure driven flow reached the steady state, the flow features for complete three cycles were recorded using a moderately high speed camera (Basler, piA640-210gc) at 210 frames per second (fps). The faster features in the fluid flow were captured by another high speed camera (Photron, Fastcam Mini UX-100) at 2000 fps. The electric field was turned ON after recording the pressure

driven oil-water flow features and the field driven flow morphologies for complete three cycles were again recorded at various applied voltage.

4.3 PROBLEM FORMULATION

4.3.1 Governing equations

The flow of a pair of incompressible, immiscible, and Newtonian fluids flowing inside a channel induced by externally applied DC electrostatic field was assumed to be governed by the following continuity and equations of motion,

$$\nabla \cdot \mathbf{u}_i = 0 \tag{4.3.1}$$

$$\rho\left(\dot{\mathbf{u}}_i + \mathbf{u}_i \cdot \nabla \mathbf{u}_i\right) = -\nabla p_i + \nabla \cdot \left(\mu_i \left(\nabla \mathbf{u}_i + \nabla \mathbf{u}_i^{\,T}\right)\right) + \nabla \cdot \mathbf{M}_i + \mathbf{f}_{st} + \rho \mathbf{g} \tag{4.3.2}$$

In absence of magnetic field, the irrotational ($\nabla \times \boldsymbol{\psi}_i = 0$) electric field ($\boldsymbol{\psi}_i$) generated across the channel was expressed in terms of the electric field potential (V_i) as, $\boldsymbol{\psi}_i = -\nabla V_i$. Replacing these expressions in the Gauss's law [$\nabla \cdot \left(\sigma_i \boldsymbol{\psi}_i\right) = 0$] led to the Laplace equation, $\nabla^2 V_i = 0$. For leaky dielectric fluids, the electrostatic force acting on the i^{th} fluid was estimated from the divergence of the Maxwell's stress tensor ($\mathbf{M}$) as,

$$\nabla \cdot \mathbf{M}_i = -\frac{1}{2}\varepsilon_0 \boldsymbol{\psi}_i^{\,2} \nabla \varepsilon + q \boldsymbol{\psi}_i \tag{4.3.3}$$

where, $\mathbf{M}_i = \varepsilon_0 \varepsilon_i \left[\boldsymbol{\psi}_i \otimes \boldsymbol{\psi}_i - 0.5\left(\boldsymbol{\psi}_i \cdot \boldsymbol{\psi}_i\right)\mathbf{I}\right]$, ε_0 was the permittivity of the free space and, $\nabla\varepsilon$ and σ were the gradient of permittivity and relative conductivity of the phases across the interface. The charge density, $q = \nabla \cdot \left(\varepsilon_0 \varepsilon \boldsymbol{\psi}_i\right)$, was expressed as, $q = \varepsilon_0 \left(\sigma \boldsymbol{\psi}_i\right) \cdot \nabla\left(\varepsilon / \sigma\right)$. We employed phase field computational method to track the interface.[4-9] The transport equation for the phase field parameter (ϕ) was expressed as, $\dot{\phi} + \mathbf{u}_i \cdot \nabla \phi = \nabla \cdot \chi\left(\nabla G\right)$. The parameter ϕ assumed -1 in water and +1 in oil and G is

the chemical potential. The variable χ captured the mobility of the interface, which was chosen to be 1 m s/kg to avoid mass loss in the conventional phase field model. The chemical potential, $G = F'(\phi) = \lambda\left[-\nabla^2\phi + \phi\left(\phi^2 - 1\right)/N^2\right]$, could be evaluated in terms of the free energy functional, $F(\phi)$, where,

$$F(\phi) = \int_{\Omega} f_{tot}\, d\Omega = \int_{\Omega}\left(f(\phi) + \frac{1}{2}\lambda\left|\nabla^2\phi\right|\right) d\Omega \tag{4.3.4}$$

In Eq. (4.3.4), Ω is the computational volume and the total free energy, f_{tot} is the total free energy density, which is the sum of bulk energy, $f(\phi) = \lambda/4N^2\left(\phi^2 - 1\right)^2$, and the interfacial energy. The parameter N is estimated by, $N = 0.5h_m$ where h_m is the maximum element size in the computational domain. The mixing energy density could be expressed as, $\lambda = \left(3\gamma N\right)/\left(2\sqrt{2}\right)$, in which γ is the interfacial tension. The density (ρ), viscosity (μ), permittivity (ε), and conductivity (σ) at the interface were evaluated as, $a = 0.5\left[a_1(1+\phi) + a_2(1-\phi)\right]$, where a can be any of the physical properties. For example, permittivity (ε) at the interface was calculated as, $\varepsilon = 0.5\left[\varepsilon_1(1+\phi) + \varepsilon_2(1-\phi)\right]$, which was a part of the divergence of the Maxwell's stress tensor in Eq. (4.3.3). Including ε as a function of ϕ ensures that the change in the Maxwell stress at the interface was taken care of while solving the governing equations along with the boundary conditions mentioned in the next sub-section.

4.3.2 Boundary conditions

Figure 4.1(b) shows the two-dimensional (2-D) microchannel of diameter, d = 300 μm and length, l = 2.0 mm. The electrodes of 1 mm length were placed at 500 μm downstream

from the oil inlet to produce electrostatic field. The physical and the flow properties employed in the simulations were nearly identical to the experimental one as can be identified in the Table 4.1. However, the comparison was rather qualitative because the viscosity and conductivity difference between water and oil was set much lower in the computations than in the experiments. This was done to avoid the stiffness in the discretized governing equations and boundary conditions while computationally solving a two-phase flow with a very large viscosity difference. The lower viscosity difference between the phases in the computations could be justified from the experimental results of Garstecki et al.[10] and computational results of Raj et al.[11], which showed the change in the flow computational and experimental flow morphologies was minimal beyond a threshold difference in viscosity between the phases. Also, the conductivity of oil and water was also set much lower than in experiments in order to avoid divergence.[12] This could be justified from the study of Feng and Scott[13] which suggest that the droplet behavior would be unaffected when the conductivity of one fluid is more than the other by an order of 100 or more. Most importantly, we chose the parameters in such a manner that the electric field Bond number ($Bo_e = \varepsilon_0 \varepsilon_c r_d \psi^2 / \gamma$) representing the ratio of the electric field force to surface tension force for the theoretical and experimental were nearly same. Here the notations ε_0, ε_c, r_d, ψ, and γ, represent the permittivity of free space, permittivity of the continuous oil phase, radius of the droplet, applied electric field intensity, and interfacial tension, respectively. Grid independent solutions were obtained when ~16800 triangular elements were placed in the computational domain. COMSOL™ multiphysics software was employed to solve the unsteady governing equations along with the aforementioned boundary conditions. This software uses the Galerkin least-square finite element method to discretize the convective diffusion equations. The numerical stability was obtained after

employing the streamline and crosswind diffusions alongside the use of the second order elements for velocity and first order elements for pressure gradient calculations. The velocity and pressure profiles for the entire domain were evaluated by the segregated predictor-corrector method with incremental pressure correction. A second-order backward difference method employing the Euler scheme with an optimum time step ~10^{-4} s was used for consistent initialization, time-marching, control of error, and convergence.

4.4 RESULTS AND DISCUSSIONS

The electric field induced deformation of a water droplet suspended in a continuous oil medium is stimulated by the additional EHD stresses at the oil-water interface originating from to the accumulations of, (a) induced charges across the interface owing to the dielectric contrast ($\varepsilon_r = \varepsilon_w/\varepsilon_c$) and (b) free charges owing to the difference in the electrical conductivities ($\sigma_r = \sigma_w/\sigma_c$) of the liquid mediums. The subscripts *w* and *c* here represent disperse (water) and continuous (oil) phases, respectively. The presence of the electric field introduces an additional Maxwell's stresses along the interface, which facilitates the small and large deformations. The components capillary forces at the interface aid as well as oppose the deformation depending upon the sign of the radius of curvature of the interface. The kinetic factors such as the shear force across the interface originating from the ratios of the dynamic viscosities ($\mu_r = \mu_w/\mu_c$) and average inlet flow velocities ($Q_r = U_w/U_c$) of the fluids also play crucial roles in deforming a droplet. The interplay between the surface tension, Maxwell's stresses, inertial forces, and viscous stresses decides the final shape of droplet.

The deformation of the droplet (D) could be analytically evaluated from leaky dielectric model (LDM) theory of Taylor[14] as, $D=(L-B)/(L+B)=0.56Bo_e f_d(\sigma_r,\varepsilon_r,\mu_r)/(2+\sigma_r)^2$, where the notations L and B represent the length and breadth of the deformed droplet. The theory suggests that the shape of the droplet could also be a function of the parameters, $f_d=\sigma_r^2+1-2\varepsilon_r+0.6(\sigma_r-\varepsilon_r)(2+3\mu_r)/(1+\mu_r)$. In particular, the LDM theory suggests that a droplet can easily deform into a prolate (D > 0) or oblate (D < 0) shape with the variations in ψ, γ, ε_r, and σ_r, under the influence of an external electric field.[7] Importantly, most of the previous theoretical and experimental studies[15,16] on the macroscopic systems have suggested that an external electric field can not only deform the dispersed water droplets inside continuous oil phase but also can break it into smaller parts especially at higher field intensities. In what follows, we discuss the electric field induced deformation and breakup of droplets inside simple microchannels.

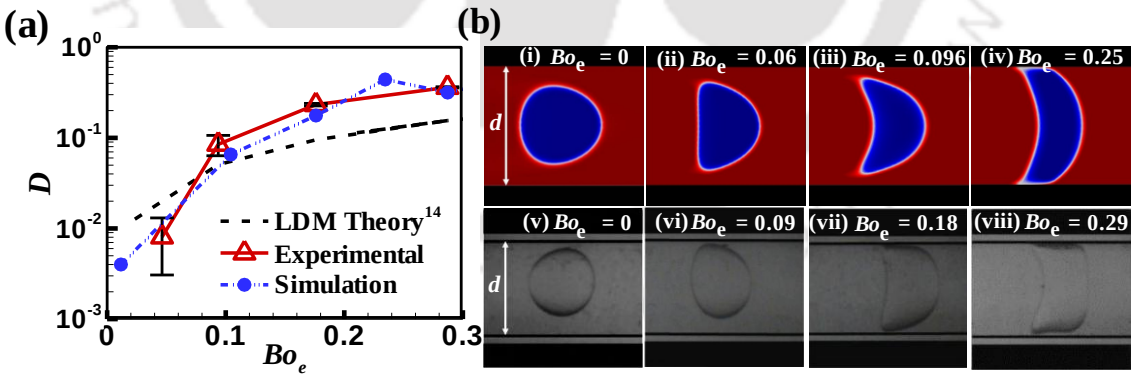

Figure 4.3: Deformation, D, of a droplet in oil due to externally applied electric field inside a microchannel of d = 300 μm. Image (a) shows the variation in D at various Bo_e in the experiments, leaky dielectric model (LDM) theory, and numerical simulations. Images (i – iv) in the row (b) show the shapes of water droplet (d_d = 190 μm) at different Bo_e obtained from the computational simulations. While, images (v – viii) show the shapes of water droplets (d_d = 214 μm) in the experiments at different Bo_e. The flow parameters for

simulations were set as, U_c = 0.1 m/s, U_w = 0 m/s, γ = 15 mN/m, ε_r = 36.4, and σ_r = 100. The flow parameters for experiments were U_c = 0.445 mm/s, U_w = 0.062 mm/s, γ = 5.1 mN/m, ε_r = 36.4, and $\sigma_r = 8.63 \times 10^9$. The dimensionless numbers are mentioned in Table A.1 of **Appendix – A**.

4.4.1 Droplet deformation under electric field

Figure 4.3 shows the regimes of electric field induced drop deformation inside microchannels. Figure 4.3 show the D obtained from LDM in the simulations, and experiments. The images (i – iv) and images (v – viii) in Figure 4.3(b) show the simulated and experimental flow morphologies when a water droplet was passed through a microchannel and exposed to the electric field having different values of ψ or in dimensionless form represented by Bo_e. The image (v) in Figure 4.3(b) show the motion of a water droplet inside a microfluidic channel filled with oil in absence of the electric field. The process parameters such as ratio of velocity of water and oil phase, Q_r = 0.14 and γ = 5.1 mN/m, were fixed in such a manner that spherical water droplets were formed inside the microchannel and the electro-coalescence was avoided by tuning the droplet frequency. These parameters were kept unchanged in the entire study unless mentioned otherwise. As mentioned previously, that the electrodes maintained a distance of, l_w = 55 μm, which required a correction factor[12] of, $\psi = V / \left(2l_w\left(\varepsilon_c / \varepsilon_p\right) + d\right)$, while reporting the experimental electric field intensities where, V, d, ε_c and ε_p represent the applied voltage, diameter of the microchannel, and the dielectric constants for oil and PDMS, respectively. Here, the effect of electric field intensity, ψ, is shown by the dimensionless variable Bo_e and the effects of velocity, density, viscosity of fluids, interfacial tension and diameter of microchannel have been incorporated in dimensionless forms as Reynolds (Re_w), Weber (We_w), Capillary (Ca_w) and Bond (Bo) numbers, as shown in Table A.1 of **Appendix – A**.

On applying an electric field of lower intensity, ψ = 0.47 MV/m and Bo_e = 0.09, the induced charge polarization at the interface led to a marginal deformation on the droplet towards the upper electrode, as shown in the image (vi) of Figure 4.3(b). With further increase in ψ to 0.65 MV/m and Bo_e = 0.18, the droplet elongated more in the vertical direction to touch the wall of the channel and formed a 'D' shaped plug flow pattern, as shown in the image (vii) of Figure 4.3(b). For ψ = 0.83 MV/m and Bo_e = 0.29, the droplet deformed into a complete plug flow pattern, as shown in the image (viii) of Figure 4.3(b). The simulation images (i) – (iv) in the Figure 4.3(b) shows similar deformation of a leaky dielectric water droplet inside a continuous oil phase with the variation in the ψ or Bo_e. Figure 4.3 shows that, in case of the magnitude of deformation, *D*, the computational and experimental results followed the linear trend predicted by the LDM theory until Bo_e < 0.1. For Bo_e > 0.1, since the shape of droplet became more complex than simple prolate or oblate due to the combined effect of Maxwell's stresses and the hydrodynamic force, the experimental and computational results deviated significantly from the predictions of LDM theory. However, in such a scenario, the deformation measured from the results of experiments and simulation agreed well with each other.

4.4.2 Droplet splitting due to applied electric field

Interestingly, increasing ψ to 0.55 MV/m led to the splitting of the primary droplet into three secondary droplets, as shown in the images (i) – (iv) in the Figure 4.4(a). The simulations images for the similar system are shown in the images (i) – (vi) in the Figure 4.4(b). Both the experimental and simulation images suggest that beyond critical field intensity the electrical stress at the interface combined with the destabilizing component of the capillary force could break the primary droplet into three parts in which a pair of

secondary droplets resided near the boundary while the other one streamed out with oil through the center part of the channel.

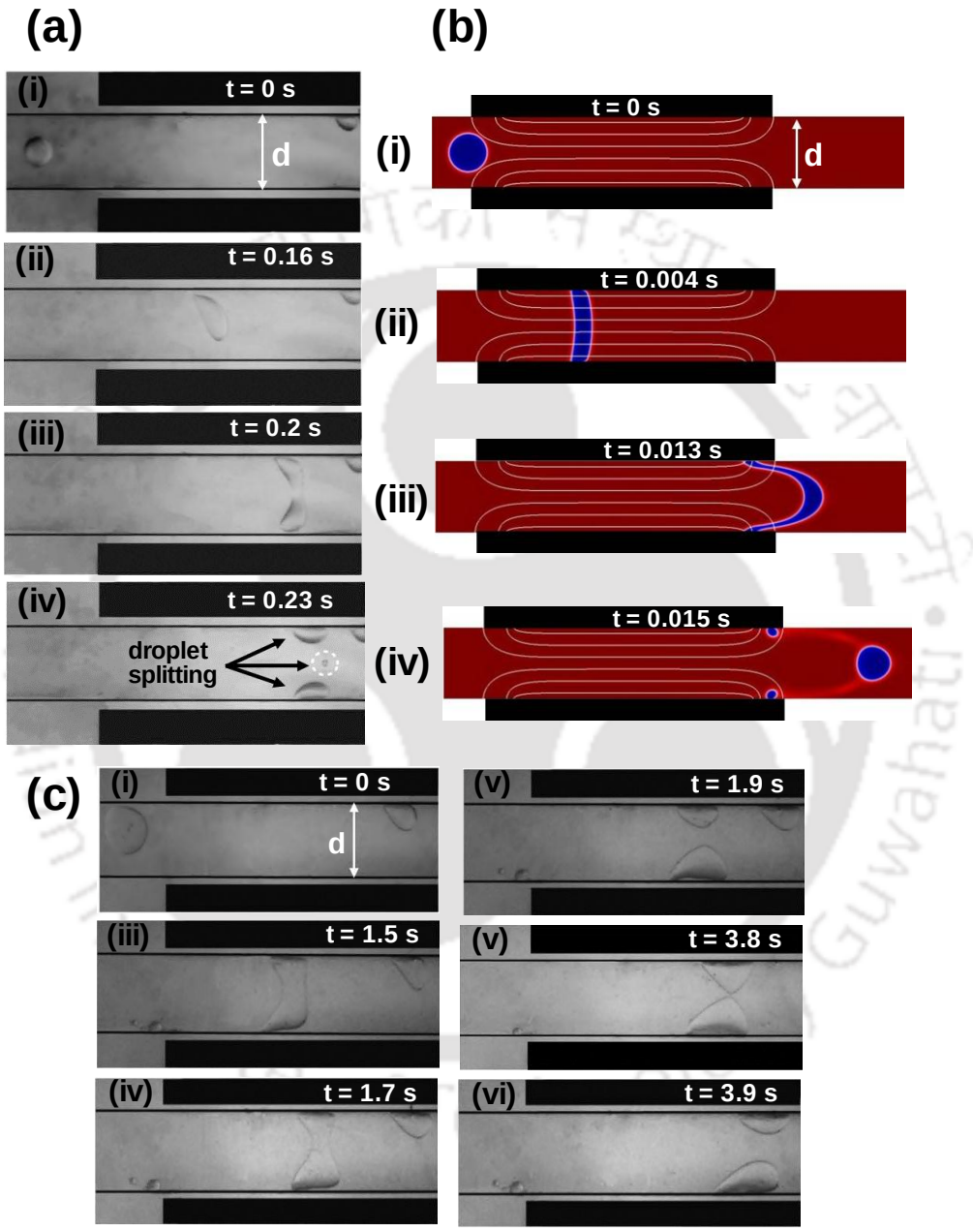

Figure 4.4: (a) Experiments showing a primary droplet (d_d = 125 μm) splitting into secondary droplets at different time (t) interval at ψ = 0.55 MV/m. Image (i) shows that a droplet approaches to the zone of applied field, (ii) shows the initiation of droplet deforming, (iii) shows the formation of a 'neck', (iv) shows the splitting of primary droplet into three secondary droplets indicated by the arrows. Here, d = 300 μm, U_c = 2

mm/s, U_w = 0.22 mm/s, γ = 5 mN/m, ε_r = 36.4, and $\sigma_r = 1.04 \times 10^{10}$. The images in (b) shows the results obtained from numerical simulations when (d_d = 157 μm, U_c = 0.1 m/s, U_w = 0 m/s, γ = 15 mN/m, ε_r = 36.4, and σ_r = 100. The images (i) – (vi) in (c) shows the splitting of a droplet (d_d = 214 μm) followed by periodic bridging and breaking of charged secondary droplets when ψ = 1.16 MV/m. Here, U_c = 0.445 mm/s, U_w = 0.062 mm/s, γ = 5.1 mN/m, ε_r = 36.4, and $\sigma_r = 8.63 \times 10^9$. The corresponding dimensionless numbers are shown in Table A.1 of **Appendix – A**.

The results from the simulations and experiments clearly suggested that once the elongated droplet entered the domain of the electric field exposure and created the water plug, the parts near the boundary moved at a much slower pace while the central part moved much faster. Subsequently, as the plug progressed downstream of the channel, it formed further to have a convex front and concave rear. Eventually, the parts of the plug near wall pinched off from the parent body undergoing the Rayleigh-Plateau instability to form the secondary droplets.[17,18] A pair of secondary droplets were found to be more firmly attached to the channel wall because, (i) the flow in that region was much weaker and (ii) they experienced an attractive force towards the electrodes by assuming induced charge of opposing polarity at the interface to that of the electrode. The experiments showed a facile way of creating a pair of droplets with opposite charge inside a straight microchannel, which was quite unlike the previously reported ones where the charged droplets could only be achieved in a bifurcated channel with complex electrode arrangements.[17,19]

Increasing the field intensity ψ to 1.16 MV/m, we observed another interesting phenomenon apart from the droplet splitting, as shown in the images (i) – (vi) in the Figure 4.4(c). In this situation, the droplet initially elongated as it approached the area exposed to the electric field before splitting into secondary droplets. Thereafter, similar to

the previous case, the pair of the secondary droplets stayed near the electrodes while moving downstream of the channels. Strikingly, when the droplets moved towards downstream transient bridges were created between them due to the attractive electrostatic force originating from the opposing induced charges at the droplet interfaces. However, the bridges were broken immediately after the formation undergoing Rayleigh-Plateau instability because of the sharp curvature near the bridging zone. Formation of the bridges and their breaking up took place periodically as the pair of the charged secondary droplets translated out of the domain of electric field exposure. The phenomenon reported here had similar origin as some of the recently reported works where, (i) a water droplet was found to bounce on an oil-water interface[20] and (ii) a pair of droplet show repeated bridge formation and subsequent break up[21] when the exposure of external EHD field was of very high intensity. Another recently reported work[22] showed that a water droplet underwent periodic deformation from a spherical to prolate and then to form a water plug touching walls of a macroscopic channel before retreating back to the spherical shape under the influence of a low intensity AC field. The study further showed that, at higher AC field intensities, there was periodic breaking of the water droplet into pair of droplets followed by coalescence of the droplets into a single droplet with time.

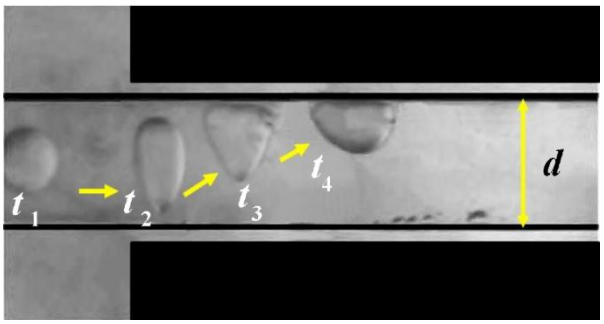

Figure 4.5: The migration of a flowing droplet (d_d = 125 μm) towards the electrode at different time (t) when ψ = 0.711 MV/m. Here, d = 0.3 mm, t_1 = 0 s, t_2 = 0.06 s, t_3 = 0.09

s, and t_4 = 0.13 s, respectively. The other parameters were, d = 300 μm, U_c = 2 mm/s, U_w = 0.22 mm/s, γ = 5 mN/m, ε_r = 36.4, and $\sigma_r = 1.04 \times 10^{10}$. The corresponding dimensionless numbers are shown in Table A.1 of **Appendix – A**.

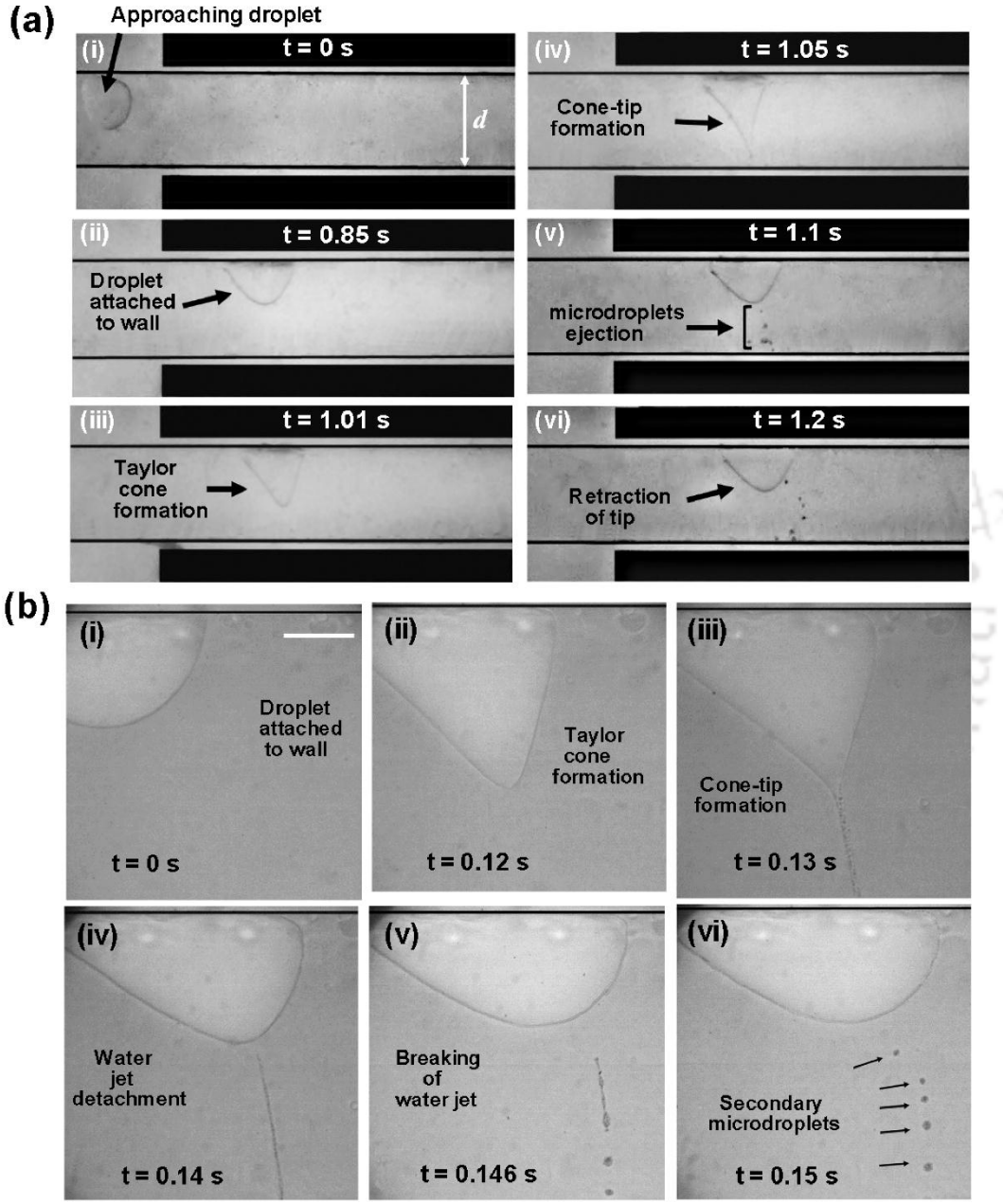

Figure 4.6: Ejection of a string of droplets from a translating primary droplet (d_d = 214 μm) at time (t) when ψ = 1.2 MV/m. Here, d = 300 μm, U_c = 0.445 mm/s, U_w = 0.062 mm/s, γ = 5.1 mN/m, ε_r = 36.4, and $\sigma_r = 8.63 \times 10^9$. The images in (a) shows the mechanism of droplet ejection recorded at 211 fps with a 5X objective. The images in (b)

show the microscopic view of similar droplets ejection mechanism recorded at 2000 fps at ψ = 3.56 MV/m with a 50X objective. The scale bar at the top of image b(i) represents length of 50 μm.

4.4.3 Spraying of microdroplets

It may be noted here that at moderately high ψ ~ 0.711 MV/m the droplet started showing a dielectrophoretic (DEP) migration towards the wall nearer to anode as it entered the region of the electric field exposure. Figure 4.5 shows a typical track of the droplet migration at different intervals of time, which is superimposed in a single image. Increasing ψ further to 1.19 – 3.56 MV/m we observed another interesting phenomenon, which is shown in the images (i) – (vi) in the Figure 4.6. Images (vii) – (xii) in the Figure 4.6 show the high speed images of a microscopic view of the same phenomenon. The images and the movies suggest that as the droplet approached the area of high intensity EHD field it underwent a DEP migration[23] towards the anode [image (i)]. Accumulation of opposing induced charges around the oil-water interface facilitated the migration of the droplet towards the anode [image (ii)]. Further, as the charged droplet migrated further downstream, it experienced a strong attractive force from the cathode to deform into a shape similar to the Taylor cone [image (iii)]. However, the Taylor cone formed was rather asymmetric because of the migration of the droplet with the annular oil flow. Importantly, the attractive force on the cone increased as the tip of the cone grew closer towards the cathode to form a cone-jet structure [image (iv)]. With progress in time the cone-jet elongated and then broke down to form a string of miniaturized water droplets undergoing Rayleigh-Plateau instability [images (iv – vi)]. Ejection of secondary microdroplets was also accompanied by the recoil of the primary droplet owing to the effects of the restoring surface tension force. When the external field intensity was kept

constant, ejection of secondary microdroplets and recoil of the Taylor cone kept occurring periodically until the primary droplet went out of the zone of the electric field exposure. Further, the frequency of the microdroplet ejection from the Taylor cone was found to increase with the EHD field intensity.

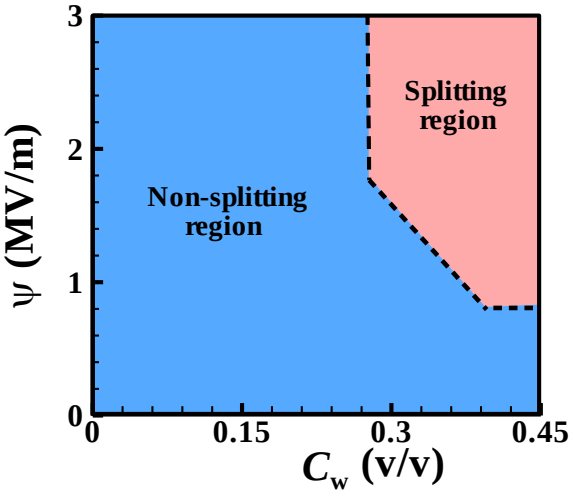

Figure 4.7: Contour plot of C_w vs ψ showing the regions of droplet splitting and non-splitting.

The reported phenomena was found to be quite similar to electrospraying[1,24] in which a fluid ejecting out of a nozzle electrode initially forms a Taylor cone under the influence of an external electric field of high intensity, which later elongates into a jet before breaking down into droplets. However, we showed a similar effect inside a simple microfluidic device, which could be utilized for systematic breakdown of a bigger droplet into the miniaturized ones with significantly higher surface to volume ratio. It may be noted here the reported electrospraying of a sessile droplet inside a microchannel is yet to be reported in the literature. It can easily be envisaged that, similar to electrospraying, formation of nanodroplets is also a possibility employing the proposed methodology. Indeed the flow structures originating from the present methodology could be expected to be much smaller with reduction in the magnitude of stabilizing interfacial tension. The ψ vs C_w plot in

Figure 4.7 shows the regions at which the droplet undergoes splitting. It shows that the droplet undergo splitting at $C_w \geq 0.3$ after critical value of ψ. Also, the role of oil flow rate in the droplet splitting process is to (i) provide hydrodynamic pressure to the EHD induced elongated droplet leading to Rayleigh-Plateau instability due to which the droplet splitting takes place, (ii) developed emulsions through continuous ejection of flowing droplet, and (iii) capture the splitting phenomena in its pristine state.

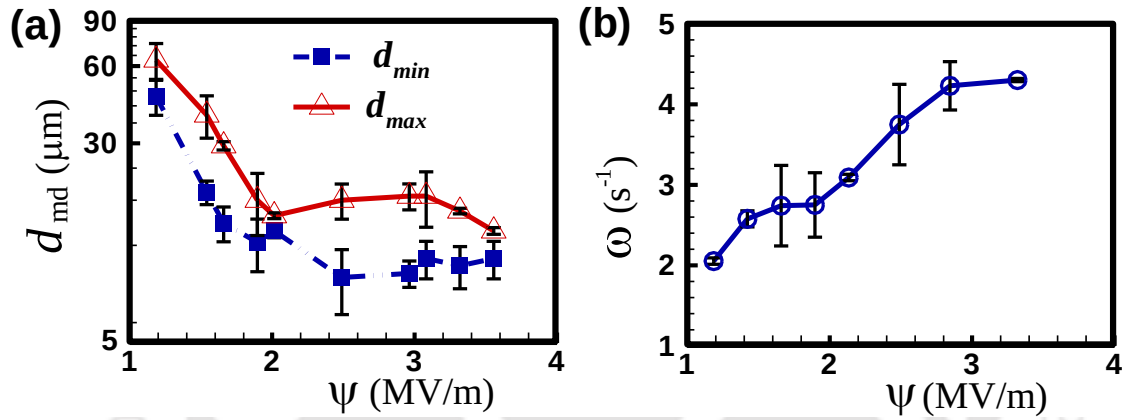

Figure 4.8: Effect of electric field intensity, ψ, on the secondary microdroplets ejected from the primary droplet. Plot (a) shows the variations in diameters (minimum - d_{min}, and maximum - d_{max}) of microdroplets (d_{md}) ejected from the primary droplet at different ψ. Plot (b) represents the variation of frequency of droplet ejection, ω, with ψ.

In Figure 4.8, plots (a) show variations in the diameters (d_{md}, minimum - d_{min}, and maximum - d_{max}) of the secondary droplets ejected from the primary droplet with ψ while plot (b) shows tithe frequency of droplet ejection, ω, with ψ. Figure 4.8(a) shows that d_{md} decreases monotonically with increase in ψ before reaching a constant value. The plot also suggests that at lower field intensities the difference in the minimum to maximum droplet size was much higher. In contrast, at higher field intensities ($> \psi = 2$ MV/m), a 214 μm droplet was broken down to a near monodisperse collection of droplets with minimum (maximum) diameter of 10 (18) μm. The diameter of the secondary microdroplets is

influence by two factors, i.e. (i) electric field intensity, and (ii) interfacial tension. The increase in electric field intensity increases the destabilizing forces which increased the stretch over the water jet ejected from the Taylor cone and reduces the diameter of the microdroplets which can be seen in Figure 4.8(a). While interfacial tension decides the minimum diameter of the droplets formed from a liquid jet undergoing Rayleigh-Plateau instability. Since the interfacial tension of the oil-water system was fixed at 5.1 mN/m, the diameter of the secondary microdroplets did not vary significantly after a certain value of ψ (~ 2 MV/m). Figure 4.8(b) suggests that these miniaturized droplets could be formed at a much faster rate (high ω) at a higher ψ. The plots show a simple but effective strategy to produce miniaturized flow patterns from a single water droplet having higher surface to volume ratio, and nearly uniform size distribution inside a simple microfluidic system with the help of an external EHD field.

4.5 SUMMARY

The study in the present chapter uncovers the behavior of a water droplet flowing inside an oil medium and exposed to an external EHD field inside a microchannel. The important conclusions are:

(i) When the external field intensity was weak, both experiments and simulations showed similar shape in deformation of the droplet at different electric field intensities. The deformation trends predicted from LDM analytical theory was found to match with the experimental and simulated results at only low field intensities (Bo_e < 0.1). In contrast, the experimental and simulated deformations were found to be comparable up to moderately high field intensities.

(ii) At moderately high electric field intensities, the droplet could be split into a pair of charged droplets, which underwent periodic bridging and breakup as they translated

out of the domain with electric field exposure. While the electrostatic attraction between the charged droplets led to the bridging, the capillary instability at the bridging point with sharp curvature caused the breakup.

(iii) At higher field intensities, we observed a unique phenomenon of secondary droplet ejection from the primary droplet, mimicking the electrospraying process. A droplet of 214 μm was broken down to a nearly monodisperse collection of droplets with minimum (maximum) diameter of 10 (18) μm forming water in oil microemulsion near the cathode region when the field intensity was significantly high. Reduction in droplet size was also observed by tuning the external field intensity. There is a possibility that the experiments reported here could indeed produce nanoscopic flow patterns, which is kept as a future scope of research work.

Concisely, a non-invasive pathway was invented to transform a water microdroplet into a string of miniaturized ones only by tuning the external field intensity across a simple microchannel. The results can be of significance in the development of droplet microfluidic devices targeted for the applications such as microscale emulsifiers, reactors, and flow cytometers, among others.

4.6 ACKNOWLEDGMENTS

We acknowledge the funding support of this work from DST, SERB, Grant no. SR/S3/CE/0079/2010, DEITY grant no. 5(9)/2012-NANO, and DST FIST grant no. SR/FST/ETII-028/2010, Government of India, for the financial aids. Supports from Mr. Joydip Chaudhuri is gratefully acknowledged.

4.7 REFERENCES

1. S. Mhatre and R. Thaokar, Industrial & Engineering Chemistry Research **53**, 13488 (2014).
2. M. K. S. Verma, A. Majumder, and A. Ghatak, Langmuir **22**, 10291 (2006).
3. Y. Jia, J. Jiang, X. Ma, Y. Li, H. Huang, K. Cai, S. Cai, and Y. Wu, Chinese Science Bulletin **53**, 3928 (2008).
4. D. M. Anderson, G. B. McFadden, and A. A. Wheeler, Annual Review of Fluid Mechanics **30**, 139 (1998).
5. D. Jacqmin, Journal of Computational Physics **155**, 96 (1999).
6. V. E. Badalassi, H. D. Ceniceros, and S. Banerjee, Journal of Computational Physics **190**, 371 (2003).
7. Y. Lin, P. Skjetne, and A. Carlson, International Journal of Multiphase Flow **45**, 1 (2012).
8. M. Plapp, Philosophical Magazine **91**, 25 (2010).
9. I. Steinbach, L. Zhang, and M. Plapp, Acta Materialia **60**, 2689 (2012).
10. P. Garstecki, M. J. Fuerstman, H. A. Stone, and G. M. Whitesides, Lab on a Chip **6**, 437 (2006).
11. R. Raj, N. Mathur, and V. V. Buwa, Industrial & Engineering Chemistry Research **49**, 10606 (2010).
12. J. D. Wehking, L. Chew, and R. Kumar, Applied Physics Letters **103**, 054101 (2013).
13. J. Q. Feng and T. C. Scott, Journal of Fluid Mechanics **311**, 289 (1996).
14. G. Taylor, Proceedings of the Royal Society of London A: Mathematical, Physical and Engineering Sciences **291**, 159 (1966).

15. C. G. Garton and Z. Krasucki, Proceedings of the Royal Society of London A: Mathematical, Physical and Engineering Sciences **280**, 211 (1964).
16. S. Torza, R. G. Cox, and S. G. Mason, Philosophical Transactions of the Royal Society of London A: Mathematical, Physical and Engineering Sciences **269**, 295 (1971).
17. H. Zhou and S. Yao, Lab on a Chip **13**, 962 (2013).
18. O. Vizika and D. A. Saville, Journal of Fluid Mechanics **239**, 1 (1992).
19. D. R. Link, E. Grasland-Mongrain, A. Duri, F. Sarrazin, Z. Cheng, G. Cristobal, M. Marquez, and D. A. Weitz, Angewandte Chemie International Edition **45**, 2556 (2006).
20. W. D. Ristenpart, J. C. Bird, A. Belmonte, F. Dollar, and H. A. Stone, Nature **461**, 377 (2009).
21. J. C. Bird, W. D. Ristenpart, A. Belmonte, and H. A. Stone, Physical Review Letters **103**, 164502 (2009).
22. T. Mochizuki, Langmuir **29**, 12879 (2013).
23. S. Dash and S. Mohanty, Electrophoresis **35**, 2656 (2014).
24. O. V. Kim and P. F. Dunn, Langmuir **26**, 15807 (2010).

Chapter 5

Electric field mediated droplet splitting in microchannels

ABSTRACT

In this chapter, numerical simulations supplemented by experiments have uncovered the strategic integration of discrete electric fields in a non-invasive manner which could substantially miniaturize the droplets into smaller parts in a pressure driven oil-water flow inside microchannels. The Maxwell's stress generated from the electric field at the oil-water interface could deform, stretch, neck, pin, and disintegrate a droplet into many miniaturized daughter droplets, which eventually usher a one-step method to form water-in-oil microemulsion employing microchannels. The interplay between electrostatic, inertial, capillary, and viscous forces led to various pathways of droplet breaking, namely, fission, cascade, or Rayleigh modes. While a localized electric field in the fission mode could split a droplet into a number of daughter droplets of smaller size, the cascade or the Rayleigh mode led to the formation of an array of miniaturized droplets when multiple electrodes generating different field intensities were ingeniously assembled around the microchannel. The droplets size and frequency could be tuned by varying the field intensity, channel diameter, electrode locations, interfacial tension, and flow ratio. The proposed methodology shows a simple way to transform a droplet into an array of miniaturized ones inside a straight microchannel for enhanced mass, energy, and momentum transfer, and higher throughput.

This chapter is published in Electrophoresis, **38**, 278 (2017).

5.1 INTRODUCTION

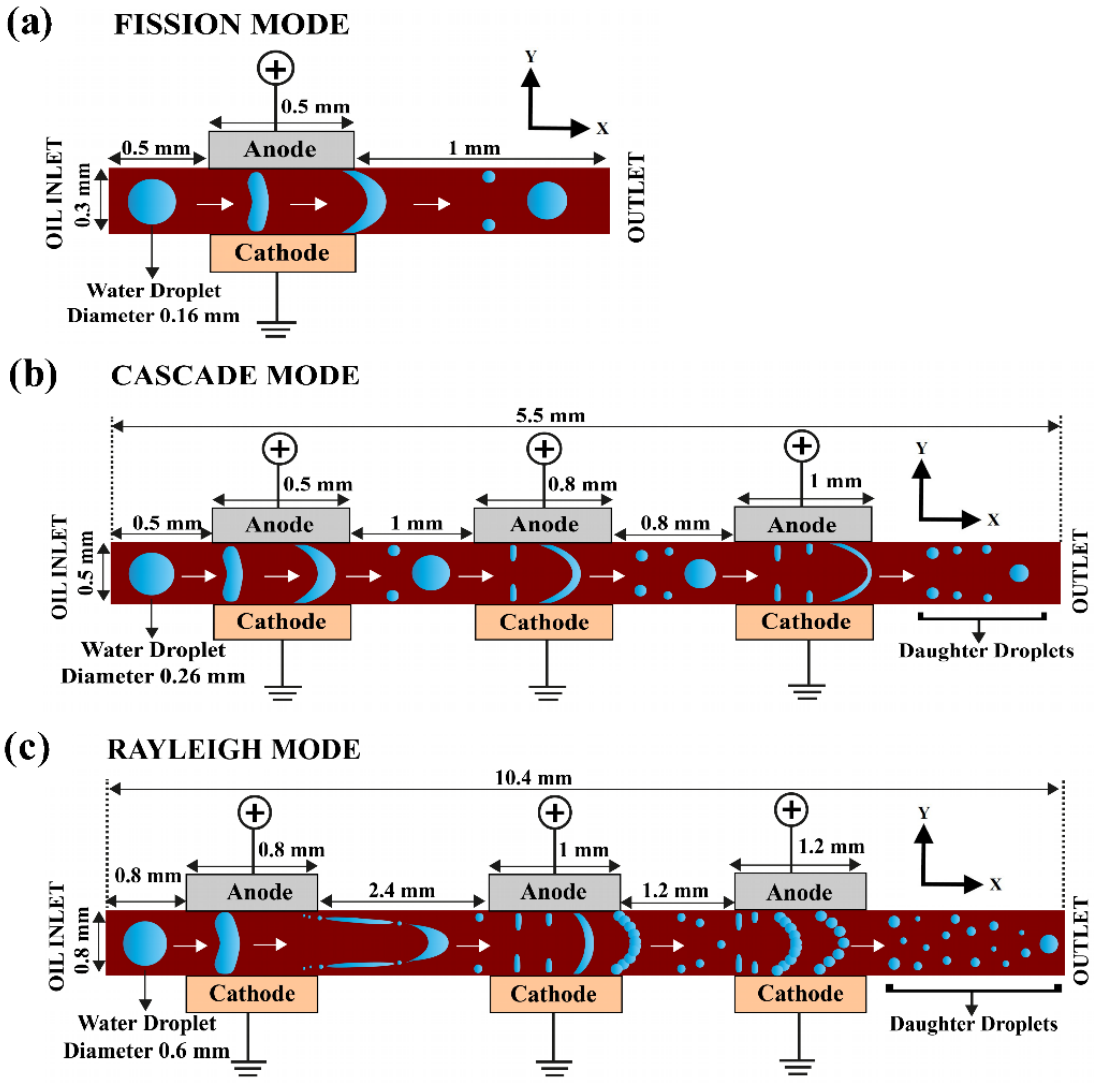

Figure 5.1: Schematic diagrams of the different modes of droplet breaking under an external electrohydrodynamic (EHD) field in a microchannel. (a) 'Fission' mode – electrodes are placed 0.5 mm downstream from inlet with field a field intensity of, ψ_1 = 1.2 MV m^{-1} when the channel diameter (d) is 0.3 mm and initial diameter of the droplet (d_d) is 0.16 mm. (b) 'Cascade' mode – electrodes are placed 0.5 mm, 2 mm, and 3.6 mm downstream from inlet with, ψ_1 = 1.2 MV m^{-1}, ψ_2 = 1.2 MV m^{-1}, and ψ_3 = 1.16 MV m^{-1}, respectively, and d = 0.5 mm and d_d = 0.26 mm. (c) 'Rayleigh' mode – electrodes are placed 0.8 mm, 4 mm, and 6.2 mm downstream from inlet with, $\psi_1 = \psi_2 = \psi_3$ = 1.25 MV m^{-1} and d = 0.8 mm and d_d = 0.6 mm.

In the present study, we explored some ingenious pathways to integrate the electric field into simple microchannels for rapid miniaturization of the droplet patterns. Figure 5.1 schematically shows the different modes that have been identified with the help of computational fluid dynamic simulations and experiments. Figure 5.1(a) shows the 'fission mode' in which a localized DC electric field was generated in the downstream of a simple rectangular microchannel to disintegrate a water droplet into smaller ones inside a continuous oil phase. When the fission mode was repeated for multiple times in the same microchannel, we observed the 'cascade mode', which enabled a systematic to form a large number of uniformly sized water droplets of smaller dimension, as shown in the Figure 5.1(b). Interestingly, for the channels with slightly bigger diameter, repeating the fission mode for multiple times did not always lead to the cascade mode of droplet breaking. Instead, we observed a 'Rayleigh mode' of droplet breaking where a single water droplet briskly broke down into a large collection of smaller droplets, as shown in the Figure 5.1(c). Surprisingly, the simple techniques shown here could rapidly break down a single droplet into forty smaller ones inside a straight microchannel, which was also associated with about thirty times miniaturization in the droplet diameter. The results reported not only suggests an explosive increase in the surface area per unit mass due to the formations of large number of droplets with smaller dimensions but a much higher throughput as the smaller flow patterns migrated past the domain at a much faster rate. The reported non-invasive methodology is expected to improve the efficiency and performance of a number of microfluidic applications through digitization and miniaturization of the flow patterns.

5.2 MATERIALS AND METHODS

5.2.1 Materials

Silicone oil (Merck, 330 – 380 cS, 25 °C) and deionized water (DI, Merck Millipore, grade-I) were the working fluids for the multiphase liquid-liquid immiscible flow. The fluid properties are mentioned in Table 5.1. A non-ionic surfactant tween-20 ($C_{58}H_{114}O_{26}$, 1.1 g/cm^3, Merck India ltd.) was added to water (v/v %) at various concentrations, C_w (ranging from 20 (% v/v) to 50 (% v/v)) to vary the oil-water interfacial tension (γ). A 'T'-junction microchannel with circular cross-section of diameter, d = 0.3 mm, and length, l = 13 mm was fabricated by replica molding of polydimethylsiloxane (PDMS).[1-4] Aluminum plates of dimension 2 mm × 0.5 mm were embedded inside the PDMS channels to fabricate the electrodes. The flow connections to the microchannel were made using silicone tubes (Cole Parmer, inner diameter = 1/16 inch) and microtips (Tarson, 0.2 – 10 µL).

Table 5.1: Fluid properties.

Properties	**Experimental**		**Computation**	
	Water	Oil	Water	Oil
Density (kg m^{-3})	997	970	1000	1000
Viscosity (Pa s)	0.001	0.34	0.001	0.01
Dielectric constant	80	2.2	80	2.2
Conductivity (S m^{-1})	0.0069	0.8×10^{-12} ref[5]	10^{-4}	10^{-6}

5.2.2 Experimental methodology

The experimental setup is schematically shown in Figure 5.2 which consist of a T-junction microchannel integrated with pumping unit, recording unit, electrodes, and a DC power source. The electrodes were integrated with the microchannel at the downstream of 2 mm from the T-junction and they did not make any contact with the fluids inside the channel. The average distance of 0.347 mm between the electrodes ensured that they were ~ 23.5

μm away from the microchannel wall. In this manner, the external field (DC power source, SES Instruments Pvt. Ltd, EHT-ll, V = 0 – 1500 V) around the microchannel only generated EHD stress on the fluid and did not electrolyze them.

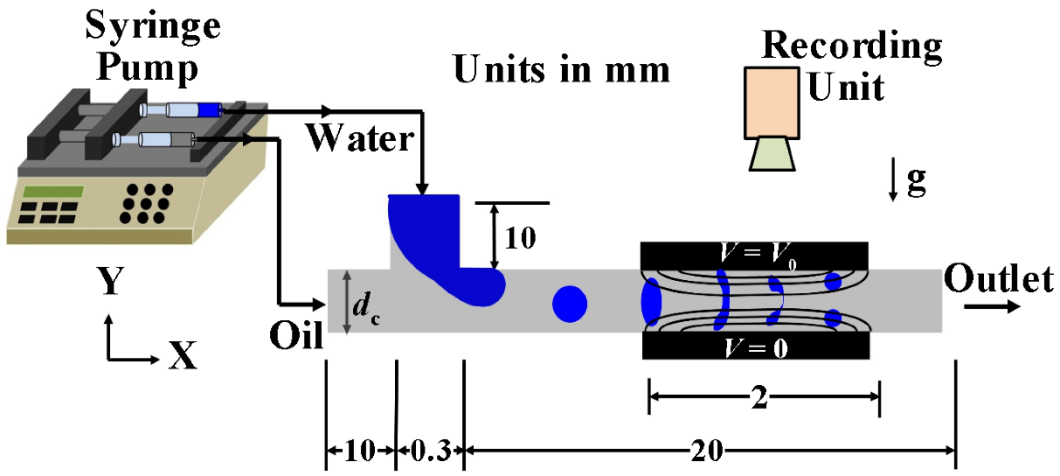

Figure 5.2: Schematics of the experimental setup with dimensions represented in millimeter (mm). Here oil (water) was infused through horizontal (vertical) inlet using a syringe pump and forms the continuous (disperse) phase. While d_c = 0.3 mm and V, represents the diameter of microchannel and applied voltage, respectively.

The microchannels were cleaned before the experiments in the following manner: (i) initially, they were ultra-sonicated in the acetone and methanol baths for 10 min each before treating with 10% (v/v) piranha solution (H_2SO_4:H_2O_2, 3:1) for 15 min; (ii) then, they were repeatedly washed with DI water for 5 min and dried by inert nitrogen gas before keeping in the air-oven for 20 min at 70 °C. Syringe pump (Harvard Apparatus, PHD 2000) forced the fluid phases at controlled flow rate into the microchannel. Initially, the silicone oil was flown through the horizontal port to fully fill the microchannel with oil before the water was infused through the vertical port to obtain the steady flow patterns after ~10 min. The flow features were recorded at 210 frames per second using an imaging unit Basler, piA640-210gc. After characterizing the pressure-driven flow in the

aforementioned method, the EHD field was turned on and the experiments were repeated to capture the flow morphologies. The oil-water interfacial tension (γ) was estimated by a digital tensiometer (Krüss) employing the du Noüy ring (Pt/Ir) method, ASTM - D1331-11 (2001).

5.3 PROBLEM FORMULATION

The oil-water flow was considered to be incompressible, immiscible, and Newtonian inside the microchannel. The Poisson's equation for the EHD field coupled with the continuity equation and Navier-Stokes equations of motion was employed to numerically simulate the experimental observations, as proposed by a few recent studies,[6,7]

$$\nabla \cdot \mathbf{u}_i = 0 \tag{5.3.1}$$

$$\rho\left(\dot{\mathbf{u}}_i + \mathbf{u}_i \cdot \nabla \mathbf{u}_i\right) = -\nabla p_i + \nabla \cdot \left(\mu_i \left(\nabla \mathbf{u}_i + \nabla \mathbf{u}_i^{\,T}\right) + \mathbf{M}_i\right) + \mathbf{f}_{st} + \rho \mathbf{g} \tag{5.3.2}$$

where the subscript '*i*' denotes oil (*i* = 1) or water (*i* = 2) and the over dot denotes the time derivative. The notations $\mathbf{u}_i$, $\mathbf{M}_i$, μ_i, ρ_i, and p_i represent the velocity vector, Maxwell's stress tensor ($\varepsilon_0 \varepsilon_i \left[\psi_i \otimes \psi_i - 0.5\left(\psi_i \cdot \psi_i\right)\mathbf{I}\right]$), dynamic viscosity, density, and pressure, respectively, for the i^{th} fluid. The vector **g** represents the acceleration due to gravity acting in the negative *y* direction (Figure 5.1). In absence of a magnetic field, the irrotational ($\nabla \times \psi_i = 0$) electric field (ψ_i) was expressed in terms of the electric field potential (V_i) as, $\psi_i = -\nabla V_i$, which transformed the Gauss's law for leaky dielectric fluids [$\nabla \cdot \left(\sigma_i \psi_i\right) = 0$] into the Laplace equation, $\nabla^2 V_i = 0$. Divergence of the Maxwell's stress tensor provided the electrostatic force (f^c) acting on the leaky dielectric materials as,

$$f^c = \nabla \cdot \mathbf{M}_i = -\frac{1}{2}\varepsilon_0 \psi_i^{\,2} \nabla \varepsilon + q\psi_i \tag{5.3.3}$$

where, $q = \nabla \cdot (\varepsilon_0 \varepsilon \psi_i), \varepsilon_0, \nabla\varepsilon$, and σ are the charge density, permittivity of free space, gradient of permittivity, and relative conductivity of the phases. The charge density q could also be expressed as,

$$q = \varepsilon_0 (\sigma \psi_i) \cdot \nabla \left(\frac{\varepsilon}{\sigma} \right) \tag{5.3.4}$$

In past few decades, different numerical methods have emerged to accurately model the dynamics of the deforming interfaces in a multiphase flow. In this regard, volume of fluid (VOF),[8,9] volume of fluid coupled with level set (CLSVOF)[10-12] and the phase field[13-15] methods were integrated with finite volume, finite difference or finite element frameworks of numerical analysis. Further, the Lattice-Boltzmann method (LBM)[16] was also employed to track the interface of the two-phase flows. In the present work, the spatiotemporal tracking of the deforming oil-water interface was done using the most accurate CLSVOF method.[17-19] The level set equation representing the interface was expressed as,

$$\dot{\phi} + \mathbf{u}_i \cdot \nabla \phi = \lambda \nabla \cdot \left(\delta \nabla \phi - \phi(1-\phi) \frac{\nabla \phi}{|\nabla \phi|} \right) \tag{5.3.5}$$

where the parameter ϕ was the level set function, which acquires a value of < 0 in oil, > 0 in water, and zero at the fluid interface (Γ). In Eq. (5.3.5), the symbol λ controls the extent of stabilization and θ is the thickness of the diffused interface. The values of λ and δ used in this study are 1 ms^{-1} and 1.625 μm respectively. In order to determine the smallest possible value of λ a detailed numerical study has been performed previously by Olsson et al.[19] and the conclusion of that work is, to ensure mass conservation, the time scale related to stabilization should be much smaller than the time scale of advection of interface, so that $(\delta/\lambda) < (l/U) \approx (\delta/\lambda) < (l/Bo_e)$ where l is the characteristic length scale

of the system (which is 0.3, 0.5 or 0.8 mm for our case), U is the characteristic speed of advection of the droplet which can be represented as $U \sim \mathrm{O}\left(Bo_e\right)$ and Bo_e is the electrical Bond number.[19] Maximum value of Bo_e used in our simulations is ≈ 4 which means the minimum (maximum) value of the right hand side of the above inequality is of the order of 10^{-5} (10^{-4}) and using the values that we have taken for λ and δ gives the order of $(\delta/\lambda) \approx 10^{-6}$ which is smaller than the right hand side of the inequality which ensures that the values taken for λ and δ are well within the limit. The surface tension force $\mathbf{f}_{st}$ in Eq. (5.3.2) was calculated as, $\mathbf{f}_{st} = \int_\Gamma \gamma \boldsymbol{\kappa} \mathbf{n}\, dS = \gamma \kappa \nabla \phi = -\gamma \left(\nabla \cdot \left[\nabla \phi / |\nabla \phi|\right]\right) \nabla \phi$, where, κ, S, and **n** denote the curvature at the interface, line element on the interface, and unit outward normal vector along Γ, respectively. The parameters density (ρ), viscosity (μ), permittivity (ε), and conductivity (σ), were assumed to be constant in the phases and was evaluated from the expression, $a(\phi) = \left[a_1 + (a_2 - a_1) H(\phi)\right]$, where a can be any of ρ, μ, ε, and σ, and $H(\phi)$ is the Heaviside function, $H(\phi) = (0 \text{ if } \phi < 0); (0.5 \text{if } \phi = 0); (1 \text{ if } \phi > 0)$.

Table 5.2: Microchannel dimensions and meshing schemes for different modes of droplet breaking shown in the Figure 1 (a) – (c).

Figure	Mode	Diameter of channel (*d*, mm)	Channel Length (*l*, mm)	Mesh Quality
5.1(a)	Fission	0.3	2.0	14520
5.1(b)	Cascade	0.5	5.5	35860
5.1(c)	Rayleigh	0.8	10.4	49456

At the oil inlet, normal inflow velocity boundary condition was enforced and at the outlet, default pressure with zero viscous stress boundary condition was fixed. The channel walls were considered to be non-wetting (contact angle θ = 150°), non-slipping, and

impermeable. The contact angle mentioned here is for the situation when a sessile water droplet on the wall of PDMS microchannel is surrounded by silicone oil. Finally, constant potential voltage boundary conditions were enforced at anode ($V_i = V_0$) and cathode ($V_i = 0$). The dimensions of the microchannel and the mesh after the grid independence tests are shown in the Table 5.2. The governing equations and the boundary conditions were solved using the commercial package COMSOL™ Multiphysics, which employs finite element method to obtain numerical solutions. The software used Galerkin least-square (GLS) method along with the second order elements for velocity and first order elements for pressure gradient calculations to discretize the nonlinear convective diffusion equations. The segregated predictor-corrector method with incremental pressure correction led to the velocity and pressure profiles for the flow. A second-order backward difference method led to consistent initialization and time-marching with optimal time step size of ~10^{-4} s. The validation of this model with the theoretical analysis is presented in **Appendix- B**. The typical fluid properties are enlisted in Table 5.1.

5.4 RESULTS AND DISCUSSION

The pressure driven two-phase flows display stratified, plug, slug, droplet, or core-annular flow morphologies with the variations in the flow rate or viscosity or density of the phases, and surface or interfacial tension.[20-25] However, the droplet flows are the most favored one for microfluidic applications because of the availability of larger interfacial area per unit volume for efficient energy, mass, and momentum transfer. Thus, the major objectives in the recent years have been, (i) digitize the flow patterns, (ii) miniaturize the size of these droplets for further enhancement in the surface to volume ratio, and (iii) improve the throughput. In this direction, application of external electrostatic fields has

shown serious potential because the two-phase flow patterns can indeed deform and then disintegrate to form flow structures with higher surface to volume ratio.[6-8,10,16,26-30] In what follows, we show some ingenious way electric field arrangements around a simple microchannel, which could break a single droplet into numerous smaller ones having very high surface to volume ratio.

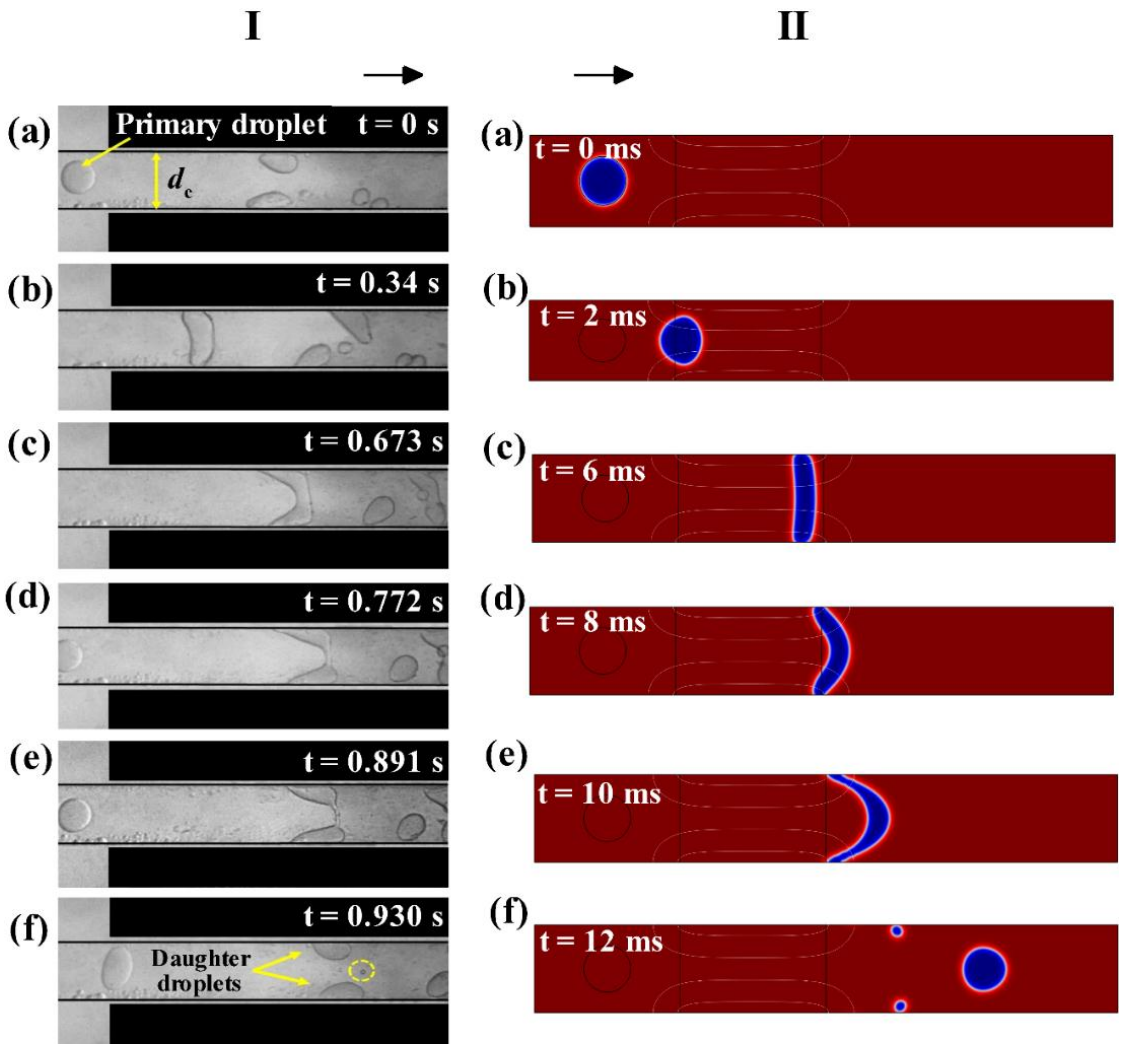

Figure 5.3: (I)[(a) – (f)] show the experimental snapshots at different time (t) of a water droplet splitting into three in the *fission* mode inside a microchannel (d_c = 0.3 mm) when the process parameters are, $u_1 = 2.64 \times 10^{-3}$ m s^{-1}, $u_2 = 0.062 \times 10^{-3}$ m s^{-1}, $\gamma = 0.0084$ N m^{-1}, $\varepsilon_r = \varepsilon_2 / \varepsilon_1 = 36.4, \psi_1 = 3.067$ MV m^{-1}, and $\sigma_r = \sigma_2 / \sigma_1 = 8.63 \times 10^9$ leads to Re_w = 0.0186, $Ca_w = 7.405 \times 10^{-6}$, $We_w = 1.378 \times 10^{-7}$, $Bo = 2.84 \times 10^{-3}$. (II)[(a) – (f)] show

simulated results obtained of the same phenomenon when, u_1 = 0.1 m s^{-1}, u_2 = 0 m s^{-1}, γ = 0.015 N m^{-1}, ψ_1 = 1.2 MV m^{-1}, $\varepsilon_r = \varepsilon_2 / \varepsilon_1 = 36.4$, and $\sigma_r = \sigma_2 / \sigma_1 = 100$. The width of electrode is 0.5 mm and is placed at 0.5 mm downstream from the oil inlet boundary. The arrowheads show the direction of flow from left to right hand side and the white contours near the electrodes show field lines of EHD force. The red (blue) color shows oil (water) phase.

We initiate the discussion with fission mode where a single droplet was broken into three daughter droplets, as shown by the experiments in the column I and simulations in the column II of Figure 5.3. Images (a) – (c) in this figure suggest that when a water droplet suspended in a continuous oil phase was flown through a zone with moderately high electric field, it elongated to form a water plug across the channel. The higher dielectric permittivity of the water droplet as compared to the oil phase led to the accumulation of a larger number of induced bound charges across the interface, which generated the EHD stress to elongate the droplet towards the electrodes and form the plug inside the channel.[15] Images (d) – (f) suggest that when the droplet moved downstream of the channel the water plug broke down to form three smaller droplets when the applied field intensity was, ψ_1 = 1.2 MV m^{-1} (simulation). Both the simulated and experimental results confirmed that indeed a bigger droplet could split into three smaller droplets when flown through a zone of electric field exposure. The images from the simulations and experiments also suggested that, although the channel was a hydrophobic one, the pair of relatively small water droplets generated near the electrodes were quite strongly attached to the channel wall as they moved downstream owing to the acquired induced charge of opposing polarity to that of the nearest electrode. Thus, apart from droplet miniaturization, the

fission mode could also produce a pair of charged droplets inside a straight microchannel.[31]

It may be noted here that, in the fission mode, the droplet disintegrated into smaller ones only beyond a critical field intensity of, ψ_c ~ 3.067 MV m^{-1} (experiment) and ψ_c ~ 1.2 MV m^{-1} (simulation) where the EHD stress could overcome the stabilizing component of capillary force at the oil-water interface. The water plug did not split into droplets when the field intensity was less than ψ_c and regained the circular shape from the plug shape when moved out of the zone of electric field exposure. It may also be noted here that the experimental and the simulated results showed rather a qualitative similarity in droplet breaking mechanism because the conditions were not exactly identical in both the situations. In particular, the simulated system showed a much faster breakup than the experimental one. The droplet produced near the electrodes were larger in the experimental studies while the simulated one showed the generation of a pair of much smaller droplets near the electrodes. However, the simulations could quite effectively explain the mechanism of the droplet breaking in the experiments and the subsequent transport of the smaller droplets towards the downstream of the channel. Concisely, the images in Figure 5.3 suggests a simpler way for controlled splitting of droplets in a microfluidic environment than the previously reported ones where either a single droplet was produced inside straight microchannel[32] or a complex geometrical arrangement was necessary for the multiplicity of the droplets.[31-33]

Importantly, the fission mode could be repeatedly employed to get the cascade mode of droplet formation. Figure 5.4 shows an example of the cascade mode in which a droplet of diameter 260 μm could be disintegrated in a controlled manner to form smaller droplets

when the primary droplet passed through a series of zone with electric field exposure in the downstream of the microchannel. Here, we chose a droplet larger than the previous case, because if the initial droplet is not large enough, the smaller daughter droplets formed after multiple splitting would be so small that the interface tracking would be very difficult. Keeping this point in our mind, we selected droplet diameter in the simulation. During experiment, we kept in our mind that the droplet will move at a lowest possible velocity and accordingly we selected Q_r values.

Images (b) – (d) in this figure shows the formation of a pair of secondary, tertiary, and quaternary droplets of almost uniform size (image (e)) when passed through the first, second, and third zones of electric field exposure, respectively. The 260 μm primary droplet kept on producing a pair of smaller droplets of size 52 – 75 μm in each zone of electric field exposure as the droplet progressed downstream. It can easily be envisaged that this methodology can repeatedly be employed for many more cycles to produce a large collection of microdroplets in a continuous oil medium. The uniqueness of this methodology is the droplet size and the number can be meticulously controlled by tuning the field intensity and the zones of exposure of the electric field across the channel.

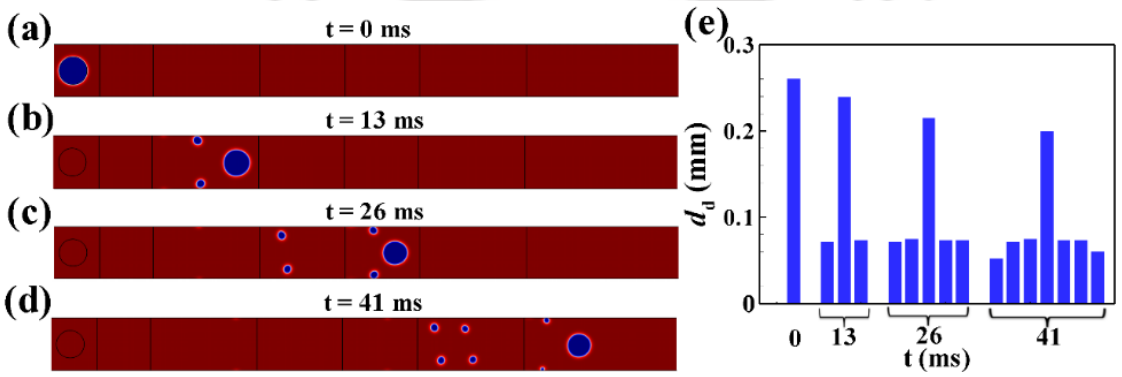

Figure 5.4: Images (a) – (d) show the spatiotemporal droplet formation in the C*ascade* mode inside a microchannel (d_c = 0.5 mm). Plot (e) shows the variation of d_d with t. The

other parameters are, u_1 = 0.1 m s^{-1}, u_2 = 0 m s^{-1}, $\rho_1 = \rho_2$ = 1000 kg m^{-3}, μ_1 = 0.01 Pa s, μ_2 = 0.001 Pa s, γ = 0.01 N m^{-1}, $\psi_1 = \psi_2$ = 1.2 MV m^{-1} and ψ_3 = 1.16 MV m^{-1}, σ_1 = 10^{-6} S m^{-1}, σ_2 = 10^{-4} S m^{-1}, $\varepsilon_r = \varepsilon_2 / \varepsilon_1 = 36.4$, and θ = 150°. Three pairs of electrodes of width w_1 = 0.5 mm, w_2 = 0.8 mm, and w_3 = 1.0 mm, are placed 0.5 mm, 2 mm and 3.6 mm downstream from the oil inlet boundary respectively. The red (blue) color shows oil (water) phase.

Importantly, the fission mode could be repeatedly employed to get the cascade mode of droplet formation. Figure 5.4 shows an example of the cascade mode in which a droplet of diameter 260 μm could be disintegrated in a controlled manner to form smaller droplets when the primary droplet passed through a series of zone with electric field exposure in the downstream of the microchannel. Images (b) – (d) in this figure shows the formation of a pair of secondary, tertiary, and quaternary droplets of almost uniform size (image (e)) when passed through the first, second, and third zones of electric field exposure, respectively. The 260 μm primary droplet kept on producing a pair of smaller droplets of size 52 – 75 μm in each zone of electric field exposure as the droplet progressed downstream. It can easily be envisaged that this methodology can repeatedly be employed for many more cycles to produce a large collection of microdroplets in a continuous oil medium. The uniqueness of this methodology is the droplet size and the number can be meticulously controlled by tuning the field intensity and the zones of exposure of the electric field across the channel.

Interestingly, when the channel diameter and the width of the zone of electric fields were systematically varied we observed Rayleigh mode of droplet breaking, as shown in Figure 5.5. The channel diameter was increased in order to accommodate larger size droplet. If the initial droplet is not large enough, the smaller daughter droplets formed after multiple

splitting would be so small that the interface tracking would be very difficult. For example, for a channel of d = 0.8 mm when three different zone of electric field exposure were created with electrode width, w_1 = 0.8 mm , w_2 = 1.0 mm, and w_3 = 1.2 mm, having field intensity of , $\psi_1 = \psi_2 = \psi_3$ = 1.25 MV m^{-1} and separated by a distance of 0.8 mm, 4.0 mm, 6.2 mm from the oil inlet.

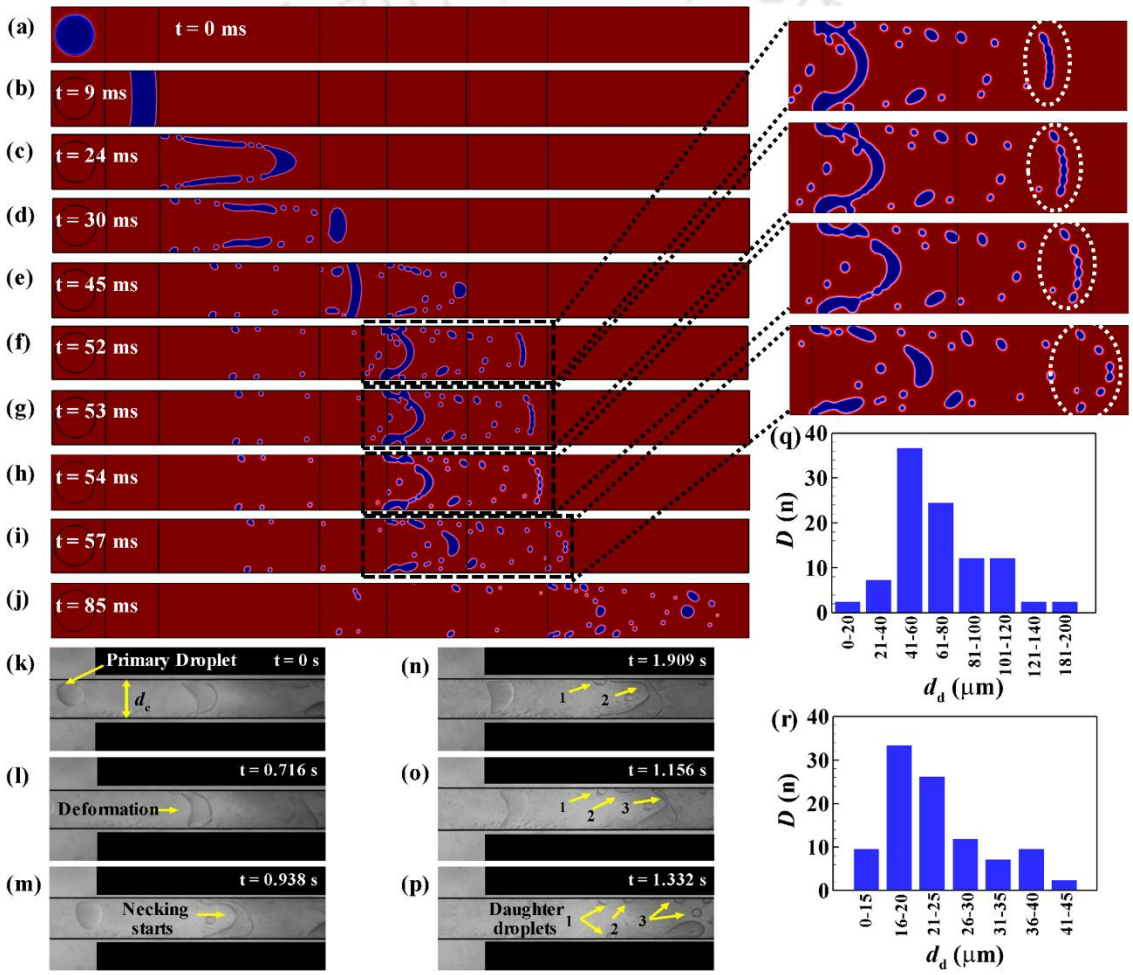

Figure 5.5: Images (a) – (j) show the spatiotemporal droplet formation in the *Rayleigh* mode when d_d = 0.6 mm and d_c = 0.8 mm in simulations. The magnified portions of the zones marked by dark broken lines are shown on the right of the image in which the lighter broken lines show the *Rayleigh* instability. Images (k) – (p) show the droplet deformation and disintegration into daughter droplets inside microchannel (d_c = 0.3 mm) experimentally at different time (t) where the employed experimental parameters are, u_1 =

1.18×10^{-3} m s^{-1}, $u_2 = 0.062 \times 10^{-3}$ m s^{-1}, $\gamma = 0.0048$ N m^{-1}, $\varepsilon_r = \varepsilon_2 / \varepsilon_1 = 36.4$, $\psi_1 = 1.11$ MV m^{-1}, and $\sigma_r = \sigma_2 / \sigma_1 = 8.63 \times 10^9$ which leads to $Re_w = 0.0186$, $Ca_w = 1.296 \times 10^{-5}$, $We_w = 2.41 \times 10^{-7}$, $Bo = 4.96 \times 10^{-3}$. Plots (q) and (r) show the size distribution, D (n), of droplets in the downstream of the channels with $d_c = 0.8$ mm and 0.3 mm, respectively. The other parameters employed in the simulations are, $u_1 = 0.1$ m s^{-1}, $u_2 = 0$ m s^{-1}, $\rho_1 = \rho_2 = 1000$ kg m^{-3}, $\mu_1 = 0.01$ Pa s, $\mu_2 = 0.001$ Pa s, $\gamma = 0.003$ N m^{-1}, $\psi_1 = \psi_2 = \psi_3 = 1.25$ MV m^{-1}, $\sigma_1 = 10^{-6}$ S m^{-1}, $\sigma_2 = 10^{-4}$ S m^{-1}, $\varepsilon_r = \varepsilon_2 / \varepsilon_1 = 36.4$, and $\theta = 150^\circ$. Three different zone of electric field exposure were created with electrode width, $w_1 = 0.8$ mm, $w_2 = 1.0$ mm, and $w_3 = 1.2$ mm, and separated by a distance of 0.8 mm, 4.0 mm, 6.2 mm from the oil inlet. The red (blue) color shows oil (water) phase.

Images (a) – (j) in Figure 5.5 show the spatiotemporal evolution of the flow at different time intervals. The images (a) and (b) show that when a primary droplet of size $d_d = 0.6$ mm entered in the domain of first electric field exposure, it initially formed a water plug. However, the movement of the water plug was slower near the boundaries due to the strong frictional force alongside the vertical attraction from the electric field exposure. The central part of the plug moved relatively faster due to the pressure from the oil flow, which eventually led to the 'boomerang' shape of the water plug with a convex front and concave rear, as shown in the image (c). The parabolic shaped plug stretched longer with time and underwent Rayleigh-Plateau[33-35] instability to form a number of droplets of non-uniform size distribution, as shown in the images (c) and (d). Importantly, images (d) – (f) show that when the largest droplet in the front, ejected out from the first zone of electric field exposure, entered into the second zone of electric field exposure, it initially formed a plug and then disintegrated into smaller droplets following a similar mechanism, as shown in the images (a) – (c). Again, images (f) – (i) suggest that when the largest droplet in the front issuing out of the second zone of electric field exposure entered into the final zone of

electric field exposure, it underwent vertical stretching and Rayleigh-Plateau[33-35] instability simultaneously to produce numerous smaller droplets. The insets on the right hand side of the images (f) – (i) show the magnified zones, indicated by the broken lines in dark on the original images, where this phenomenon took place. The stretched water plug 'pearled' into a garland of droplets as marked by the broken lines in white. Further, image (j) shows any of the bigger droplets issuing to the third zone of electric field exposure underwent similar stretching followed by 'pearling' through Rayleigh-Plateau[33-35] instability to create a large collection of smaller droplets at the extreme downstream of the microchannel.

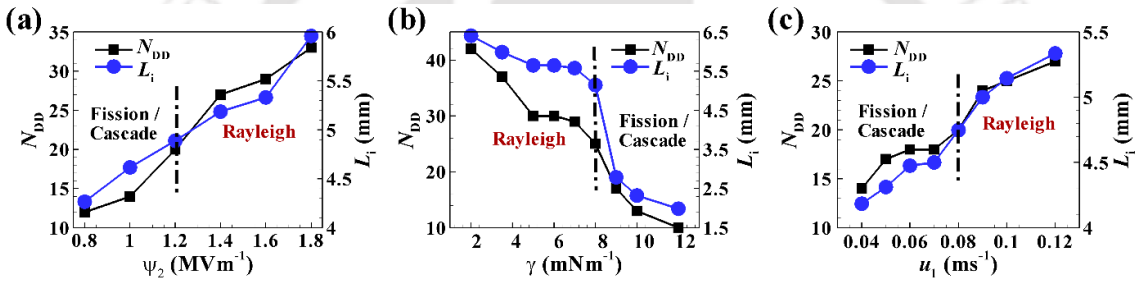

Figure 5.6: Plots (a) – (c) show the variations in interfacial contact length (L_i – circular symbols, blue lines, right side of *y*-axis) and the number of daughter droplets generated (N_{DD} – square symbols, black lines, left side of *y*-axis) with ψ_2, γ, and u_1, respectively, when d_d = 0.6 mm and d_c = 0.8 mm. Plots (a), (b) and (c) also classify the prevalent mode of droplet breakup mechanism (fission/cascade or Rayleigh) for each parameters like, ψ_2, γ, and u_1. The other parameters employed for the plots are, u_1 = 0.1 m s^{-1} [for plots (a) and (b)], u_2 = 0 m s^{-1}, $\rho_1 = \rho_2$ = 1000 kg m^{-3}, μ_1 = 0.01 Pa s, μ_2 = 0.001 Pa s, ψ_1 = 1.25 MV m^{-1}, ψ_2 = 1.25 MV m^{-1} [for plots (b) and (c)], ψ_3 = 1.25 MV m^{-1}, γ = 0.008 N m^{-1} [for plots (a) and (c)], σ_1 = 10^{-6} S m^{-1}, σ_2 = 10^{-4} S m^{-1}, $\varepsilon_r = \varepsilon_2 / \varepsilon_1 = 36.4$, and θ = 150°. Electrodes of width w_1 = 0.8 mm, w_2 = 1.0 mm and w_3 = 1.2 mm, are placed at a distance of 0.8 mm, 4 mm and 6.2 mm from the oil inlet boundary respectively.

Images (k) – (p) in the Figure 5.5 show the experimental Rayleigh mode breakup, which corroborate the observations in the simulated results shown in images (a) – (d). The

experimental images suggest that when the primary droplet approached towards the pair of electrodes (image (k), t = 0 s), it deformed into a plug shape inside the microchannel, as shown in the image (l). Images (m) shows the 'necking' (t = 0.938 s) of the plug with time, as previously observed in the simulated image (c). Images (n) – (p) show the Rayleigh mode of breakup into many smaller droplets, as indicated by the arrows. The analysis of droplet size and their distribution from the simulations in the plot (q) suggests that the Rayleigh mode could disintegrate a 600 μm droplet into 28 droplets of size less than 80 μm in which the smallest size was ~20 μm. Further the plot (r) shows that this phenomenon was also possible when the diameter of the microchannel (d) and droplet diameter (d_d) were reduced to 300 μm and 200 μm, respectively. In this this situation, the electric field intensities were, $\psi_1 = \psi_2 = \psi_3 = 1.25$ MV m^{-1}, the electrode widths were, w_1 = 0.8 mm, w_2 = 1.0 mm, and w_3 = 1.2 mm, and the electrodes were separated by a distance of, 0.8 mm, 4.0 mm, 6.2 mm from the oil inlet. Plot (r) suggests that in such a scenario a 200 μm droplet was fragmented into ~30 smaller droplets of size less than 25 μm in which smallest one was ~10 μm. Concisely, Figure 5.5 shows a one-step process to produce water-in-oil microemulsion from a droplet driven multiphase flow by discrete application of multiple EHD fields around a microchannel.

Images (a) – (c) in the Figure 5.6 show the sensitivity of the field intensity at the second electrode (ψ_2), interfacial tension (γ), and the oil flow rate (u_1) on the number of droplets produced (N_{DD}) and cumulative length of the interfacial contact between oil and water (L_i). Among all the other parameters, we found that these three parameters were the most influential ones in facilitating the Rayleigh mode inside the microchannel. The parameter L_i is calculated as the total length of the oil–water interface, which is the product of the

number of droplets produced (or flow features) with the perimeter of each droplet (or flow feature). The parameter L_i by definition is a measure of the total available interface for energy, mass, or momentum exchange while N_{DD} is a measure of the extent of miniaturization and throughput. The parameters L_i and N_{DD} are calculated at the extreme downstream of the channel when all the droplets were out of the zone of electric field exposure. All the plots suggest that the transition from fission or cascade mode to Rayleigh mode took place with increase in ψ_2 and u_1 as well as reduction in γ. While the reduction in the interfacial tension facilitated the miniaturization of the droplets by reducing the surface energy of the fragmented droplets, increase in the electric field and the oil flow rate enabled the 'stretching', 'deformation', 'necking' and 'disintegration' stages of the Rayleigh mode of droplet breaking. The broken vertical line in the plots (a) – (c) in Figure 5.6 show the conditions beyond or below which the transition from the fission or cascade to Rayleigh mode led to the rapid reduction in the size of the droplet, increase in the number of droplet, enhancement in the interfacial area for mass, energy and momentum transfer, and improvement in the net throughput from the channel.

5.5 SUMMARY

In this chapter, numerical simulations corroborated by the experiments have shown some interesting electric field induced disintegration of a water droplet into several miniaturized ones inside a straight microchannel with the ingenious application of discrete electric fields of variable intensity at multiple locations. The major conclusions from the study are as follows,

(i) Strategic placement of a pair of electrodes in the downstream of the channel could engender a fission mode of droplet splitting in which a bigger droplet was split into three

smaller ones. This is very much similar to the one observed in **Chapter 4**. Repeated application of such electric fields at the downstream of the microchannel showed the onset of the cascade mode in which a single droplet could be fragmented into three, five, and seven smaller droplets when the electric field was generated in one, two, and three different locations, respectively, having different intensities. The cascade mode shows a systematic way to disintegrate a droplet into many smaller ones with the help of localized Maxwell's stresses generated at the oil-water interfaces.

(ii) A transition from cascade/fission to Rayleigh mode was observed for the droplets with lower interfacial tension when the oil flow rate and the intensity of the localized field were significantly higher. While the electric field helped in elongating the droplet in the normal direction of the flow, the oil flow helped in deforming, necking, and disintegration of the elongated droplet to facilitate the Rayleigh instability for droplet breakup. Remarkably, in such a scenario, a droplet could be broken into 40 or more parts having minimum size ~30 times smaller than the initial one. The Rayleigh mode showed an interesting pathway to rapidly disintegrate a droplet into an array of miniaturized ones, which can be useful for enhanced mass, energy and momentum transfer. The water-in-oil emulsion produced in the downstream of such channels showcase a single step method to produce microemulsion inside the straight microchannels.

5.6 ACKNOWLEDGEMENTS

We thank DEITY grant no. 5(9)/2012-NANO, DST-SERB, grant no. SR/S3/CE/0079/2010, and DST FIST grant no. SR/FST/ETII-028/2010, Government of India, for the financial aids. Supports from Mr. Joydip Chaudhuri is gratefully acknowledged.

5.7 REFERENCES

1. M. K. S. Verma, A. Majumder, and A. Ghatak, Langmuir **22**, 10291 (2006).
2. M. K. S. Verma, S. R. Ganneboyina, Rakshith, and A. Ghatak, Langmuir **24**, 2248 (2008).
3. S. H. Song, C. K. Lee, T. J. Kim, I. Shin, S. C. Jun, and H. I. Jung, Microfluid Nanofluid **9**, 533 (2010).
4. Y. Jia, J. Jiang, X. Ma, Y. Li, H. Huang, K. Cai, S. Cai, and Y. Wu, Chinese Science Bulletin **53**, 3928 (2008).
5. S. Mhatre and R. Thaokar, Industrial & Engineering Chemistry Research **53**, 13488 (2014).
6. S. Torza, R. G. Cox, and S. G. Mason, Philosophical Transactions of the Royal Society of London. Series A, Mathematical and Physical Sciences **269**, 295 (1971).
7. J. D. Sherwood, Journal of Fluid Mechanics **188**, 133 (1988).
8. J. M. Lopez-Herrera, S. Popinet, and M. A. Herrada, Journal of Computational Physics **230**, 1939 (2011).
9. G. Tomar, D. Gerlach, G. Biswas, N. Alleborn, A. Sharma, F. Durst, S. W. J. Welch, and A. Delgado, Journal of Computational Physics **227**, 1267 (2007).
10. J. Q. Feng and T. C. Scott, Journal of Fluid Mechanics **311**, 289 (1996).
11. G. Tomar, G. Biswas, A. Sharma, and A. Agarwal, Physics of Fluids **17**, 112103 (2005).
12. D. Gerlach, G. Tomar, G. Biswas, and F. Durst, International Journal of Heat and Mass Transfer **49**, 740 (2006).
13. D. Jacqmin, Journal of Computational Physics **155**, 96 (1999).

14. V. E. Badalassi, H. D. Ceniceros, and S. Banerjee, Journal of Computational Physics **190**, 371 (2003).
15. Y. Lin, P. Skjetne, and A. Carlson, International Journal of Multiphase Flow **45**, 1 (2012).
16. J. Zhang and D. Y. Kwok, Journal of Computational Physics **206**, 150 (2005).
17. J. A. Sethian and P. Smereka, Annual review of fluid mechanics **35**, 341 (2003).
18. Y. Lin, Electrophoresis **34**, 736 (2013).
19. E. Olsson, G. Kreiss, and S. Zahedi, Journal of Computational Physics **225**, 785 (2007).
20. P. Garstecki, M. J. Fuerstman, H. A. Stone, and G. M. Whitesides, Lab on a Chip **6**, 437 (2006).
21. R. M. Santos and M. Kawaji, International Journal of Multiphase Flow **36**, 314 (2010).
22. T. Cubaud and T. G. Mason, Physics of Fluids **20**, 053302 (2008).
23. T. Cubaud and T. G. Mason, Physical Review Letters **96**, 114501 (2006).
24. S. Timung, V. Tiwari, A. K. Singh, T. K. Mandal, and D. Bandyopadhyay, The Canadian Journal of Chemical Engineering **93**, 1736 (2015).
25. L. Shui, A. van den Berg, and J. C. T. Eijkel, Lab on a Chip **9**, 795 (2009).
26. S. Lecuyer, W. D. Ristenpart, O. Vincent, and H. A. Stone, Applied Physics Letters **92**, 104105 (2008).
27. O. Vizika and D. A. Saville, Journal of Fluid Mechanics **239**, 1 (1992).
28. M. Sato, S. Kato, and M. Saito, IEEE Transactions on Industry Applications **32**, 138 (1996).
29. P. Singh and N. Aubry, Electrophoresis **28**, 644 (2007).

30. D. W. Jonathan, C. Larry, and K. Ranganathan, Applied Physics Letters **103**, 054101 (2013).

31. H. Zhou and S. Yao, Lab on a Chip **13**, 962 (2013).

32. D. R. Link, E. Grasland-Mongrain, A. Duri, F. Sarrazin, Z. Cheng, G. Cristobal, M. Marquez, and D. A. Weitz, Angewandte Chemie International Edition **45**, 2556 (2006).

33. D. R. Link, S. L. Anna, D. A. Weitz, and H. A. Stone, Physical Review Letters **92**, 054503 (2004).

34. S. D. Masumi Yamada, Hirosuke Maenaka, Masahiro Yasuda, Minoru Seki, Journal of Colloid and Interface Science **321**, 401 (2008).

35. A. Carlson, M. Do-Quang, and G. Amberg, International Journal of Multiphase Flow **36**, 397 (2010).

Chapter 6

Microfluidic energy harvester

ABSTRACT

In this chapter, we demonstrate a droplet of NaCl – water solution generated electricity in the presence of light when it was placed between two cylindrical electrodes of Cu and Cu_2O. The generated voltage varied with different kinds of light sources and it was found that under solar illumination the generated voltage was maximum. Moreover, gold nanoparticles in the droplet enhanced the voltage generation due to their surface plasmon resonance. The maximum generated voltage was found to be ~120 mV under solar illumination for a single droplet. The effects of different parameters like salt concentration, light source distance, droplet volume, nanoparticle loading etc. were also studied. In order to further enhance the voltage generation convex lens was also used to focus solar light on the droplet. The generated voltage could be increased using multiple droplets and a maximum of ~320 mV was achieved using five such droplets. Moreover, the maximum power density achieved in this case is ~13 $\mu w/cm^2$ under solar illumination. The similar phenomenon was also implemented in microchannel which increased the performance of the system. It was found that at a critical flow rate the generated voltage and current density was enhanced which led to a ~13 fold increment in power density. In this case, the effect of electrochemical photovoltaics, surface plasmon resonance, and streaming potential was combined to improve the efficiency of the device. Interestingly, the combined effect of the mentioned three effects could increase the efficiency of the system by five times to ~1.7% as compared to the situation when the salt electrolyte was held stationary in the microfluidic device (~0.35%). Thus, the proposed microchannel based energy harvester is a potential candidate for the large area solar energy harvester.

This chapter is published in Indian Patent, 201631036408 A, 2016

6.1 INTRODUCTION

In this study, we report the design and development of a pair of micro power harvesters, namely, (i) droplet energy harvester (DEH) and (ii) microfluidic energy harvester (MEH). The DEH consists of a salt-water microdroplet placed at the junction of a pair of Schottky barrier Cu-Cu_2O electrodes, which can convert the solar energy into the electrical one, emulating the principles of electrochemical photovoltaics (ECPV).[1-3] Use of suspended gold nanoparticles (AuNPs) inside the microdroplet helps in improving the efficiency the DEH due to generation of additional current inside the DEH owing to the surface Plasmon resonance (SPR) of AuNPs under the electromagnetic irradiation.[4-9] In order to obtain even higher efficiencies, the DEH is converted into MEH in which the nanoparticle laden salt-water solution is flown inside a microfluidic channel integrated with a Schottky barrier Cu-Cu_2O electrodes. While the combined effects of the ECPV and SPR can convert the solar energy into the electrical one inside the MEH, the mechanical energy due to the flow of the electrolyte generated streaming potential (SP) across the electrodes to harvest additional electrical energy. The combined effects of the ECPV, SPR, and SP inside the MEH help in obtaining an efficiency of ~2.5% under direct solar illumination, which is perhaps the highest among the reported ones. A very large scale integration (VLSI) of the DEHs and MEHs is envisioned to supply energy to diverse modern day gadgets such as mobile phones, tablets, laptops, or display units.

6.2 MATERIALS AND METHODS

6.2.1 Materials

Hydrochloric acid (HCl), sodium hydroxide (NaOH) pellets, sodium chloride (NaCl), 99.8% were procured from Merck (India). Gold (III) chloride ($HAuCl_4.3H_2O$), sodium borohydride ($NaBH_4$), 98% were obtained from Sigma-Aldrich (India). Polydimethyl

siloxane or PDMS (Dow Corning, Sylgard 184) was procured from Kevin Electrochem (India). The chemicals were of analytical grade and directly employed for the study. The Cu wire, Glass substrate, double sided tapes, lens, lasers, bulbs, and LEDS were purchased from the local venders. The Milli-Q water was used for cleaning and preparation of the solutions.

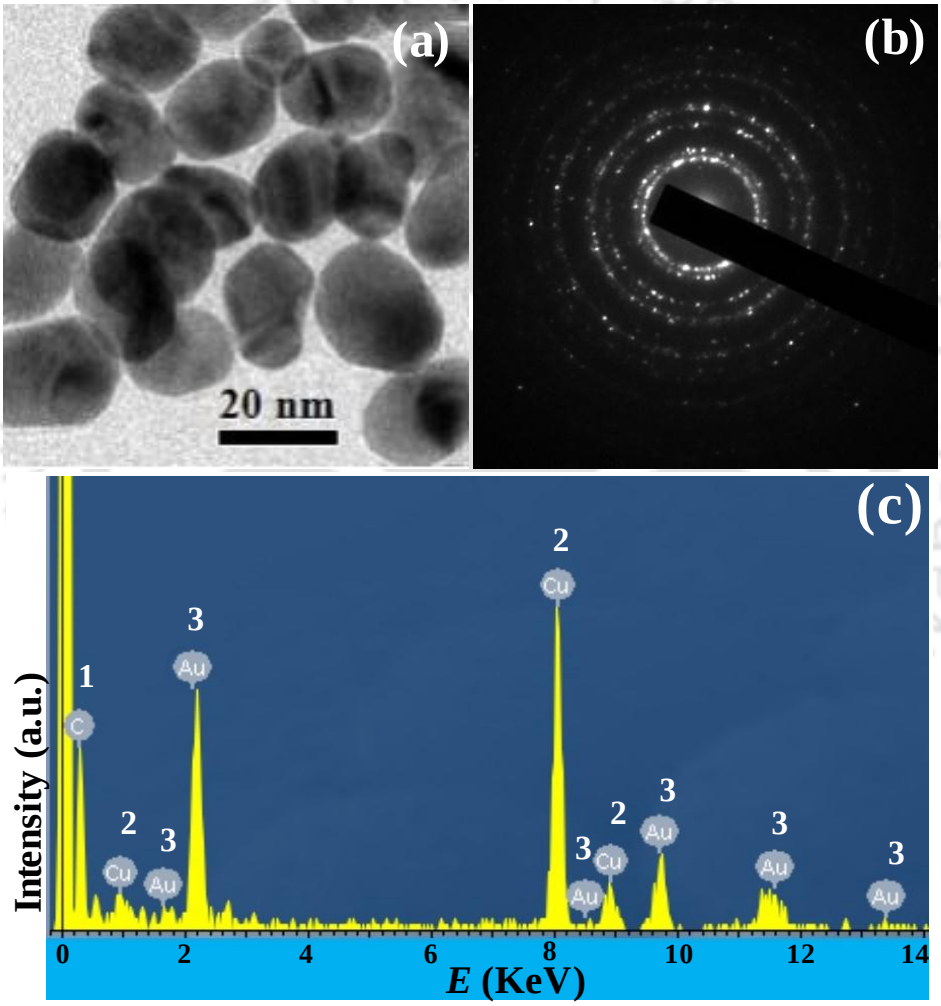

Figure 6.1: Image (a) shows the size and shape of the AuNPs from TEM. Image (b) shows the SAED pattern of synthesized AuNPs and image (c) shows the EDX of the same. The numbers 1 to 3 in the image (c) represents the peaks of C, Cu, and Au respectively.

6.2.2 Synthesis and characterizations of gold nanoparticles

The gold nanoparticles (AuNPs) were synthesized by reducing $HAuCl_4.3H_2O$.[10] Initially, we mixed $HAuCl_4.3H_2O$ with HCl in equal molar ratio, which resulted in a 50 mM $AuCl^{4-}$ aqueous solution (solution-I). Following this, $NaBH_4$ was dissolved in aqueous 1 mM NaOH in equal molar ratio to prepare 50 mM of BH^{4-} solution (solution-II). Thereafter, a solution of 0.5 mM gold ions was prepared by mixing 100 µl of solution-I with water. Then, a 300 µl of solution-II was mixed to the aqueous solution-I with continuous stirring. The change in color of the solution from pale yellow to orange to red after few minutes of stirring indicated the formation of AuNPs. Transmission electron microscope (TEM) was performed for analyzing the size and shape of the AuNPs while energy dispersive x-ray (EDX) spectroscopy confirmed the presence of Au, as shown in Figure 6.1.

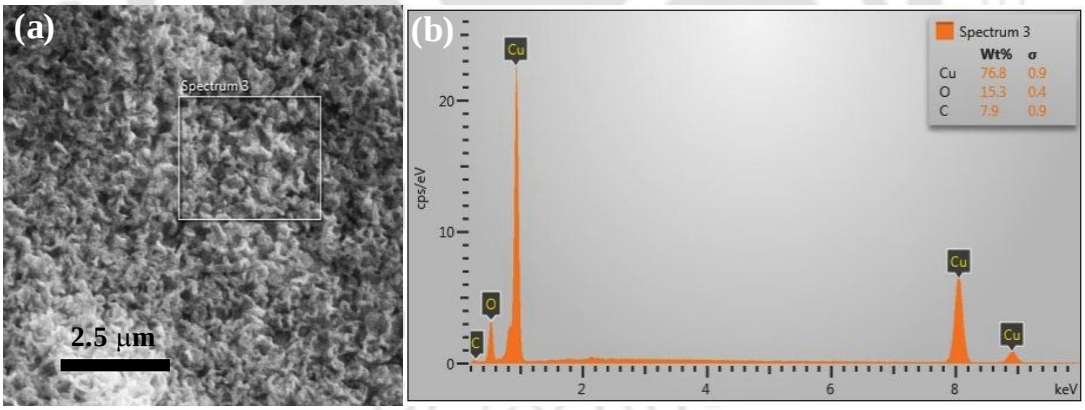

Figure 6.2: Image (a) shows the surface morphologies obtained from FESEM for the Cu_2O electrode and image (b) shows the Energy Dispersive X-ray (EDX) analysis of the same.

6.2.3 Synthesis and characterizations of copper oxide electrodes

Copper (I) oxide (Cu_2O) was grown on Cu electrodes using thermal oxidation method where the cylindrical copper wires were heated for 30 s, 60 s, 80 s, and 90 s in presence of air. Consequently, copper (I) oxide formed on the surface of copper wires alongside forming a small amount of copper (II) oxide. Field emission scanning electron microscope (FESEM) was performed to examine the surface morphology of the electrodes. Here, the details of the FESEM image and Energy Dispersive X-ray (EDX) analysis are shown in Figure 6.2.

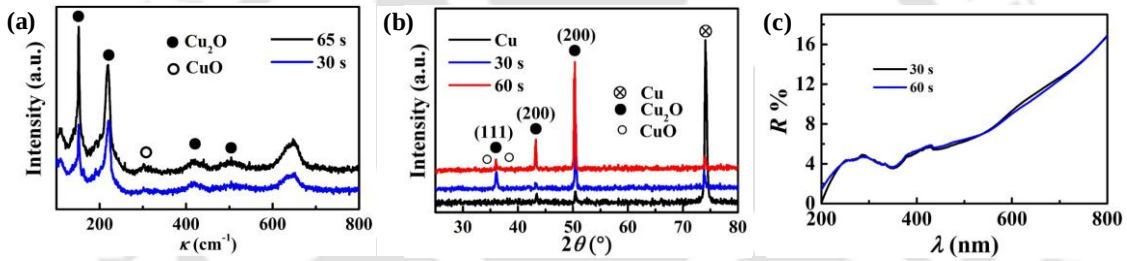

Figure 6.3: Images (a), (b) and (c) show the Raman spectroscopy, XRD, and UV-Vis spectroscopy characterizations, respectively, of the Cu_2O electrode at different time of heating.

Additionally, the Cu_2O electrodes were also characterized using Raman spectroscopy (Horiba Jobin Vyon, Model: LabRam HR) in which 514 nm was used for laser excitation and XRD (Bruker, Model-D8- Advance), as shown in images (a) and (b) in Figure 6.3, respectively. In both the analysis, we found characteristic peaks of Cu_2O with few small peaks of CuO. Therefore, both Raman spectroscopy and XRD analysis also confirmed successful growth of Cu_2O on electrode due to the thermal oxidation of Cu. The optical property of the prepared Cu_2O further characterized with UV-Vis spectroscopy (Shimadzu, UV-2600), as shown in Figure 6.3(c), in which the reflectance spectrum of fabricated Cu_2O electrode was plotted.

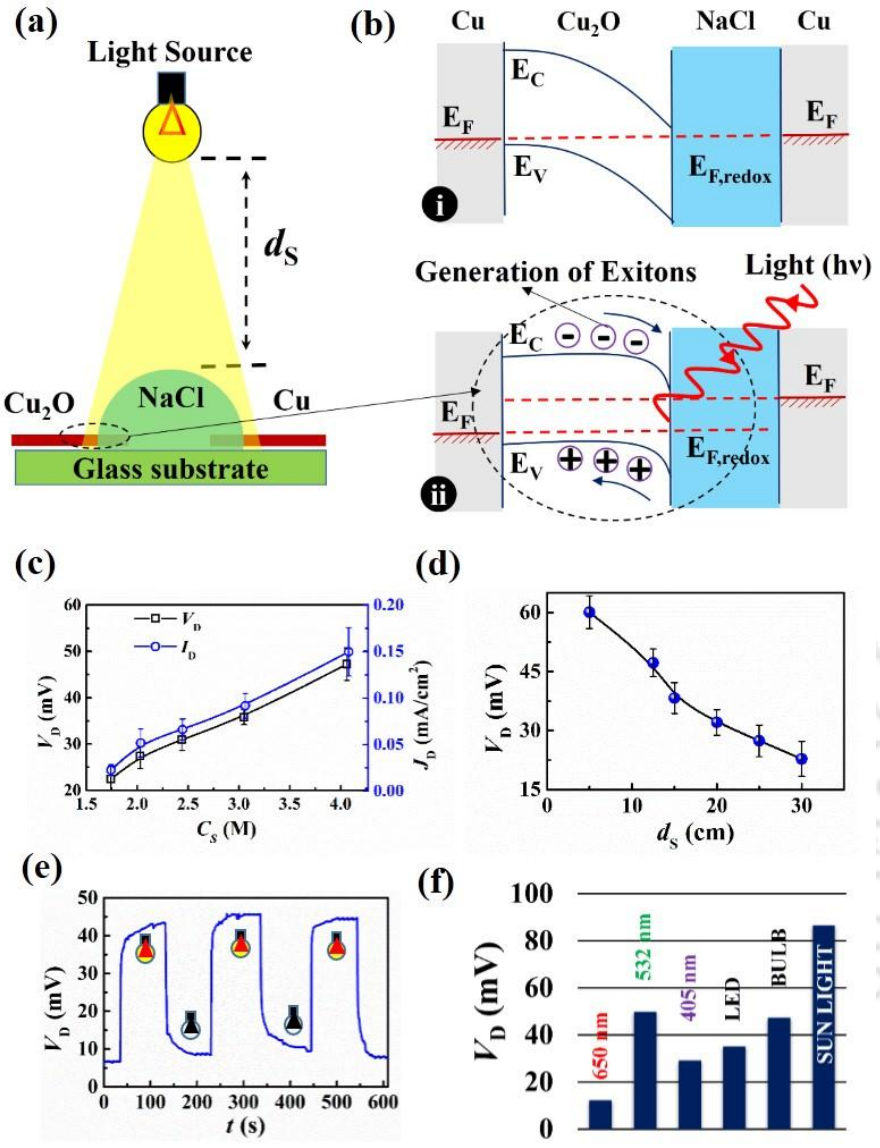

Figure 6.4: Image (a) shows the experimental set-up of a droplet energy harvester (DEH) which consists of a droplet of aqueous solution of NaCl dispensed on a glass slide in between the Cu and Cu_2O electrodes and then illuminated by a light source from the top. Image (b) schematically shows the band diagram of the configuration in presence and absence of the photo-excitations. Plot (c) shows the variations in the voltage generated (V_D) and current density (J_D) when NaCl concentration (C_s) in the droplet was varied. Plot (d) shows change in V_D as the distance between light source and droplet (d_s) was varied. Image (e) illustrates the variation in V_D when the light source was turn on and off for three consecutive cycles. Image (f) shows variation in V_D for different light source like red laser

(650 nm), green laser (532 nm), blue laser (405 nm), LED, and incandescent bulb, and solar illumination of ~24 klux.

6.2.4 Experimental methodology

Figure 6.4(a) schematically shows the setup employed for the droplet energy harvester (DEH) experiments. A water microdoplet of aqueous NaCl solution was dispensed at the junction of a pair of Cu-Cu_2O electrodes (dia. ~240 µm). Thereafter, the microdroplet was exposed to the different light sources such as the incandescent bulb (100 W, 220 V - 50Hz AC, Bajaj, India), lasers of wavelengths 650 nm, 532 nm and 405 nm (Huonje, China), and direct solar illumination. The voltage and current was measured using a digital multimeter (Mastech, India, range: 0 – 200 MΩ ± 1.0%).

The intensity of the light sources was measured with the help of a lux meter (HTC LX-101A). The concentration of NaCl in the droplet (C_s) and the distance between artificial light source and droplet surface (d_s) were optimized by evaluating the maximum potential difference obtained for a particular combination of C_s = 4 M and d_s = 12.5 cm. The distance was maintained to create ~ 4.5 kLux light intensity for all the experiments unless mentioned otherwise. In order to intensify the power generation, in some of the experiments we used bi-convex lens (6 mm diameter and 10 cm focal length) to focus solar illumination on the DEH.

The setup shown in Figure 6.4(a) was also employed for the microfluidic energy harvester (MEH) experiments with the exception that the DEH was replaced by the microchannel integrated with the Cu-Cu_2O electrodes. The methods to prepare such microchannels and their cleaning protocol before experimental use are discussed in the Section C.1 of **Appendix-C**. For MEH experiments the aqueous salt solution was flown through the

microchannel with the help of a syringe pump (Harvard Apparatus, PHD 2000) at different flow rates. The MEH experiments were also conducted under the same set of light exposure as mentioned for the DEH experiments. Again, in order to intensify the power generation, we used bi-convex lens (6 mm diameter and 10 cm focal length) to focus solar illumination on the droplet.

In order to uncover the influence of AuNPs on the power generation, we conducted the DEH and MEH experiments when the aqueous NaCl solution (4.0 M) loaded with AuNPs at different volume ratios (v/v). The AuNP laden fluid was stimulated using lasers of wavelengths 650 nm, 532 nm, and 405 nm to investigate the effect of SPR on the power generated. Additionally, AuNP laden fluid experiments were also performed with LED, 100 W bulb, and under solar illumination. The experimental setup employed to evaluate the efficiency of the proposed DEH and MEH is shown in Figure C.1 of the **Appendix-C**. The procedure to evaluate the efficiency of the different DEH and MEH prototypes are discussed in detail in Section C.2 of **Appendix-C**.

6.3 RESULTS AND DISCUSSION

Figure 6.4(a) shows the setup for the DEH experiments. The DEH setup resembled an electrochemical photovoltaic (ECPV) system composed of a glass substrate, a semiconductor p-type Cu_2O electrode, an electrolyte microdroplet of aqueous NaCl solution, and a metal Cu counter electrode. The droplet of 4 M aqueous NaCl solution was dispensed at the junction of Cu and Cu_2O electrodes before a 100 W incandescent bulb of intensity ~4.5 kLux was illuminated from a vertical distance of d_s = 12.5 cm. The bulb could generate a potential difference of ~43 mV across the Cu-Cu_2O electrodes. The control experiments performed showed that the use of a pair of Cu electrodes could not

generate any such potential difference under similar conditions. Figure 6.4(b) shows the energy band diagram of DEH, which suggest that the proposed DEH-ECPV system could develop excitons upon light illumination when the electrons from valance band of the semiconductor Cu_2O electrode jumped to the conduction band. Consequently, the electrons reduce Na+ in the electrolyte while the holes reach the Cu counter electrode through the external circuit to oxidize Cl- in the electrolyte. In long time, the reduced (oxidized) Na+ (Cl-) on the Cu_2O (Cu) electrode transferred back to the electrolyte to enable the ECPV arrangement a regenerative one.[11]

Figure 6.4(c) shows the variations in the potential difference (V_D) and current density (J_D) across the droplet for different concentrations of NaCl (C_s). The plots confirm that V_D and J_D amplified with the increase in C_s because of the enhancement in the electrical conductance of the microdroplet. Figure 6.4(d) shows that V_D enhanced significantly as the light intensity was increased by bringing in the source closer to the DEH. Figure 6.4(e) shows that the phenomenon was repeatable because a finite V_D was observed when the light source was turned 'on' and decreased when it was turned 'off' for three consecutive cycles. Importantly, Figure 6.4(f) suggest that the potential difference was maximum ~90 mV when the DEH was exposed to a direct solar illumination of intensity 24 kLux. The experiments highlighted the potential of the DEH-ECPV prototype for solar energy harvesting.

Figure 6.5 shows some simple strategies to improve the power efficiency of the DEH-ECPV system. Figure 6.5(a) shows the power density, $P_D = V_D \times J_D$, across the DEH increased with the reduction in the droplet volume (ϕ_D). The results highlight the importance of miniaturisation in improving the power density of such systems.

In this case, P_D improved since the V_D and J_D did not decrease significantly with reduced surface area of the droplet at a lower ϕ_D. Figure 6.5(b) shows that when the DEH was loaded with different proportions of AuNPs (C_{Au} - %v/v) the V_D initially increased with AuNP loading and reached a maximum value before reducing progressively. Control experiments suggested that the phenomenon was only possible when the nanoparticles of the noble metals such as AuNPs were used. For example, Figure C.2 of the Appendix-C shows that use of Ni nanoparticles led to the reduction in V_D. Figure 6.5(b) suggests that the optimum C_{Au} was found to be a ~20% (v/v) in 4 M aqueous NaCl solution for which V_D was ~100 mV when the light source was green laser.

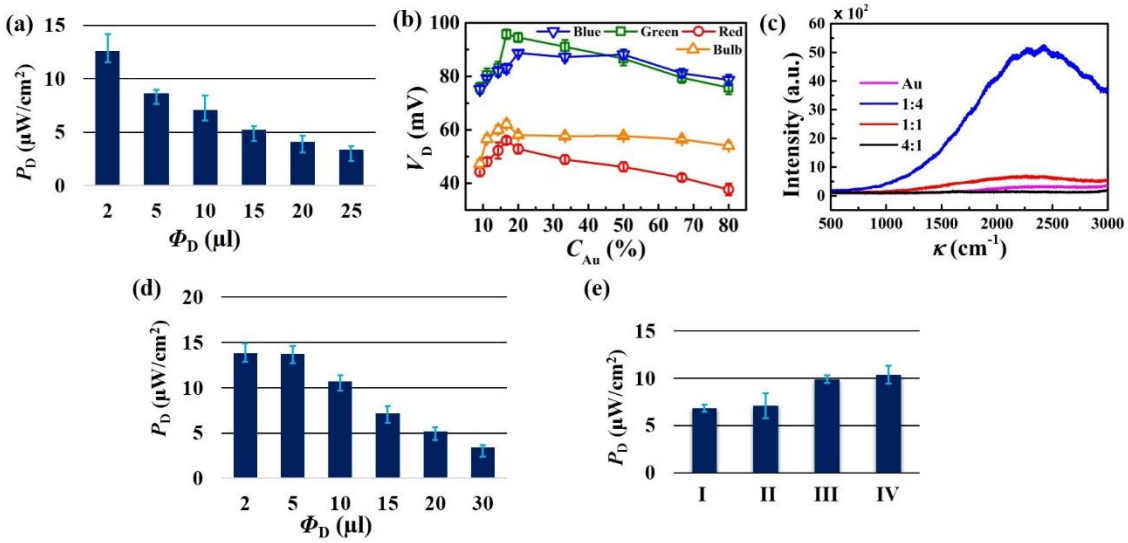

Figure 6.5: Plot (a) shows the power density (P_D) for a 4 M aqueous NaCl microdroplet of different volume (ϕ_D) under 100 W bulb when d_s = 12.5 cm. Image (b) shows variation in V_D when AuNPs were loaded inside the 4 M aqueous NaCl droplet at different proportions (C_{Au} - % v/v). The plots also suggest the influence of different light source on the same. Image (c) shows the power density in case of AuNP laden salt-water droplet of different volume (ϕ_D). Image (d) shows the P_D

for, (I) 500 µl of 4 M NaCl solution film of 1 cm x 2 cm area, (II) 4 M NaCl droplet of 10 µl, (III) 500 µl of 4M NaCl solution film of 1 cm × 2 cm area with 20% AuNP loading, (IV) 4M NaCl droplet of 10 µl with 20% AuNP loading. Image (e) shows the Raman spectroscopy of AuNP in aq. 4 M NaCl solution at different concentration. This image shows the variation in SPR for different AuNP loaded aqueous NaCl solutions. The intensity of the light was ~4.5 kLux.

Figure 6.5(c) shows the Raman spectra with 488 nm laser excitation of the AuNP loaded aqueous NaCl solution at different proportions, which confirmed maximum surface enhanced Raman scattering (SERS) when 1:4 (v/v) AuNP- aqueous-NaCl was used.[12-15] The SERS results corroborate the maximum voltage generation of the droplet composed of aqueous NaCl solution with ~20% (v/v) AuNP loading, as shown in Figure 6.5(b). The TEM images (a) – (c) in Figure C.3 of **Appendix-C** show that with increase C_{Au} the AuNPs agglomerated, which led to the reduction in the SPR.[15] The agglomeration of AuNPs was also supported by the shifting and broadening of peaks in UV-Vis spectra at higher loading, as shown in Figure C.3(d) of **Appendix-C.**

Figure 6.5(d) shows that the P_D improved significantly in case of AuNP laden DEH for a smaller ϕ_D. While, Figure 6.5(e) illustrates the variation in V_D for four different systems, (I) a film of 1 cm × 2 cm area composed of 500 µl of 4 M aqueous NaCl solution; (II) 4 M aqueous NaCl droplet of 10 µl, (III) a film of 1 cm × 2 cm area composed of 500 µl of 4 M aqueous NaCl solution with 20% AuNPs, and (IV) 4 M aqueous NaCl droplet of 10 µl with 20% AuNPs. All the systems were illuminated with 100 W bulb from 12.5 cm at ~4.5 kLux. The experiments uncovered that AuNP loaded microdroplets were more efficient in harvesting power

that the similar thin film based systems. Briefly, the Figures 6.5 shows that about 1.5- to 2-fold rise in V_D and P_D is possible with the reduction in size of the droplet and the use optimum level of AuNPs in the DEH.

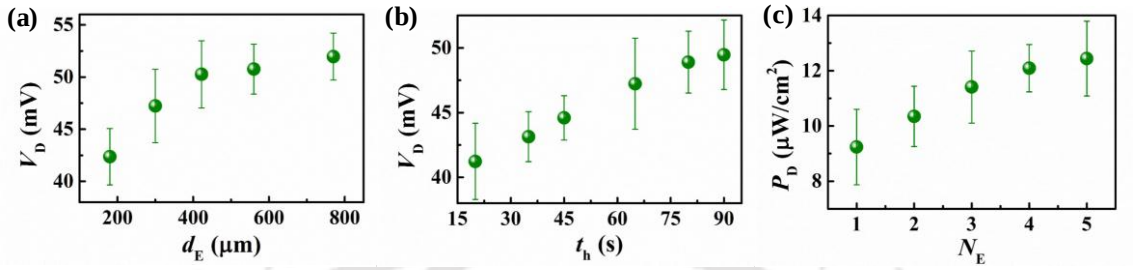

Figure 6.6: This image shows the variations in V_D with, (a) different electrode diameter (d_E), (b) different electrode heating time (t_h), and variations in P_D with (c) number of electrodes (N_E).

Figure 6.6 shows that the properties of the electrodes could play important roles in improving the V_D for the DEH-ECPV systems. Figure 6.6(a) shows the V_D increased with the diameter of the electrodes (d_E). However, the electrodes with diameter ~240 μm was used for the experiments because beyond this dimension the increase in V_D was not so profound. We also studied the effect of the time duration (t_h) for thermal heating to grow Cu_2O on the Cu electrodes. Figure 6.6(b) shows that with the increase in t_h the performance of Cu_2O-Cu system improved. The figure also suggests that heating a Cu microwire for t_h ~ 80 s could provide the optimal Cu_2O electrode. Interestingly, with the increase in the number of electrode pairs (N_E) the value of P_D also increased, as shown in Figure 6.6(c). The plot suggests that the increase in the total effective surface area of the electrodes for the charge transfer could increase efficiency of the proposed DEH-ECPV system. Further, the plot opened up the possibility of μ-VLSI through the integration of multiple electrodes under each DEH-ECPV system to extract more power.

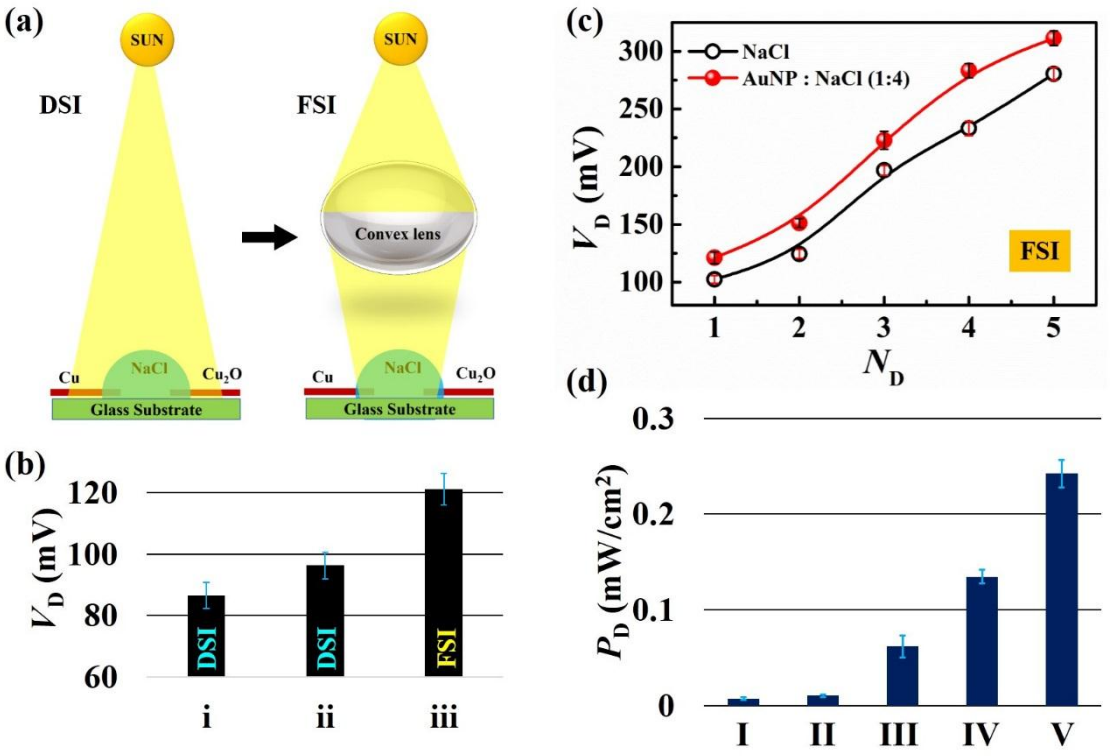

Figure 6.7: Image (a) shows the schematic diagram of the experimental set-up under direct solar illumination (DSI) and focussed solar illumination (FSI). Image (b) shows the variations in generated voltage V_D for three different conditions (i) DSI on a droplet of 4 M aq. NaCl solution, (ii) DSI on a droplet of 4 M aq. NaCl solution with 20% AuNPs, and (iii) FSI on a droplet of 4 M aq. NaCl solution with 20% AuNPs. Image (c) shows the variations in V_D under FSI with the number of DEH (N_D) composed of 4 M aq. NaCl solution and 4 M aq. NaCl solution with 20% AuNPs. Image (d) shows the variation in P_D for, (I) 4 M aq. NaCl droplet under 100 W bulb, (II) 4 M aq. NaCl droplet with 20% AuNP loading under 100 W bulb, (III) 4 M aq. NaCl droplet with 20% AuNP under green laser, (IV) 4 M aq. NaCl droplet under FSI, and (V) 4 M aq. NaCl droplet with 20% AuNP loading under FSI.

Figure 6.7 summarizes the performance of the DEH-ECPV system under direct (DSI) and focused solar illuminations (FSI), as schematically shown in the image 6.7(a). Although the response of the prototype was maximum under DSI, it could be

further enhanced by FSI on the DEH with the help of a bi-convex lens. Figure 6.7(b) shows the variations in V_D for three different conditions (i) DSI on a droplet of 4 M aq. NaCl solution, (ii) DSI on a droplet of 4M aq. NaCl solution with 20% AuNPs, and (iii) FSI on a droplet of 4M aq. NaCl solution with 20% AuNPs. While the DSI could generate about ~90 mV of potential difference, use of FSI could increase the same upto ~120 mV in presence of 20% AuNPs, as shown in Figure 6.7(b). Remarkably enough, the use of five such DEH could enhance the V_D to about 300 mV as shown in Figure 6.7(c). Figure 6.7(d) shows that, in this scenario, the use of AuNPs along with the convex lens, five units of DEH-ECPV could enhance P_D about 35 fold (from 0.007 mW/cm^2 to 0.242 mw/cm^2), which was found to be unusually high for such a simple system. Simple scale-up calculations from this plot unveil that the proposed DEH-ECPV unit could harvest ~1 W in ~0.4 m^2 area.

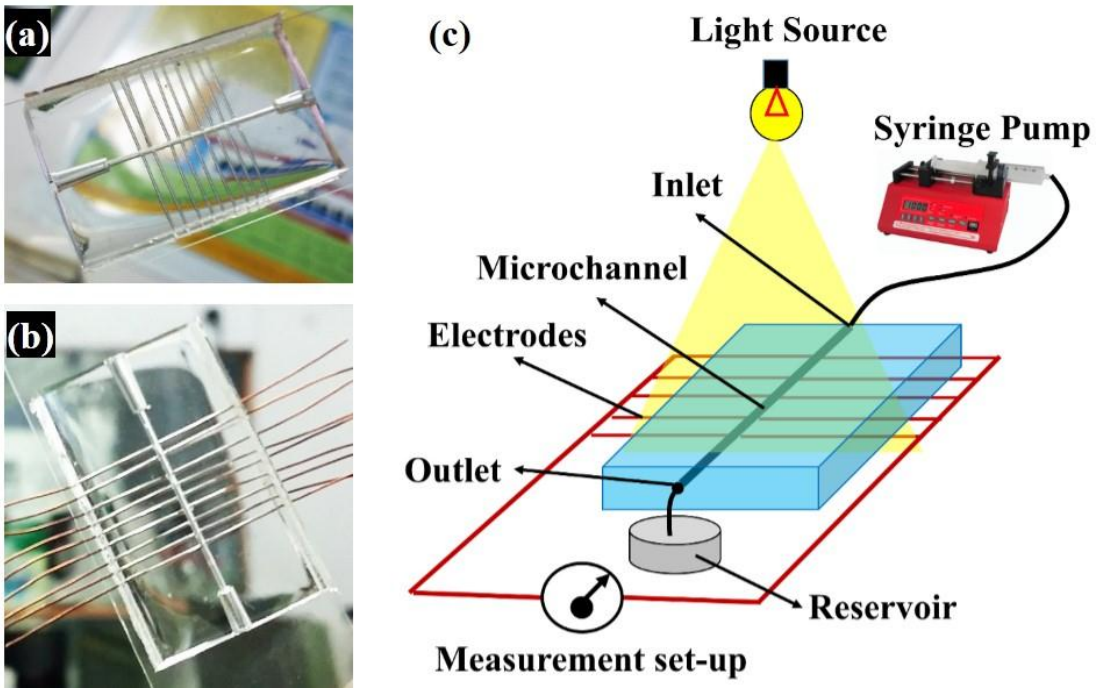

Figure 6.8: The image (a) and (b) photographs of the MEH. Image (c) shows the experimental setup for the energy harvesting employing the MEH.

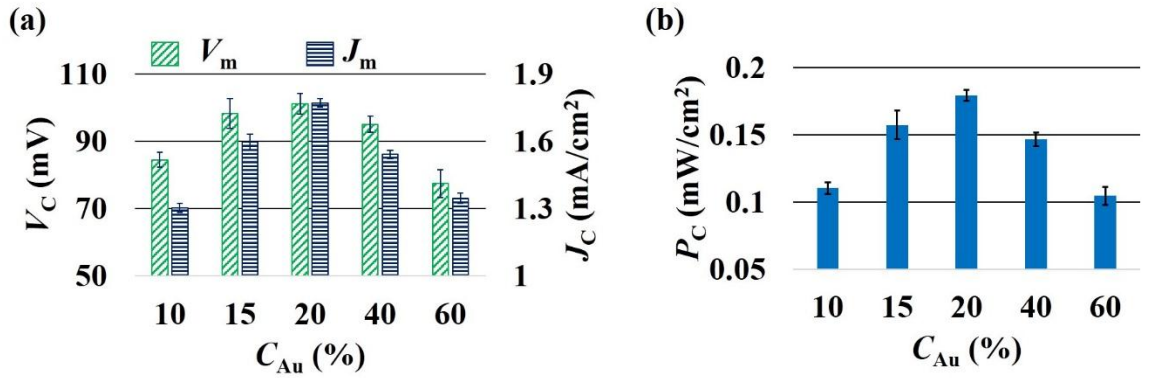

Figure 6.9: Image (a) shows the change in generated voltage (V_C) and current density (J_C) with the AuNP loading (C_{Au}) for the 9-electrode MEH. Image (b) shows the change in power density (P_C) with C_{Au} for the 9-electrode MEH. In all cases the light intensity was 1.1 kLux and F_R = 0.01 ml/min.

Interestingly, the principles of the DEH-ECPV system discussed so far could be extended to develop a microfluidic energy harvester (MEH) with enhanced efficiency. Figure 6.8 shows the typical MEH setup employed for the experiments. The Figures 6.8(a) and 6.8(b) show the photographic images of the MEH, which was composed of a transparent PDMS slab with a central channel for the flow of the electrolyte. The central channel was connected to a series of tributary channels at the sides through which the Cu electrodes were inserted at one side and the Cu_2O electrodes were inserted from the other. The images suggest that we kept the options to insert 9-pairs of electrodes in the MEH to uncover its potential for µ-VLSI. Figure 6.8(c) shows the experimental setup where the light source was illuminated from the top and a micropump was employed to enforce the electrolyte to flow through the central microchannel at different flow rates (F_R). It may be noted here that instead of pumps we also used the hydrostatic heads to flow the electrolytes and found similar results as reported later. We employed two types of

electrolytes to flow through the channel, (i) 4 M aq. NaCl and (ii) 4 M aq. NaCl loaded with AuNPs. The Figures 6.9(a) and 6.9(b) suggest that even for the 9-pair electrode MEH the 20% (v/v) AuNPs with aq. NaCl solution was optimal.

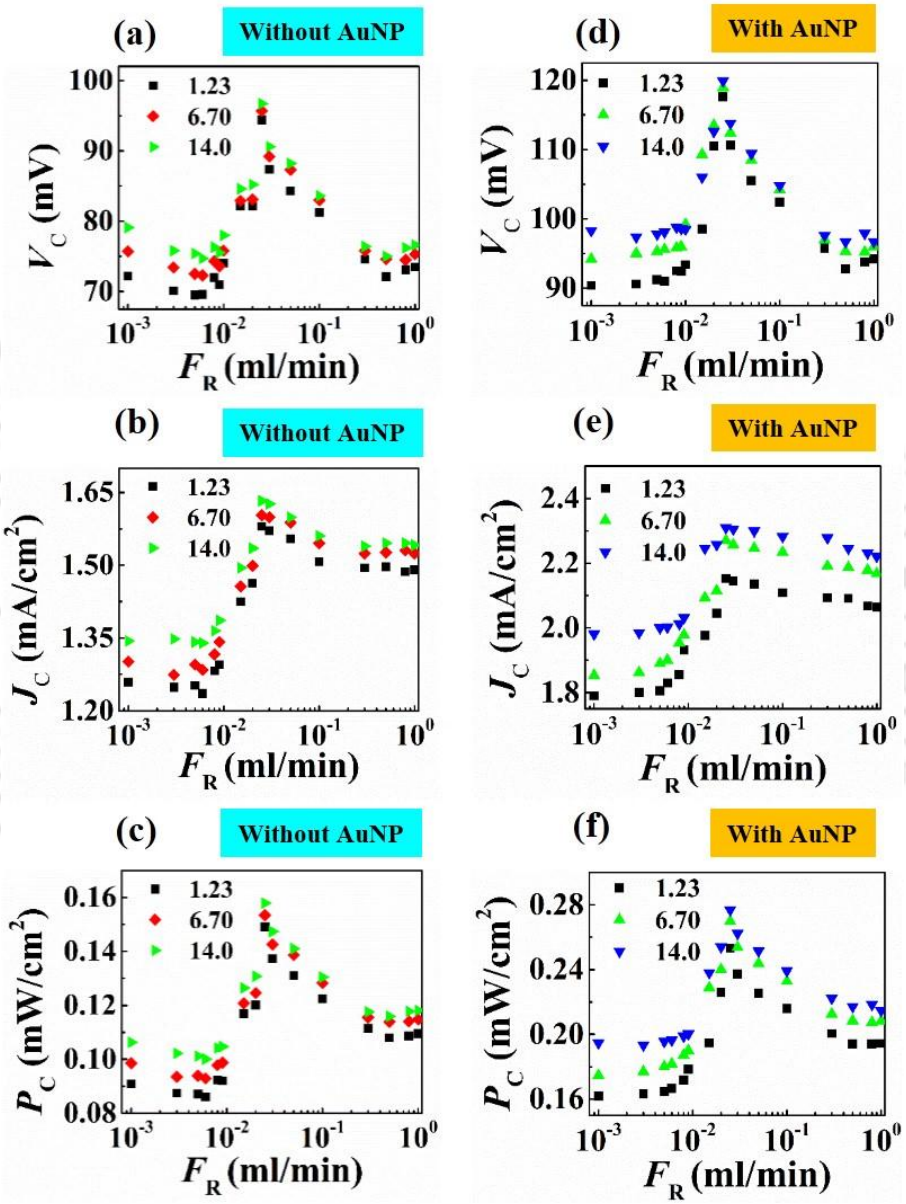

Figure 6.10: Images (a) – (c) [(d) – (f)] show the variations in the voltage generated (V_C), current density (J_C), and power density (P_C), respectively, with the flow rate (F_R) of the electrolyte 4 M aq. NaCl solution [4 M of aq. NaCl solution with 20% (v/v) AuNPs] in the MEH-ECPV setup. The square (■), diamond (♦), and triangle (▲) symbols on the images (a) – (f) represent light intensities of 1.23 kLux, 6.7 kLux, and 14 kLux, respectively.

Figures 6.10(a) – 6.10(c) show the variations in the voltage generated (V_C), current density (J_C), and power density (P_C), in the MEH with F_R when 4 M aq. NaCl solution was flown. In these experiments, we inserted all 9-pair of electrodes for the experiments. The Figures 6.10(d) – 6.10(f) show similar plots as shown in Figures 6.10(a) – 6.10(c) when the 4 M aq. NaCl solution loaded with AuNPs [20% (v/v)] was flown. The plots suggest that V_C, J_C, and P_C values were similar to the DEH at the smaller values of F_R before reaching a maximum (denoted as, V_{Cm}, J_{Cm}, and P_{Cm}) at the intermediate values of F_R. However, with further increase, beyond a threshold value of F_R the magnitudes of V_C, J_C, and P_C reduced. The plots reveal that the MEH could show significant improvement in enhancing V_C, J_C, and P_C as compared to the DEH at moderately high values of F_R. From the plots we evaluated the optimum flow rate for energy harvesting as, F_R ~0.025 ml/min. Further, as observed for DEH, the magnitudes of V_C, J_C, and P_C could be amplified significantly with the use of optimal AuNP loading and increase in the intensity of light exposure.

The enhancement of the V_C, J_C, and P_C with F_R could be attributed to the generation of streaming potential (V_{SP}) across the electrodes, when the electrolyte was forced through the channel. The contact of the Cu and Cu_2O electrodes with the electrolyte ensured that the electrical double layers were generated around them. In consequence, the Cu and Cu_2O electrodes developed a difference in ζ-potentials, which led to an additional voltage generation in the MEH prototype apart from the ones induced by the excitations from photon and SPR on the AuNPs. The V_{SP} in the MEH increased with the pressure drop and flow rate, which is perhaps one of the very simple way to enhance the streaming potential of a system. At higher F_R,

perhaps a partial destruction of the double layer due to the flow led to the reduction in the voltage generation. However, even at higher F_R the MEH could generate larger V_C as compared to the situation when the fluid was stationary.

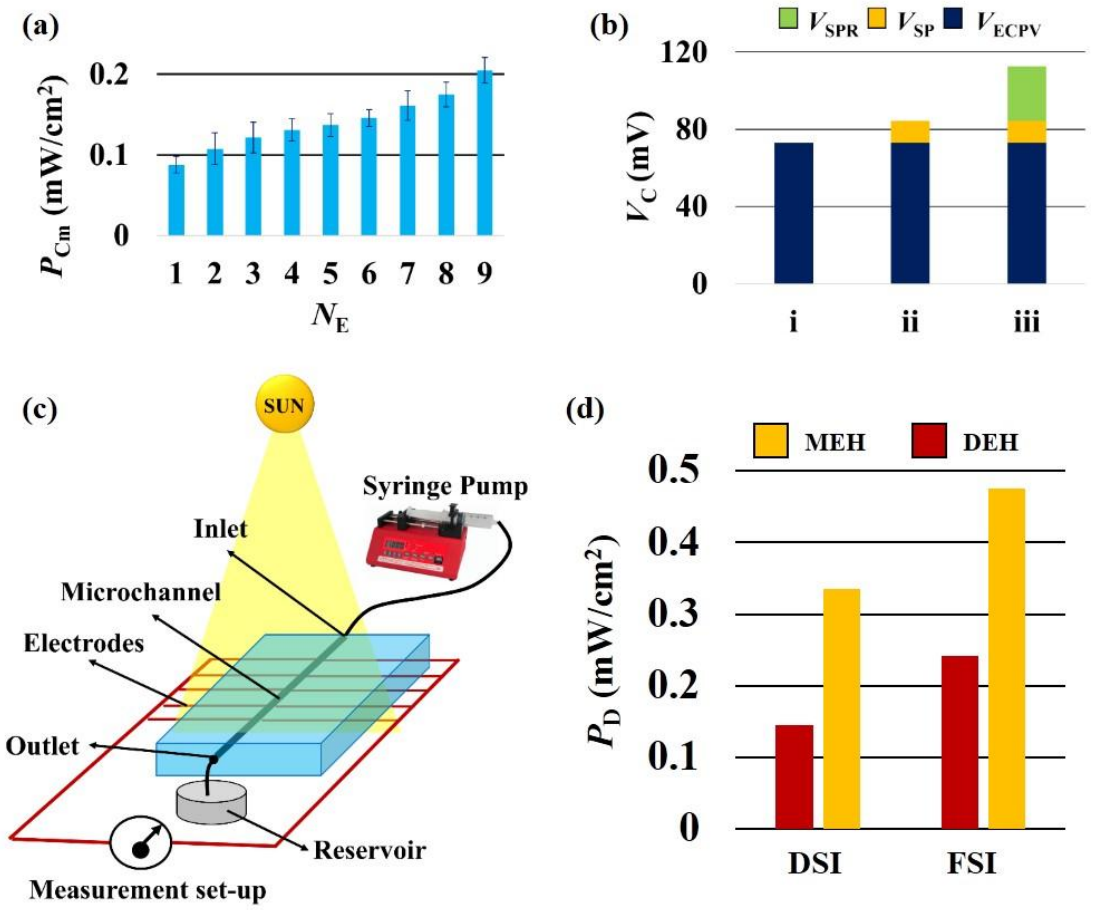

Figure 6.11: Image (a) shows the change in P_{Cm} with number of the pair of Cu-Cu_2O electrodes (N_E) for a 4 M aq. NaCl solution with AuNPs. Image (b) shows the potential difference generated (V_C) because of the ECPV (V_{ECPV}), SPR (V_{SPR}), and streaming potential (V_{SP}) for the 9-electrode MEH. In all cases the light intensity was 1.1 kLux and F_R = 0.025 ml/min. Image (c) shows the schematic diagram of the MEH setup under DSI. Image (d) illustrates the comparison between power densities (P_D) of MEH and DEH under DSI and FSI.

In order to improve the performance of the MEH, experiments were conducted with varying the number of electrodes (N_E) at a fixed light intensity of 1.1 kLux for the

electrolyte 4 M aq. NaCl solution with AuNPs flowing at F_R = 0.025 ml/min. Figure 6.11(a) shows that the P_{Cm} increased with N_E, which confirmed that a μ-VLSI of electrodes across the central microchannel could enhance the P_{Cm} of the MEH system. In order to identify the individual contribution of the ECPV (V_{ECPV}), SPR (V_{SPR}), and SP (V_{SP}) inside the MEH, we performed a set of control experiments. The V_{ECPV} was identified when a stationary 4.0 M aq. NaCl solution inside MEH with 9-pair electrodes was exposed to the light. The V_{SP} was identified by flowing a 4.0 M aq. NaCl solution at a F_R = 0.025 ml/min to generate (V_{ECPV} + V_{SP}) and then subtracting the magnitude of the V_{ECPV} obtained from the previous experiment. The V_{SPR} was identified by flowing a 4.0 M aq. NaCl solution loaded with AuNPs at a F_R = 0.025 ml/min to generate (V_{ECPV} + V_{SP} + V_{SPR}) and then subtracting the sum of V_{ECPV} and V_{SP} from the same. Figure 6.11(b) shows the magnitudes of the V_{SP} = 15 mV, V_{ECPV} = 76 mv, and V_{SPR} = 27 mV from these experiments. The MEH was further tested under solar illumination as shown in Figure 6.11(c). The power density of the MEH is found to be ~2 times compared to DEH under DSI and FSI as illustrated in Figure 6.11(d). The experiments suggest that MEH system could harvest ~1 W in ~0.2 m^2 area.

Figure 6.12 shows that the potential difference generated by the DEH and MEH prototypes could also be evaluated with the help of simple theoretical calculations. Figure 6.12(a) shows the schematic a single unit cell of MEH composed of a microchannel of diameter, *d*, and length, *L*. We assumed the electrode distance to be similar to, *d*. In such a situation, the V_{SP} can be expressed as,

$$V_{SP} = \frac{128\varepsilon_r \varepsilon_o \zeta L F_R}{\pi d^4 K_L} \quad (6.3.1)$$

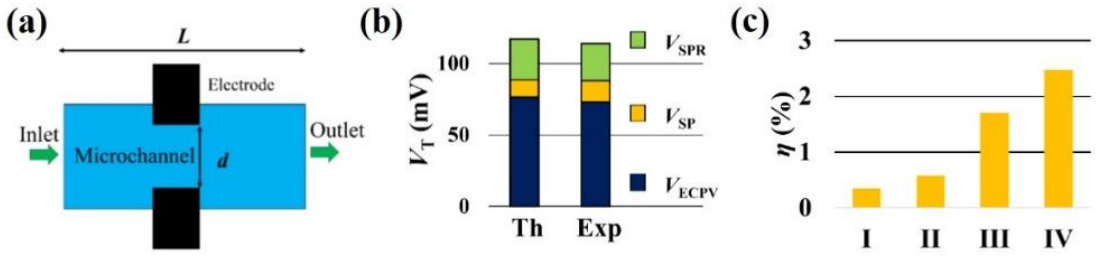

Table: 1 Systems	V_{OC} (mV)	J_{SC} (mA/cm²)	V_m (mV)	J_m (mA/cm²)	FF %	η %
I. Salt-water DEH (DEH-S)	23.4	0.80	14.2	0.48	36.41	~0.09
II. Salt-water DEH with AuNPs (DEH-SA)	33.4	1.3	21.2	0.89	43.45	~0.26
III. MEH with Stationary Salt-water (MEH-S)	68.6	0.91	42.4	0.60	40.75	~0.35
IV. MEH with Flowing Salt-water (MEH-SF)	79.4	1.17	48.0	0.86	44.43	~0.56
V. DEH-S Loaded with AuNPs under FSI	117.6	2.3	80.3	1.91	56.70	~0.80
VI. MEH-SF with AuNPs	109.1	4.35	88.9	3.52	65.93	~1.63
VII. MEH-SF loaded with AuNPs under FSI	128.3	5.51	114.1	4.17	67.30	~2.48

Figure 6.12: Image (a) schematically shows the theoretical domain chosen for the calculations with a microchannel of length, *L*, having a pair of electrodes separated by a distance, *d*. Image (b) shows the comparison between the experimental (Exp) and theoretically (Th) values of the V_{SP}, V_{SPR}, and V_{ECPV}. Image (c) shows the efficiencies of the different MEH systems: (I) the salt-water electrolyte was stationary; (II) when the salt-water electrolyte was flown at F_R = 0.025 ml/min; (III) when the salt-water electrolyte with suspended AuNPs (20% v/v) was flown at F_R = 0.025 ml/min; and (IV) when the salt-water electrolyte with suspended AuNPs (20% v/v) was flown at F_R = 0.025 ml/min under FSI. Table I summarizes the values of different efficiency parameters for both DEH and MEH discussed in the present work: (I) salt-water DEH (DEH-S); (II) salt-water DEH with AuNPs (DEH-SA); (III) MEH with stationary salt-water (MEH-S); (IV) MEH with flowing salt-water at optimum flow rate (MEH-SF); (V) DEH with salt-water (DEH-S)

loaded with AuNPs and under FSI; (VI) MEH with flowing salt-water (MEH-SF) with AuNPs; and (VII) MEH with flowing salt-water loaded with AuNPs and under FSI.

Here, the length of the channel (L) was 0.05 m, effective diameter of the channel (d) was 10^{-4} m, the specific electrical conductivity (K_L) of the electrolyte was 0.015 S m^{-1}, the flow rate of the electrolyte (F_R) was 0.025 ml/min, dielectric constant of water (ε_r)was 80, dielectric permittivity of free space (ε_o) was 8.854×10^{-12} F m^{-1}, and the ζ -potential of the electrodes (ζ) were 0.03 V. Plugging the values into the Eq. (6.3.1) we obtained the theoretical value for, V_{SP} = 12.04 mV, as shown in Figure 6.12(b). The value obtained was very close to the experimental value of 15 mV, as shown in Figures 6.11(b) and 6.12(b). Further, the V_{ECPV} was calculated employing the expression,

$$V_{ECPV} = \frac{nkT}{q} \ln\left(\frac{I_{Ph}}{I_D} + 1\right) \tag{6.3.2}$$

where the ideality factor (n) was chosen as 1, Boltzmann constant (k) was 1.38×10^{-23} m^2 kg s^{-2} K^{-1}, the absolute temperature (T) was 300 K, charge of electron (q) was 1.6×10^{-9} C, the current in presence of light (I_{ph}) was 5.4 μA, and the current in the dark (I_D) was 0.3 μA. Putting these values into the Eq. (6.3.2) we obtained the theoretical value for the V_{ECPV} = 76.5 mV, which was very close to the experimental value of 73 mV, as shown in Figures 6.11(b) and 6.12(b).

The enhancement of potential due to SPR was theoretically evaluated from the expression,

$$V_{SPR} = \eta_{abs} V_{ECPV} \tag{6.3.3}$$

where fraction of optical absorption increased due to SPR (η_{abs}) was taken as 0.4. An absorption spectroscopy for a constant volume of AuNPs provided the average absorption ~40% when the AuNP loading in the electrolyte was ~20% (v/v). Thus, the theoretical potential difference because of SPR was found to be V_{SPR} = 30.6 mV, which was again found to be very similar to the experimentally obtained, 27 mV, as shown in Figures 6.11(b) and 6.12(b). Combining all the aforementioned theoretical potentials we obtained the total theoretical value $V_{Th.} = V_{SP} + V_{ECPV} + V_{SPR}$ = 119.1 mV, which could be generated by the MEH. Again, the magnitude of $V_{Th.}$ was found to be very close to the experimental one, $V_{Ex.} = V_{SP} + V_{ECPV} + V_{SPR}$ = 115 mV, as shown in Figure 6.11(b) and 6.12(b).

The fill-factor (*FF*) and power efficiency (η) were evaluated for the DEH and MEH employing the expressions,

$$FF = \left(\frac{V_m \times J_m}{V_{OC} \times J_{SC}} \right) \times 100\% \tag{6.3.4}$$

$$\eta = \frac{P_{out}}{P_{in}} = \frac{V_{OC} \times I_{sc} \times FF}{P_{in}} = \frac{P_{Dout}}{P_{Din}} \tag{6.3.5}$$

where V_{OC}, J_{SC}, V_m, J_m, P_{out}, P_{in}, P_{Dout}, and P_{Din} denote open-circuit voltage, short-circuit current density, voltage corresponds to maximum power, current density corresponds to maximum power, output power, input power, output power density, and input power density, respectively. The P_{Din} was calculated from the lux value which is measured using a lux meter where 1 lux was 1 lumen/m^2. The luminous efficiency of a 100 W incandescent bulb was ~15 lumen/W, which was used to calculate the optical flux ~0.067 W/m^2. The light source intensity was of ~1100 lux = 73.7 W/m^2, which led to the input power density, P_{Din} = 73.7 W/m^2. The output

power density, $P_{Dout} = V_m \times J_m$ where, V_m and J_m was the voltage and current density corresponds to maximum power, which was obtained from the J-V curve. Figure 6.12(c) shows the typical variations in the power efficiency (η) for the MEH where, (I) the salt-water electrolyte was stationary; (II) when the salt-water electrolyte was flown at an optimum F_R; (III) when the salt-water electrolyte with suspended AuNPs (20% v/v) was flown at an optimum F_R; and (IV) when the salt-water electrolyte with suspended AuNPs (20% v/v) was flown at an optimum F_R and the light was focused using a bi-convex lens. Clearly, the table summarize the use of the combined influences of electrochemical photovoltaics, surface Plasmon resonance, and streaming potential could increase the efficiency of the device up to 2.48%, which is among the highest reported so far employing the Schottky barrier energy harvesters.

Table I in Figure 6.12 shows the typical experimentally obtained V_{OC}, J_{SC}, V_m, J_m, FF, and η values for the DEHs and MEHs considered in this work. The Table suggest that while DEH with salt water could show only 0.1% efficiency, it enhanced by about 2.5-folds to 0.24% with the use of the SPR from the AuNPs. Further, flowing this electrolyte at an optimal flow rate through the MEH could increase the efficiency of by about 6-folds to ~1.63%. Finally, focussing the light source into the MEH, undergoing a flow of AuNP laden salt electrolyte at an optimal flow rate, led to an additional 1.5-fold increase in efficiency to ~2.5%.

6.4 SUMMARY

In this chapter, we demonstrate that a microdroplet of aqueous salt solution could electrochemically harvest energy from various light sources including the solar

irradiation when placed on a pair of Schottky barrier Cu-Cu_2O electrodes. Introduction of gold nanoparticles inside the microdroplet improved the power density and the efficiency of the energy harvested due to the inclusion of the effects of surface Palsmon resonance alongside the electrochemical photovoltaics. Use of focussed solar illumination through lens for five such microdroplets showed ~30-fold enhancement of the power density and ~7-fold increase in the efficiency, which opened up the possibility to harvest high density of power employing a very large scale integration of such systems. Remarkably enough, flowing the nanoparticle laden slat solution inside a microfluidic energy harvester integrated with the Cu-Cu_2O electrodes could harvest energy at an efficiency of ~2.5%, which is perhaps the highest reported so far employing the Schottky barrier energy harvesters. In this situation, the combined effects of the streaming potential due to the flow, surface Pasmon resonance due to the nanoparticles and the electrochemical photovoltaics led to the increase in the efficiency under a focussed illumination of the light source on the microfluidic energy harvester. The power density of the microfluidic device could be increased by a factor of ~13 with the use of multiple Cu-Cu_2O electrodes, which opened up the possibility of VLSI of such systems for high density energy harvesting. While an array of droplet systems could harvest solar energy at a higher efficiency, the microfluidic setup integrated with a large collection of electrodes could harvest hydel power when integrated any hydrostatic head generating flow equivalent to the pump.

6.5 ACKNOWLEDGEMENTS

We thank DST Nano-Mission program, grant no. SR/NM/NS-1109/2012(C), DEITY grant no. 5(9)/2012-NANO, and FIST-grant no. SR/FST/ETII-028/2010,

Government of India, for financial aids. We also gratefully thank the support from Central Instrumental Facility, IIT Guwahati for the access to the characterization facilities. Contributions from Mr. Amit Kumar Singh and Mr. Mitradip Bhattacharjee are also gratefully acknowledged.

6.6 REFERENCES

1. D. Tahir and S. Tougaard, Journal of Physics: Condensed Matter **24**, 175002 (2012).
2. D. S. Murali, S. Kumar, R. Choudhary, A. D. Wadikar, M. K. Jain, and A. Subrahmanyam, AIP Advances **5**, 047143 (2015).
3. I. S. Brandt, C. A. Martins, V. C. Zoldan, A. D. C. Viegas, J. H. Dias da Silva, and A. A. Pasa, Thin Solid Films **562**, 144 (2014).
4. S. K. Ghosh and T. Pal, Chemical Reviews **107**, 4797 (2007).
5. H. Choi *et al.*, Nature Photonics **7**, 732 (2013).
6. D. Schaadt, B. Feng, and E. Yu, Applied Physics Letters **86**, 063106 (2005).
7. J. H. Im *et al.*, Nano Letters **15**, 2120 (2015).
8. S. Pillai, K. Catchpole, T. Trupke, and M. Green, Journal of Applied Physics **101**, 093105 (2007).
9. K. Nakayama, K. Tanabe, and H. A. Atwater, Applied Physics Letters **93**, 121904 (2008).
10. M. N. Martin, J. I. Basham, P. Chando, and S. K. Eah, Langmuir **26**, 7410 (2010).
11. A. J. Nozik and R. Memming, The Journal of Physical Chemistry **100**, 13061 (1996).
12. M. Moskovits, Reviews of Modern Physics **57**, 783 (1985).
13. V. Amendola, S. Scaramuzza, S. Agnoli, S. Polizzi, and M. Meneghetti, Nanoscale **6**, 1423 (2014).

14. M. K. Hossain, Y. Kitahama, G. G. Huang, T. Kaneko, and Y. Ozaki, Applied Physics B **93**, 165 (2008).

15. G. Wang and W. Sun, The Journal of Physical Chemistry B **110**, 20901 (2006).

Chapter 7

Conclusions and scope for future work

7.1 CONCLUSIONS

A detailed study on the morphologies of the multiphase gas-liquid and liquid-liquid system in microchannel has been explored. The thesis is initiated with the development of a flow pattern predictor for gas-liquid and liquid-liquid systems inside the microchannels. Thereafter, a series of experiments and simulations were performed to identify the possibility of miniaturization of various pressure-driven flow structures inside a microchannel with fine tuning of flow velocity, interfacial tension and viscosity. Further, microdroplets obtained from the pressure-driven flows were broken down to smaller ones with the help of applied electric field through various mechanisms. The experiments were also corroborated by numerical simulations in order to get a detailed insight of various flow features. The knowledge and understanding gathered from the studies of pressure and field driven microfluidics have been utilized to transform a droplet energy harvester into a microfluidic energy harvester. Finally, we could develop a proof-of-concept prototype of a microfluidic based energy harvester, which showed significant potential in supplying power to the modern portable devices. The major conclusions from each of the chapters are discussed below.

7.1.1 Prediction of flow patterns using neural network

The study in the present chapter developed a probabilistic neural network (PNN) for prediction of flow patterns and their transition boundaries in the range of microchannel for both gas-liquid and liquid-liquid flows. The PNN was trained with various input parameters such as superficial velocities of both phases, channel inclination, interfacial tension, density difference and viscosity ratio of phases. Overall, the PNN showed high accuracy in prediction for the tube diameter of 530 – 50 μm for gas-liquid flow. The flow

patterns predicted were compared with its corresponding literature data and found to be in good agreement for all flow patterns except for liquid lump flow. This was because of less number of data available for this flow pattern in literature. The transition boundaries obtained from predicted flow pattern maps were also compared with analytical models. The percentage accuracy of PNN has been found to be higher than the same obtained from various analytical models. The accuracy of PNN prediction was also higher than the Weber number model. This PNN prediction could further be improved by incorporating larger sets of data for those flow patterns (such as, liquid-lump flow) where the prediction accuracy was quite low.

While the prediction for liquid-liquid flow patterns were also been accomplished in similar fashion. Overall, the PNN showed high prediction accuracy (~ 91.46 %) but due to lack of enough of data for some flow patterns, it showed few mismatching. The accurate prediction of flow patterns for liquid-liquid system will need huge collection of data at various microchannel diameters. Due to unavailability of data in vast numbers, we leave the detailed study on the prediction of liquid-liquid flow system for future scope.

7.1.2 Capillary force mediated flow-patterns of oil-water microflows

In this chapter, a combined experimental and computational study uncovered the effects of interfacial tension and viscosity on the flow patterns and pressure drop characteristics of an oil-water flow inside ‘T’ shaped microchannels. The important conclusions are as follows:

Transitions from slug, to plug, to droplet, to core-annular, to stratified flow patterns were obtained by tuning the oil-water interfacial tension. Progressive reduction in interfacial tension at a constant oil-to-water flow ratio transformed big slugs into smaller plugs, and

plugs into smaller droplets. The simulations uncovered a non-monotonic and nonlinear reduction in pressure drop with a decrease in interfacial tension. The change in pressure drop could be directly correlated to the frequency of the slug, plug, or droplet flow patterns at the outlet. The transitions from dripping to jetting mechanism of water droplet ejection at the inlet were also associated with some distinctive pressure drop change across the channel.

The study also identifies the pathways to miniaturize the flow structures, which enables the availability of a higher surface-to-volume ratio for the flow patterns inside microfluidic devices. At considerably lower values of the water-to-oil flow and water-to-oil viscosity ratios, droplet flow patterns could emerge when the magnitude of the oil-water interfacial tension was moderately low. Importantly, the study indicates that reducing the interfacial tension to extremely smaller values might not always be useful for microfluidic applications, because this could lead to stratified flow patterns with lower surface-to-volume ratios than the targeted droplet flow patterns. The reported transitions of the flow patterns and the subsequent pressure drop characteristics can be significant in improving the efficiency of future microfluidic devices.

7.1.3 Electric field mediated spraying of miniaturized droplets

The work in the present chapter uncovers the behavior of a water droplet flowing inside an oil medium and exposed to an external electrohydrodynamic (EHD) field inside a microchannel. The important conclusions are:

(i) When the external field intensity was weaker, both experiments and simulations showed similar shape in deformation of the droplet at different electric field intensities. The deformation trends predicted from leaky dielectric model (LDM) was found to

match with the experimental and simulated results at low field intensities ($Bo_e < 0.1$). While, the experimental and simulated deformations were found to be comparable up to moderately high field intensities.

(ii) At moderately high electric field intensities, the droplet could be split into a pair of charged droplets, which underwent periodic bridging and breakup as they translated out of the domain with electric field exposure. While the electrostatic attraction between the charged droplets led to the bridging, the capillary instability at the bridging point with sharp curvature caused the breakup.

(iii) At higher field intensities, we observed a unique phenomenon of secondary droplet ejection from the primary droplet, mimicking the electrospraying process. A droplet of 214 μm was broken down to a near monodisperse collection of droplets with minimum (maximum) diameter of 10 (18) μm forming water in oil microemulsion near the cathode region when the field intensity was significantly high. The droplet size could be tuned by changing the external field intensity. There is a possibility that the experiments reported here could indeed produce nanoscopic flow patterns, which is kept as a future scope of research work.

Concisely, a non-invasive pathway was proposed to transform a water microdroplet into a string of miniaturized ones only by tuning the external field intensity across a simple microchannel. The results can be of significance in the development of droplet microfluidic devices targeted for the applications such as microscale emulsifiers, reactors, and flow cytometers, among others.

7.1.4 Electric field mediated droplet splitting in microchannels

In this chapter, numerical simulations corroborated by the experiments have shown some interesting electric field induced disintegration of a water droplet into several miniaturized ones inside a straight microchannel with the ingenious application of discrete electric fields of variable intensity at multiple locations. The major conclusions from the study are as follows,

(i) Strategic placement of a pair of electrodes in the downstream of the channel could engender a fission mode of droplet splitting in which a bigger microdroplet was split into three smaller ones. Repeated application of such electric fields at the downstream of the microchannel showed the onset of the cascade mode in which a single droplet could be fragmented into three, five, and seven smaller microdroplets when the electric field was generated in one, two, and three different locations, respectively, having different intensities. The cascade mode shows a systematic way to disintegrate a microdroplet into many smaller ones with the help of localized Maxwell's stresses generated at the oil-water interfaces.

(ii) A transition from cascade/fission to Rayleigh mode was observed for the droplets with lower interfacial tension when the oil flow rate and the intensity of the localized field were significantly higher. While the electric field helped in elongating the droplet in the normal direction of the flow, the oil flow helped in deforming, necking, and disintegration of the elongated droplet to facilitate the Rayleigh instability for droplet breakup. Remarkably, in such a scenario, a microdroplet could be broken into 40 or more parts having minimum size ~30 times smaller than the initial one. The Rayleigh mode showed an interesting pathway to rapidly disintegrate a microdroplet into an array of miniaturized ones,

which can be useful for enhanced mass, energy and momentum transfer. The water-in-oil emulsion produced in the downstream of such channels showcase a single step method to produce microemulsion inside the straight microchannels.

7.1.5 Microfluidic energy harvester

In this chapter we demonstrate a microdroplet of aqueous salt solution that could electrochemically harvest energy from various light sources including the solar irradiation when placed on a pair of Schottky barrier Cu-Cu_2O electrodes. Introduction of gold nanoparticles inside the microdroplet improved the power density and the efficiency of the energy harvested due to the inclusion of the effects of surface Palsmon resonance alongside the electrochemical photovoltaics. Use of focussed solar illumination through lens for five such microdroplets showed ~30-fold enhancement of the power density and ~7-fold increase in the efficiency, which opened up the possibility to harvest high density of power employing a very large scale integration of such systems.

Remarkably enough, flowing the nanoparticle laden slat solution inside a microfluidic energy harvester integrated with the Cu-Cu_2O electrodes could harvest energy at an efficiency of ~2.5%, which is perhaps the highest reported so far employing the Schottky barrier energy harvesters. In this situation, the combined effects of the streaming potential due to the flow, surface Pasmon resonance due to the nanoparticles and the electrochemical photovoltaics led to the increase in the efficiency under a focussed illumination of the light source on the microfluidic energy harvester. The power density of the microfluidic device could be increased by a factor of ~13 with the use of multiple Cu-Cu_2O electrodes, which opened up

the possibility of VLSI of such systems for high density energy harvesting. While an array of droplet systems could harvest solar energy at a higher efficiency, the microfluidic setup integrated with a large collection of electrodes could harvest hydel power when integrated any hydrostatic head generating flow equivalent to the pump.

7.2 FUTURE SCOPE OF RESEARCH

The works in the present thesis can be extended in many different ways. Some of the interesting configurations, which remains to be explored, are as follows:

(i) The work in Chapter 2 showed how probabilistic neural network was employed as a first hand flow pattern indicator for gas-liquid and liquid-liquid systems. However, due to lack of data for liquid-liquid systems the PNN model showed some mismatching. This could be improved by incorporating higher number of data during training. A comparative study on the prediction accuracy of different types of neural networks for liquid-liquid flow systems are yet to be done.

(ii) In Chapter 3, with the help of experiments and simulations we showed the effect of flow velocity ratios, interfacial tension and viscosity of phases on the transition and formation of oil-water flow morphologies in a straight T-junction microchannel. One of the immediate extension could be the study of flow morphologies in a microchannel with contraction and expansion chambers. Also, the effect of reduction in channel diameter on the flow morphologies of oil-water systems is still an open area of research.

(iii) In Chapter 4, we showed a droplet flowing inside a microchannel undergoes deformation, splitting and spraying into smaller size microdroplets at various electric

field intensities. While, numerical simulations in Chapter 5 proposes the cascading mode of droplet splitting where strategic placement of multiple electrodes along the downstream of microchannel could split a droplet multiple times resulting in even smaller microdroplets. An experimental study of cascading mode of droplet breaking phenomena is still an open area of research. Alongside, a detailed parametric study of the effect of electric field intensity, initial droplet size, diameter of microchannel, length of electrode and gap between the electrodes, for the droplet size distribution is left for future scope of study.

(iv) In Chapter 6 we developed a proof of concept prototype of a microfluidics based energy harvester where electrolyte was flown along a straight channel fitted with Cu-Cu_2O electrodes, which upon illumination with light, a generation of voltage was observed. The present study proposed a system which utilizes Cu_2O as an active material employing both streaming potential and surface Plasmon resonance in addition to electrochemical photovoltaic to enhance the power density as well as efficiency of the system. Although the present efficiency of the system is ~2.48 % which is quite high as compared to the other energy harvesters of this kind but still there is always a scope of improvement. This could be achieved by substituting the active material Cu_2O by other efficient materials, which has the capacity to generate higher power density. Moreover, the generated power density can also be improved by modifying the channel geometry to increase the internal light reflection which in turn can increase the efficiency.

APPENDIX – A

A.1 Identification of dispersed phase

The flow patterns in **Chapter 3** were identified from video recording made by a high definition handycam (HDR-XR160E, Sony) and the images were extracted from the recorded video for each experiments. No, microscope were employed to capture the image of flow patterns shown in this chapter.

To identify the wall wetting fluid, a few experiments were performed with dyed oil phase. The oil phase was dyed with iodine which became reddish in color. A representative photograph of the plug flow of such system is shown in the Figure A1. The figure clearly shows that oil phase acts as wall wetting fluid and continuous phase whereas water phase is dispersed into the oil phase.

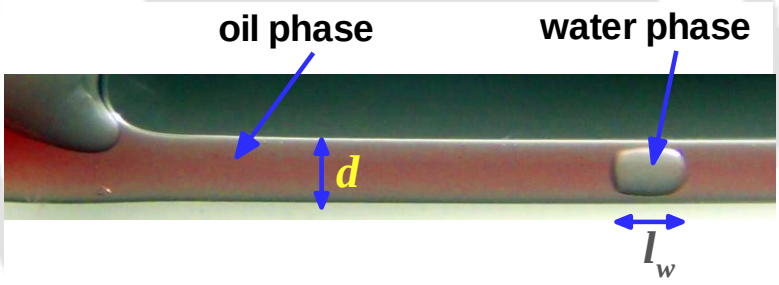

Figure A.1: Plug flow at $Q_r = 0.1$. Here, red phase is iodine added oil.

The differentiation was made based on slug/ plug lateral widths (l_w). If,

$d < l_w < 1.3d$ then, plug flow, and

$l_w > 1.3d$ then slug flow. Here, d = diameter of channel.

Table A.1: Dimensionless numbers associated with different figures.

Experimental							Computation					
Sl. No.	Fig. No.	Re_w $\times10^{-2}$	We_w $\times10^{-7}$	Ca_w $\times10^{-5}$	Bo $\times10^{-3}$	Bo_e	Fig. No.	Re_c	We_c	Ca_c	Bo $\times10^{-3}$	Bo_e
1.	4.3b(v - viii)	1.8	2.28	1.22	4.7	0 - 0.29	4.3b(i – iv)	2.9	0.19	0.067	1.6	0 - 0.25
2.	4.4(a)	6.6	28.9	4.4	4.7	0.074	4.4(b)	2.9	0.19	0.066	1.6	0.294
3.	4.4(c)	1.8	2.25	1.22	4.7	0.57	–	–	–	–	–	–
4.	4.5	6.6	28.9	4.4	4.7	0.12	–	–	–	–	–	–
5.	4.6(a)	1.85	2.25	1.22	4.7	1.15	–	–	–	–	–	–
6.	4.6(b)	1.85	2.25	1.22	4.7	5.27	–	–	–	–	–	–

APPENDIX – B

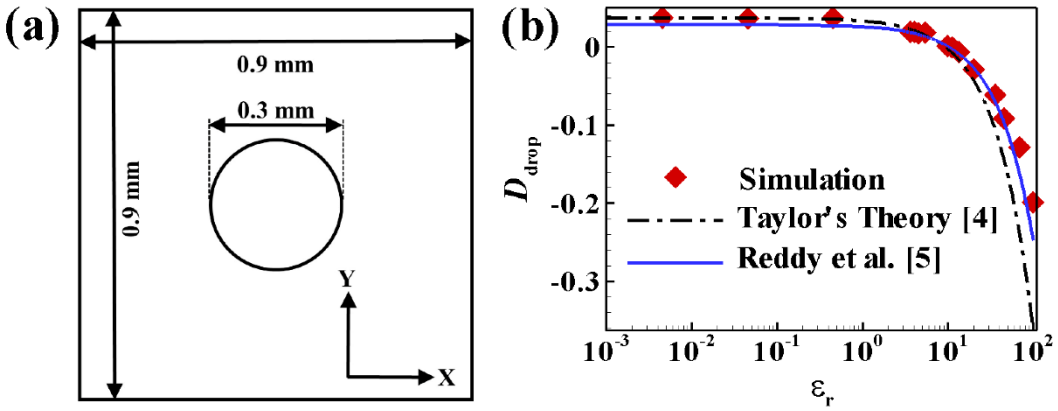

Figure B.1: (a) Schematic diagram of the computational domain taken for the validation. Plot (b) shows the quantitative comparison between theoretical and numerical droplet deformation.

Previous studies showed that electrohydrodynamic (EHD) stresses originating from the externally applied electric field can deform the interface of a circular droplet into prolate or oblate shapes depending upon the dielectric permittivity and electrical conductivity of the fluid mediums.[1-3] In order to validate the simulations performed here, we compare the numerical results obtained from the present study with a theoretical calculation on the deformation of a stationary droplet under an applied electric field.[4,5] The analytical expression for the droplet deformation (D) was previously predicted from the leaky dielectric model (LDM) theory[4] as,

$$D=(L-B)/(L+B)=0.56Bo_e\left(\sigma_r^2+1-2\varepsilon_r+0.6(\sigma_r-\varepsilon_r)(2+3\mu_r)/(1+\mu_r)\right)/(2+\sigma_r)^2$$

Here the notations L and B represent the length and breadth of the deformed droplet and $Bo_e=\left(\varepsilon_0\varepsilon_1 r\psi^2\right)/\gamma$ is the electric field Bond number in which r is the radius of the undeformed droplet, γ is the interfacial tension, ψ is the applied voltage, ε_0 is the permittivity of the free space, and ε_1 is the dielectric constant of the continuous oil phase. The

LDM theory suggests that a stationary droplet can easily deform into a prolate ($D > 0$) or oblate ($D < 0$) shape with the variations in ψ, γ, ε_r, and σ_r, under the influence of externally applied electric field.[4] Apart from the LDM theory the theoretical framework proposed by Reddy and Esmaeeli[5] has also been considered to validate the numerical results obtained in the present work, which proposed the droplet deformation (D) to be, $D = 0.33 Bo_e \left(\sigma_r^2 + \sigma_r + 1 - 3\varepsilon_r\right) / \left(1+\sigma_r\right)^2$.

APPENDIX – C

C.1 Microchannel fabrication and cleaning

Microwire molding technique was employed to fabricate the microchannels.[6,7] Polydimethylsiloxane (PDMS - Dow Corning, Sylgard 184 kit) along with copper wire was used in this fabrication procedure. Copper wire of diameter 300 μm were employed to construct the templates. The copper wires were joined by adhesives to get the required mold, which consisted of a main wire at the center and a series of tributary wires perpendicular to it. A trench of dimensions 50 mm × 30 mm × 5.5 mm (length × width × height) was prepared on a glass slide employing the double sided tapes. Thereafter, the prepared copper wire template was fit inside the trench. Then, a 1:10 (v/v) solution of cross-linker and pre-polymer of Sylgard 184 kit was prepared. The prepared solution was degasified by keeping the solution in vacuum for 30 min. The solution was then poured on the trench and template.

The trench made of double sided tapes filled with PDMS solution was then cured at 60^{o} C for 40 min in an air oven. After this, the PDMS was solidified and the cake was dipped in chloroform to inflate and then the copper wires were pulled out of the solidified PDMS cake. The resulting PDMS cake possessed one central microchannel connected to a series of tributary microchannels perpendicular to it, as shown in the Figure 6.8(b). The central microchannel was fabricated for the electrolyte to flow whereas the side microchanels were fabricated for electrode insertion. The side microchannels were then integrated with Cu-Cu_2O electrodes, as shown in the Figure 6.8(b), while one side of the main microchannel was used as the inlet for the salt-water flow and the other one as the outlet. The microchannels had inner diameter, d = 300 μm. Before the experiments initiated, the

microchannels were cleaned for 10 min with acetone and methanol simultaneously in the ultra-sonication bath before cleaning with 10% (v/v) dilute piranha solution (H_2SO_4:H_2O_2, 3:1) for 15 min. Further, repeated washing of the microchannel was performed with DI water for 5 min. The microchannel was then dried by blowing nitrogen gas followed by a heating of 20 min at 70 °C in air-oven before used for the experiments.

C.2 Measurement of generated photo-current and photo-voltage

In order to measure the photo-current and photo-voltage characteristics of the DEH and MEH, a variable resistance (R_L) of 1 kΩ was connected in series. A voltmeter (Mastech Digital Inc., M92AH) and an ammeter (Mastech Digital Inc., M92AH) were connected to the solar cell as described in Figure C.1. The variable resistance R_L was varied to measure the generated voltage and current. At highest value of R_L, the generated voltage was approximately equal to the open circuit voltage (V_{OC}).

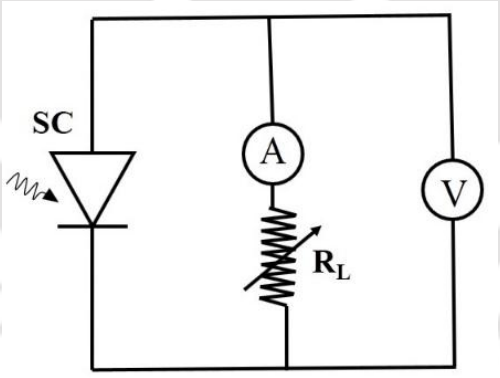

Figure C.1: Circuit diagram for measuring the photo-current and photo-voltage characteristics of the DEH and MEH where SC is the DEH or MEH, which was connected to a voltmeter and an ammeter as shown. The notation R_L is a variable load resistance, which was tuned in order to get different set of photo-current and photo-voltage.

The R_L can be disconnected while measuring the V_{OC} whereas at R_L = 0, the photo-generated current was assumed to be the short-circuit current density (J_{SC}). The point of

maximum power (V_m, J_m) was calculated from the points by changing the value of R_L. The fill factor (FF) of the cell was evaluated using the equation,

$$FF = \left(\frac{V_m \times J_m}{V_{OC} \times J_{SC}} \right) \times 100\% \quad \text{(C.2.1)}$$

Here, V_m and J_m are the voltage and current density for maximum power (P_{max}) and V_{OC} and I_{SC} are the open-circuit voltage and short-circuit current. The overall photo conversion efficiency was calculated by the equation,

$$\eta = \frac{V_{OC} \times J_{SC} \times FF}{P_{in}} \quad \text{(C.2.2)}$$

Here P_{in} is the incident radiant power density.

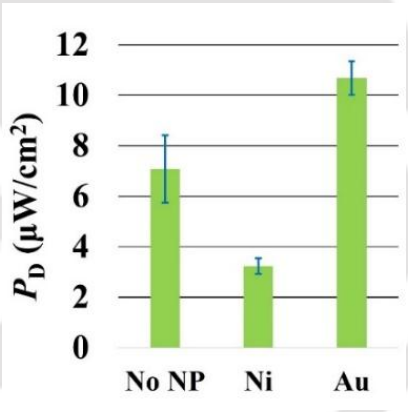

Figure C.2: The image shows the power density of a 4 M aqueous NaCl microdroplet with suspended gold nanoparticles (Au), nickel nanoparticles (Ni) nanoparticles, and without nanoparticles (NoNP) placed in between Cu and Cu_2O electrodes exposed to a 100 W incandescent bulb at a luminous flux per unit area of 1.1 kLux.

The power and current density in MEH was calculated considering the effective active area of the electrodes. The electrodes employed in this case were cylindrical. The diameter of each electrode was ~240 μm. The length of the electrodes inside the electrolyte solution was ~150 μm. As the light was incident from the top, so only top-half of the electrode surface area was effectively generating the voltage. So, for the current and power density

calculations in MEH, we considered the top half surface of each electrode, multiplied by effective number of electrodes.

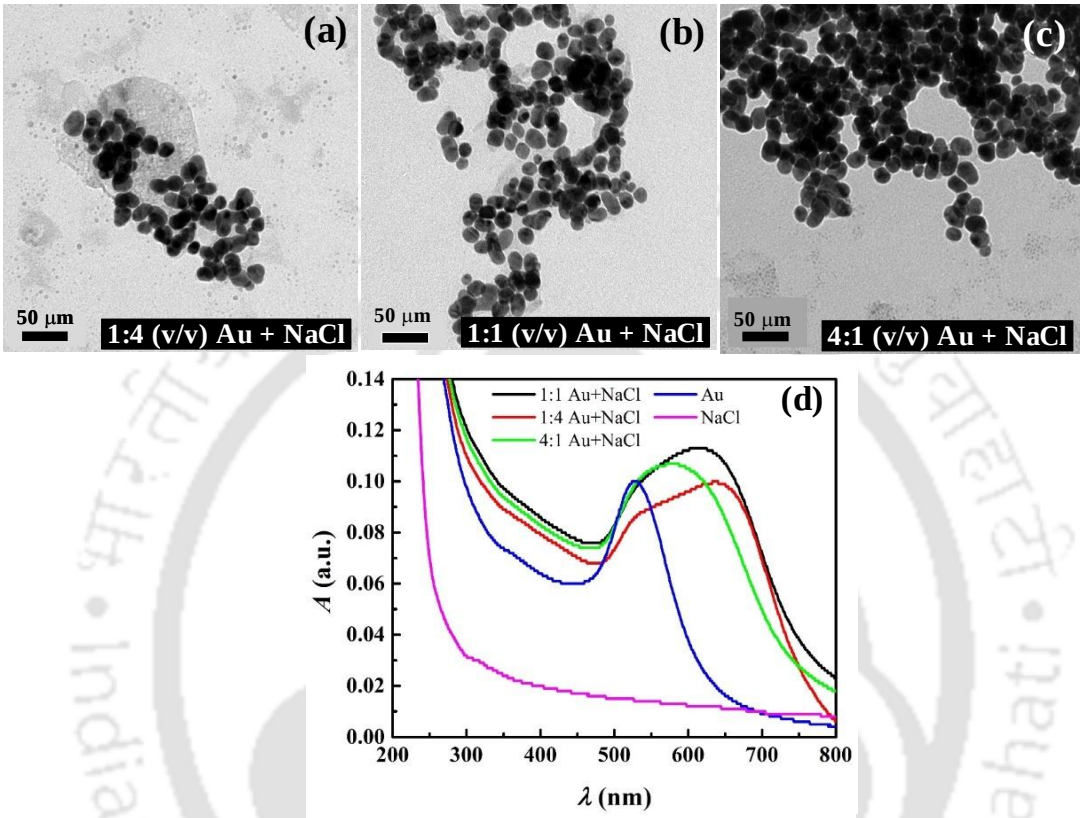

Figure C.3: The TEM images of (A) 1:4 (v/v) (B) 1:1 (v/v) (C) 4:1 (v/v) AuNPs in 4M aqueous NaCl solution. Image (D) shows the UV-vis spectra for AuNP-NaCl mixture of different proportion (v/v).

C.3 Effect of nanoparticles and optical characterization of AuNP

Figure C.2 shows the generation of power density in presence and absence of nanoparticles. A control experiment was performed where the Ni nanoparticles were suspended in a microdroplet and exposed to a light of intensity 1.1 kLux. The presence of Ni nanoparticels could not show any enhancement in the P_D whereas the AuNPs showed the enhancement due to the SPR effects.

C.4 Agglomeration of nanoparticles

The images in Figure C.3 illustrates the effect of electrolyte on the synthesized AuNPs. In this experiment, the synthesized AuNPs were mixed with 4 M aqueous NaCl solution at different proportions (1:4, 1:1 and 4:1 v/v) and then a TEM analysis was performed. It was found that the increase in the NaCl proportion led to higher agglomeration of AuNPs as shown in the images (a) – (c) of Figure C.3. Moreover, the agglomeration of the AuNPs with increased proportion in the salt solution had also been reflected absorption spectra from the UV-Vis spectroscopy, as illustrated in image (d).

REFERENCES

1. Y. Lin, P. Skjetne, and A. Carlson, International Journal of Multiphase Flow **45**, 1 (2012).
2. Y. Lin, Electrophoresis **34**, 736 (2013).
3. O. Vizika and D. A. Saville, Journal of Fluid Mechanics **239**, 1 (1992).
4. G. Taylor, Proceedings of the Royal Society of London. Series A. Mathematical and Physical Sciences **291**, 159 (1966).
5. M. N. Reddy and A. Esmaeeli, International Journal of Multiphase Flow **35**, 1051 (2009).
6. M. K. Verma, A. Majumder, and A. Ghatak, Langmuir **22**, 10291 (2006).
7. Y. Jia, J. Jiang, X. Ma, Y. Li, H. Huang, K. Cai, S. Cai, and Y. Wu, Chinese Science Bulletin **53**, 3928 (2008).